Science Advances
AAAS

Supplementary Materials for

Ozone chemistry in western U.S. wildfire plumes

Lu Xu*, John D. Crounse, Krystal T. Vasquez, Hannah Allen, Paul O. Wennberg*, Ilann Bourgeois, Steven S. Brown, Pedro Campuzano-Jost, Matthew M. Coggon, James H. Crawford, Joshua P. DiGangi, Glenn S. Diskin, Alan Fried, Emily M. Gargulinski, Jessica B. Gilman, Georgios I. Gkatzelis, Hongyu Guo, Johnathan W. Hair, Samuel R. Hall, Hannah A. Halliday, Thomas F. Hanisco, Reem A. Hannun, Christopher D. Holmes, L. Gregory Huey, Jose L. Jimenez, Aaron Lamplugh, Young Ro Lee, Jin Liao, Jakob Lindaas, J. Andrew Neuman, John B. Nowak, Jeff Peischl, David A. Peterson, Felix Piel, Dirk Richter, Pamela S. Rickly, Michael A. Robinson, Andrew W. Rollins, Thomas B. Ryerson, Kanako Sekimoto, Vanessa Selimovic, Taylor Shingler, Amber J. Soja, Jason M. St. Clair, David J. Tanner, Kirk Ullmann, Patrick R. Veres, James Walega, Carsten Warneke, Rebecca A. Washenfelder, Petter Weibring, Armin Wisthaler, Glenn M. Wolfe, Caroline C. Womack, Robert J. Yokelson

*Corresponding author. Email: lu.xu@noaa.gov (L.X.); wennberg@caltech.edu (P.O.W.)

Published 8 December 2021, *Sci. Adv.* **7**, eabl3648 (2021)
DOI: 10.1126/sciadv.abl3648

This PDF file includes:

1 FIREX-AQ

The Fire Influence on Regional to Global Environments and Air Quality (FIREX-AQ) campaign focused on characterizing fire emissions and investigating their environment impacts. During FIREX-AQ, the NASA DC-8 aircraft conducted 22 research flights between July 24 and September 5, 2019. From July 24 to August 16, the aircraft was based in Boise, Idaho to study the wildfires in the western U.S. From August 21 to September 5, the aircraft was based in Salina, Kansas to characterize prescribed fires, including agricultural burning, forest understory burning, etc. This study focuses on the O_X formation in western wildfire plumes and utilizes measurements from 13 research flights that sampled 10 distinct fires, including repeated visits to the same fire (i.e., Williams Flats fire in Washington state) on different days. The related flight tracks are shown in Figure S1. The aircraft typically took off between 15:00 and 17:00 (Mountain Daylight Time, GMT - 6) and flight duration was around 7 h. The majority of the wildfire plumes sampled in FIREX-AQ were not mixed with smoke from other fires. Thus, the smoke sampled could be traced back to a definitive source.

The sampling strategy typically measured the smoke plume close to the wildfire to characterize the primary emissions followed by multiple crosswind plume transects downwind of the fire. We define the set of such crosswind transects through the smoke plume as a "fire ladder". In some flights, the same wildfire was sampled with more than one fire ladder at a different time of day. The aircraft true air speed was about 150 m s^{-1}, which yields a horizontal resolution of 150 m for the in situ 1Hz measurements. The crosswind plume width varies significantly with fires and downwind distance. Because of air traffic control, the minimal distance to fire is restricted and ranges from 2 to 20 km. The furthest sampling distance varies with fires and it typically ranges from 60 to 200 km.

Previous analyses on similar fire ladders typically analyzed the plume evolution as a function

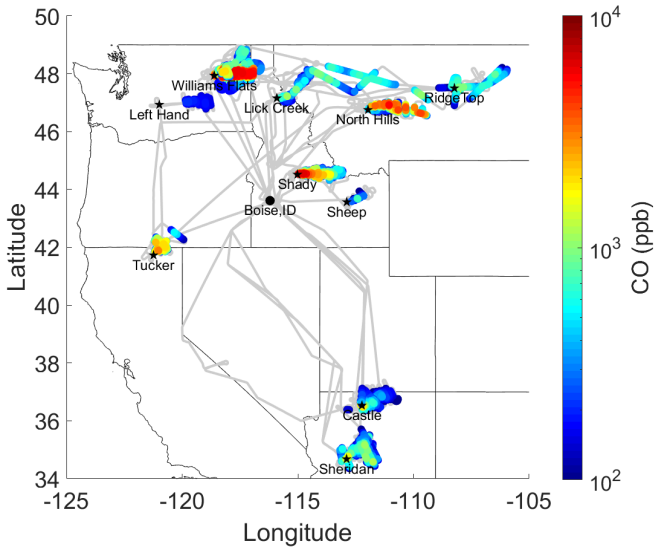

Figure S1: The flight tracks of the NASA DC-8 for sampling wildfires in the western U.S. during FIREX-AQ.

of smoke physical age, which is computed from downwind distance and wind speed, in a pseudo-Lagrangian framework (*6, 7, 9*). The potentially changing fire conditions over time requires that the aircraft follows the same airmass when transecting the plume at different downwind distances in order to validate this analysis approach. However, this requirement is often challenged by the aircraft navigation artifacts and complex plume dispersion. For example, Figure S3 in Wiggins et al. (*31*) illustrates that the equivalent aircraft speed along the plume length (i.e., downwind distance between successive transects/sampling time interval) is considerably faster than the wind speed in FIREX-AQ. In other words, the smoke sampled in different transects was emitted at different times, with samples further downwind being emitted earlier in the day. Even if the plumes were sampled in a pseudo-Lagrangian fashion, the complex plume dispersion could still cause artifacts, as a crosswind transect only takes a snapshot of plume composition at a given altitude but not the plume 3D structure. For example, while one transect crosses the dense portion of the plume, another transect may only skim

the top edge of the plume. Contrasting these two transects inevitably introduces uncertainty in examining plume evolution. Analysis based on a single transect, which samples smoke emitted under similar conditions, is less impacted by fluctuations in fire emissions over time. The different extent of photochemical processing between the plume center and edges results in different plume compositions across each crosswind transect. This phenomenon has been observed in previous studies on both power plant and wildfire plumes (*14, 17, 32–35*). Here, we apply single transect analysis to quantitatively investigate the O_x chemistry in wildfire plumes.

The sampled fires were representative of those occurring in coniferous- and chaparral-dominated ecosystems of the western U.S. More details about the sampled fuel types are documented in FIREX-AQ data archive. According to previous elemental analysis of fuels characteristic of the western US, the nitrogen content is in the range 0.23-1.28% (*36*).

The modified combustion efficiency (MCE) indicates the relative abundance of flaming and smoldering combustion. MCE is calculated for each transect using Eqn.S1:

$$\mathrm{MCE} = \frac{1}{m_{CO/CO_2} + 1} \tag{S1}$$

where m_{CO/CO_2} represents the slope of the York regression between the mixing ratio of CO and CO_2 for each transect. The MCE in this study ranges from 0.85 to 0.95, with a median value of 0.91 (Figure S2). More than 90% of transects have MCE smaller than 0.92. It is noteworthy that the temperate wildfires generally burn at lower efficiencies than the laboratory simulations (*36*).

Smoke age is estimated from airmass trajectory analysis. Upwind trajectories are initialized at the aircraft location every 5 s and computed in HYSPLIT (*37*) with three sets of meteorological data: HRRR, NAM CONUS nest, and GFS. Trajectories that are grossly inconsistent with smoke transport direction observed by geostationary satellite imagers (GOES-16 and GOES-17; GOES-R Algorithm Working Group, 2017) are excluded from further analysis. The smoke age is determined from the point where the upwind trajectory makes its closest approach to the

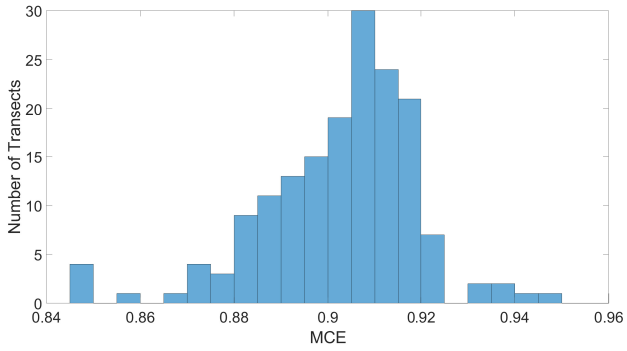

Figure S2: The histogram of MCE for wildfire plume transects in this study.

fire source, plus time for the buoyant plume rise from the surface to the trajectory altitude at 7 m s^{-1}. We average the age estimates from the three meteorological datasets (excluding any that are inconsistent with observed transport) to form a single best estimate of the smoke age. Uncertainty in each age estimate is computed from the spread between meteorological datasets, errors in model wind speed, and additional uncertainties in the emission location within large-area fires and plume rise speed. Median age uncertainties are 27%.

The fire radiative power (FRP) is an important indicator of fire strength. The detailed procedure to obtain the diurnal cycle of FRP for the wildfires specific to the FIREX-AQ campaign is discussed in Wiggins et al. (*31*) and briefly described below. FRP is obtained from both GOES-16 and -17 Advanced Baseline Instruments (ABI). GOES data included are within 2 pixels (4km) of the final GeoMAC final fire perimeter. We chose a two-pixel distance to optimize for 90% of the energy sensed by the ABI instrument, based on the Point Response Function. We calculate the raw FRP by summing up FRP for each 5-min period. Then, we modify the raw FRP to represent a more realistic diurnal fire cycle (denoted as pseudo-raw FRP) in the following procedure. First, an adjusted FRP is generated by subtracting 5% from each 5-minute total FRP period throughout the day. Second, the subtracted 5% is redistributed equally across quiescent FRP times, which are defined as periods with no FRP observations for

a given 5-minute period. Third, the "quiescent mean" value, defined as 5% total daily FRP / number of quiescent 5-minute periods, is added to any remaining 5-minute interval where the adjusted FRP is less than the "quiescent mean". Fourth, the transition between quiescent and active FRP is smoothed. Finally, the resultant product provides a continuous function for the allocation of emissions across the diurnal cycle, based on FRP variability.

2 Instrumentation

The NASA DC-8 aircraft hosted an unprecedented atmospheric chemistry payload and provided comprehensive in situ characterization of fire emissions and their atmospheric evolution. The instruments of interest to this study are summarized in Table S1. Species included in this analysis are ~80 VOCs, CH_4, C_2H_6, HCHO, CHOCHO, O_3, NO, NO_2, HNO_3, peroxyacylnitrates (PANs), particulate nitrate (pNO_3), oxygenated aromatics, and hydroxyperoxides and hydroxynitrates produced from the oxidation of ethene and propene. All the measurements are 1Hz, except the discrete whole air samples (iWAS). As discussed in Section S7, we generate pseudo 1Hz estimates of all VOCs measured by iWAS as a group by interpolating between the discrete observations using the 1Hz C8-aromatics measurement of PTR-ToF-MS.

The extensive instrument payload on the NASA DC8 allows the characterization of several critical species with different techniques. When duplicate measurements are available, the measurement is selected based on an integrated consideration of measurement precision and accuracy, data coverage, and instrument response time. The NO concentration is measured by both laser-induced fluorescence (LIF) (*38*) and chemiluminescence (CL) (*33*) methods. Two measurements agree within a 20% calibration uncertainty. The LIF NO is selected because it has better precision (i.e., 1 ppt for LIF-NO vs. 6 ppt for CL-NO) and data coverage (nearly 100% for LIF-NO vs. ~40% for CL-NO). NO_2 concentration is measured by three instruments: nonresonant laser-induced fluorescence (CANOE) (*39*), chemiluminescence (CL) (*33*), and

airborne cavity enhanced spectrometer (ACES) (*40*). Given that the three measurements agree well (∼10%), for each flight, we select the measurement with the largest coverage of plume data. HONO is measured by two instruments: I^- CIMS (*41*) and (ACES) (*40*). In general, two measurements show high correlation on flights when the HONO concentration is much larger than the ACES measurement precision (600 ppt), but the correlation slope ranges from 0.9 to 1.8, depending on flight. The reason for the lack of agreement between two techniques is under investigation. HONO measured by I^- CIMS is selected because of its better precision (3 ppt for I^- CIMS vs. 600 ppt for ACES). Using ACES HONO does not alter any conclusions in this study. Phenol is measured by two instruments: CF_3O^- CIMS and PTR. The inter-comparison shows a good correlation, but a poor quantitative agreement. CF_3O^- CIMS measurement is lower than PTR measurement by a factor of 3-4. This difference is also under investigation and likely caused by absolute calibration of phenol standards. The main usage of phenol is to calculate OH exposure and the systematic bias between the CF_3O^- CIMS and PTR measurements does not affect the calculation, because the calculation relies on the loss fraction of phenol, instead of its absolute concentration. The HCHO is measured by two instruments: the laser-induced fluorescence instrument (ISAF) (*42*) and the compact atmospheric multi-species spectrometer (CAMS) (*43*). ISAF HCHO, which is used in this analysis, is 27% lower than CAMS HCHO. The source of the systematic bias has not been resolved at this time, but likely caused by the absolute calibration of HCHO standards (*44*). Using CAMS HCHO increases the slope of York fit in Figure 7 from 1.12 to 1.15. HCN is measured by several instruments, including PTR, CF_3O^- CIMS, I^- CIMS, and NCAR trace organic gas analyzer (TOGA) (*29*). The instrument comparison shows complex results. In this study, we use HCN measured by CF_3O^- CIMS and the HCN mixing ratios are determined from the relative signals arising from ambient HCN ($H^{12}C^{14}N$) and continuously added standard addition of isotopically labeled $H^{13}C^{15}N$. In this study, HCN is mainly used together with CO (i.e., ΔHCN/ΔCO) to diagnose the variation of

fire emissions across individual transects, so that the uncertainty in the absolute concentration of HCN does not affect this analysis.

Measurement	Technique	Accuracy	Reference	Note
O_3	gas phase chemiluminescence	2%	(*33*)	
NO_y	gas phase chemiluminescence	10-15%	(*33*)	
NO_2	nonresonant laser-induced fluorescence	10%	(*39*)	a
	gas phase chemiluminescence	7%	(*33*)	
	airborne cavity enhanced spectrometer	4%	(*40*)	
NO	laser-induced fluorescence	9%	(*38*)	
phenol & HNO_3 & HCN	CIMS (CF_3O^-)	25%	(*45*)	
OVOCs	CIMS (CF_3O^-)	25%	(*45*)	b
PANs	CIMS (I^-)	20-30%	(*46*)	c
pNO_3	HR-ToF-AMS	34%	(*47–49*)	
VOCs	whole air sampler with offline GC-MS	6-17%	(*50*)	d
VOCs	PTR-ToF-MS	25%	(*51, 52*)	e
HCHO	laser-induced fluorescence	10%	(*42*)	
CO	diode laser spectrometer	2-7%	(*53*)	
CH_4	diode laser spectrometer	1%	(*53*)	
C_2H_6	absorption spectrometer	2%	(*43*)	
CHOCHO	airborne cavity enhanced spectrometer	4%	(*40*)	
HONO	CIMS (I^-)	15%	(*41*)	
Photolysis frequencies	actinic flux spectroradiometry	12-20%	(*54*)	
H_2O	diode laser hygrometer	5%	(*55*)	

[a] The instrument in this study was operated at wavelength 532 nm, which is different from that in the reference.
[b] OVOCs measured by CF_3O^- CIMS include phenol, hydroxynitrates and hydroperoxide produced from the OH-initiated oxidation of ethene and propene.
[c] Four peroxy acyl nitrates (PANs) are measured by I– CIMS, which are peroxyacetyl nitrate (PAN), peroxylpropionyl nitrate (PPN), peroxylbutyryl nitrate (PBN), and peroxyacryloyl nitrate (APAN).
[d] The full list of VOCs measured by the NOAA integrated whole air sampler is shown in Table S3.
[e] The full list of VOCs measured by PTR-ToF-MS is shown in Table S4.

Table S1: Instrumentation List

3 OH exposure

3.1 Calculation of OH exposure

The time-integrated exposure of the fire emissions to OH (i.e., OH exposure) is estimated using the observed ratio between two VOCs (*56–58*). For a pair of VOC species to be selected in the OH exposure calculation, they should satisfy the following criteria: (1) they arise from the same source; (2) their dominant atmospheric fate is reaction with OH; and (3) the lifetime of at least one VOC should be comparable to the time scale of interest. In addition, the single transect analysis requires that the VOCs are measured at high temporal resolution (at least 1Hz). Among $\sim$80 VOCs quantified in this study, few satisfy the above criteria. For example, the most widely used toluene/benzene ratio in the literature is not applicable here, because their lifetimes (i.e., $\sim$10 days and $\sim$1.8 days and for benzene and toluene, respectively) are much longer than the smoke evolution time (<12 h) in this study. Furans have lifetimes on a similar scale as smoke age, but they are sticky and subject to partitioning delay in sampling lines. After a comprehensive search and evaluation, we utilize the phenol/benzene ratio to estimate OH exposure, because both species are directly emitted from fire, dominantly react with OH, and are reliably measured by CF_3O^- CIMS and PTR-ToF-MS, respectively, with 1Hz frequency. Phenol has a lifetime of $\sim$8 h under typical atmospheric OH concentration, well matched to the maximum smoke transport time in this study. A minor fraction of phenol is consumed by nitrate radical for these daylight conditions. It is estimated that even in the plume center of the densest plume where the phenol+nitrate radical reaction is the most important, more than 90% of phenol is consumed by OH (*59*).

The equation to calculate OH exposure is similar to previous studies, with slight modifications to account for the secondary production of phenol from benzene oxidation. In the derivation below, we start from simplified conditions and then generalize the expression to ambient conditions.

The major reactions of benzene and phenol in the fire plume are represented as follows:

$$B + OH \xrightarrow{k_{B+OH}} Y_P \times P$$

$$P + OH \xrightarrow{k_{P+OH}} \text{products}$$

, where B and P represent benzene and phenol, respectively, Y_P represents the phenol yield from OH-initiated oxidation of benzene. Assuming no dilution, the change rates of benzene and phenol concentrations are governed by

$$\frac{d[B]}{dt} = -k_{B+OH}[B][OH]$$

$$\frac{d[P]}{dt} = Y_P k_{B+OH}[B][OH] - k_{P+OH}[P][OH]$$

Further, the above equations are integrated to obtain

$$[B]_{t_M} = [B]_{t_E} e^{-k_{B+OH}\int_{t_E}^{t_M}[OH]\cdot dt} \tag{S2}$$

$$[P]_{t_M} = Y_P[B]_{t_E}\frac{k_{B+OH}}{k_{P+OH}-k_{B+OH}}(e^{-k_{B+OH}\int_{t_E}^{t_M}[OH]\cdot dt} - e^{-k_{P+OH}\int_{t_E}^{t_M}[OH]\cdot dt}) + [P]_{t_E}e^{-k_{P+OH}\int_{t_E}^{t_M}[OH]\cdot dt} \tag{S3}$$

where t_E and t_M represent the time of emission and of measurement, respectively. Equations S2 and S3 are combined and rearranged to obtain

$$\frac{[P]_{t_M}}{[B]_{t_M}} - Y_P\frac{k_{B+OH}}{k_{P+OH}-k_{B+OH}} = (\frac{[P]_{t_E}}{[B]_{t_E}} - Y_P\frac{k_{B+OH}}{k_{P+OH}-k_{B+OH}})e^{(k_{B+OH}-k_{P+OH})\int_{t_E}^{t_M}[OH]\cdot dt} \tag{S4}$$

Rearrange Eqn.S4 to obtain an expression for OH exposure

$$\int_{t_E}^{t_M}[OH]\cdot dt = \frac{\ln(\frac{[P]_{t_E}}{[B]_{t_E}} - Y_P\frac{k_{B+OH}}{k_{P+OH}-k_{B+OH}}) - \ln(\frac{[P]_{t_M}}{[B]_{t_M}} - Y_P\frac{k_{B+OH}}{k_{P+OH}-k_{B+OH}})}{k_{P+OH}-k_{B+OH}} \tag{S5}$$

We then substitute $\frac{[P]_{t_E}}{[B]_{t_E}}$ with the excess ratio $\frac{\Delta[P]_{t_E}}{\Delta[B]_{t_E}}$ to account for dilution and finally arrive at Eqn.S6.

$$\int_{t_E}^{t_M}[OH]\cdot dt = \frac{\ln\left(\frac{\Delta[P]_{t_E}}{\Delta[B]_{t_E}} - Y_P\frac{k_{B+OH}}{k_{P+OH}-k_{B+OH}}\right) - \ln\left(\frac{\Delta[P]_{t_M}}{\Delta[B]_{t_M}} - Y_P\frac{k_{B+OH}}{k_{P+OH}-k_{B+OH}}\right)}{k_{P+OH}-k_{B+OH}} \quad \text{(S6)}$$

In Eqn.S6, k_{B+OH} and k_{P+OH} are calculated at sampling temperature. Y_P is 0.53, which is obtained at room temperature (*60*), as the temperature-dependent value is unknown. The impact of secondary production of phenol on estimated OH exposure is minor, because of the slow consumption of benzene and the secondary production being much smaller than the large amount of primary phenol emission. Nonetheless, we do account for the small amount of phenol production in the OH exposure calculation. The initial [P]/[B] excess ratio (i.e., $\frac{\Delta[P]_{t_E}}{\Delta[B]_{t_E}}$) is represented by the 95th percentile of $\frac{\Delta[P]}{\Delta[B]}$ from the transects close to fire. The $\frac{\Delta[P]_{t_E}}{\Delta[B]_{t_E}}$ value does not affect the O_x chemical closure analysis (i.e., Eqn.3) because that analysis utilizes the difference in OH exposure across each transect (denoted as ΔOH exposure) and any error cancels in the calculation. For the 25 transects involved in the analysis, the ΔOH exposure ranges from 0.73 to 2.51×10^{10} molecule cm^{-3} s. The ΔOH exposure is equivalent to 2 to 7 h transport time, assuming a constant OH concentration of 1×10^{6} molecule cm^{-3}.

Besides chemical loss, another factor influencing ratio between two VOCs is atmospheric mixing (*56, 57*). When the influence of mixing on the ratio of two VOCs is taken into account, the expression for OH exposure is shown in Eqn.S7, following the derivation in McKeen et al. (*57*).

$$\int_{t_1}^{t_2}[OH]\cdot dt = \frac{1}{k_Y-k_X}\left(\ln\frac{[Y]_{t_1}-\frac{D[Y]_{bkg}}{D+k_{Y+OH}[OH]}}{[X]_{t_1}-\frac{D[X]_{bkg}}{D+k_{X+OH}[OH]}} - \ln\frac{[Y]_{t_2}-\frac{D[Y]_{bkg}}{D+k_{Y+OH}[OH]}}{[X]_{t_2}-\frac{D[X]_{bkg}}{D+k_{X+OH}[OH]}}\right) \quad \text{(S7)}$$

In Eqn.S7, D is a coefficient to describe the atmospheric mixing. Eqn.S7 is difficult to solve analytically. To reduce the interference of atmospheric mixing on estimated OH exposure, we estimate the OH exposure only for the measurements when the phenol and benzene concentrations are at least 10 times higher than ambient background levels. Another approximation worth noting is that the $\frac{D[X]_{bkg}}{D+k_{X+OH}[OH]}$ term is replaced with $[X]_{bkg}$.

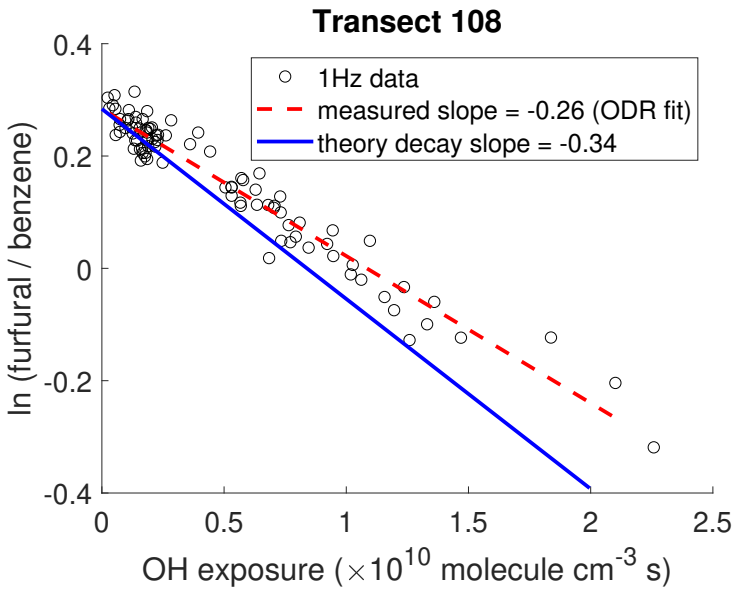

Figure S3: Example plot to illustrate the evaluation of OH exposure estimated from the phenol/benzene ratio against the observed furfural/benzene ratio.

The uncertainty of OH exposure derived from the phenol/benzene ratio is evaluated based on the measured decay of other pairs of VOCs. One example of such evaluation is shown in Figure S3. This figure displays the measured furfural/benzene ratio as a function of OH exposure (inferred from phenol/benzene ratio) for one plume transect. The measured furfural is assumed to be the 2-furfural isomer, because it is 21 times more abundant than 3-furfural based on GC measurements in the 2016 FIREX FireLab study (*15*). On the one hand, the theoretical decay rate of furfural/benzene ratio is calculated based on their reaction rate coefficients with OH (i.e., $(k_{benzene+OH} - k_{furfural+OH}) \times 10^{10}$), which is denoted as "theoretical decay rate" and is -0.34 for this transect. On the other hand, the decay rate can also be calculated by fitting the observed furfural/benzene ratio vs. OH exposure, which is denoted as "measured decay rate" and is -0.26 for this transect. By comparing the decay rates from two methods, the measured decay rate is slower than the theoretical one, suggesting the OH exposure is overestimated. We apply this analysis to all transects for three pairs of VOCs: phenol/HCN, furfural/benzene, and

styrene/benzene. Figure S4 shows the histogram of the ratio of measured/theoretical decay rate for each pair and a Gaussian distribution is fitted to the histogram. Regarding phenol/HCN, the mode of the histogram (based on Gaussian fit) is 0.97, suggesting that the phenol/benzene-derived OH exposure can reasonably reproduce the phenol/HCN decay. This agreement also suggests the the secondary production of phenol is small, because replacing the slow VOC benzene with HCN has small impacts on the estimated OH exposure. Regarding the furfural/benzene ratio, the mode of the histogram is 0.79, suggesting the phenol/benzene-derived OH exposure is overestimated by $\sim$30%. Regarding styrene/benzene ratio, the mode of the histogram is 1.34, suggesting measured decay rate is faster than theoretical decay rate by $\sim$25%. This is expected because styrene has significant additional loss via reaction with O_3. Overall, we estimate that the uncertainty in the calculated OH exposure based on the phenol/benzene ratio is $\sim$30%.

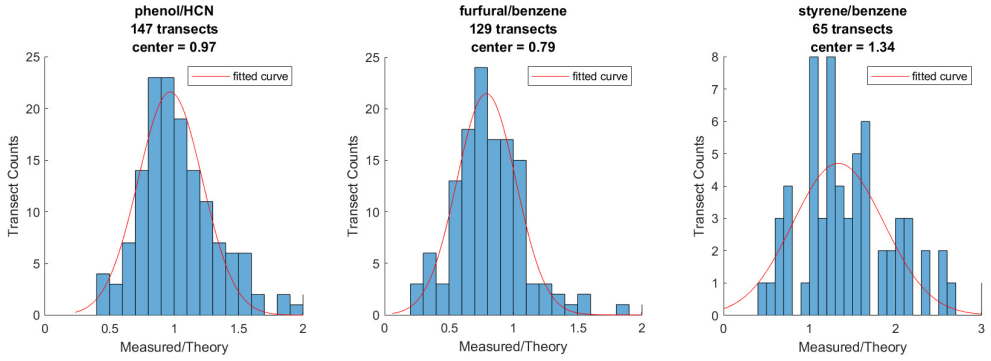

Figure S4: The histogram of the ratio of measured to theoretical decay rate. The analysis illustrated in Figure S3 is applied to all plume transects, but only transects with r^2 of the linear fit greater than 0.2 are included in the histogram. The histogram is fitted with Gaussian curve.

3.2 HO_x sources

Dividing the OH exposure by the smoke age provides an estimate of the average OH concentration that the smoke experiences from emission to measurement. The OH concentration derived using this method for the flight on 8/3/2019 is shown in Figure S5. At 1 h after smoke emission, the average OH concentration on the plume edge is $\sim 4 \times 10^6$ molecules cm^{-3}, 40 times higher than that in the plume center where attenuated actinic flux hinders the photolysis of HONO. The difference between plume center and edges gradually diminishes as smoke ages. We caution that the estimated OH concentration depends on the emission ratio of phenol to benzene, but this uncertainty is unlikely to substantially alter the observed evolution of OH concentration.

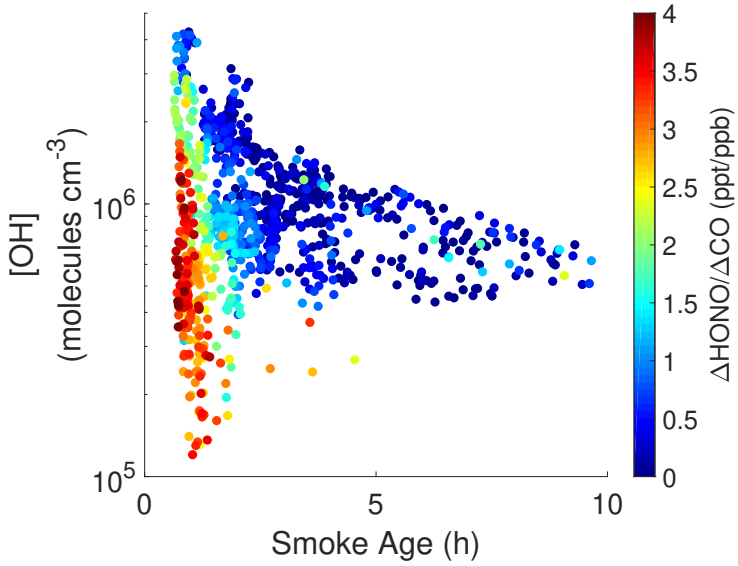

Figure S5: The evolution of OH concentration as a function of smoke age for the second fire ladder on 8/3/2019 flight. The smoke age is estimated based on backtrajectory analysis.

The instantaneous production rate of HO_x (P_{HOx}) is calculated using Eqn.S8, by following Peng et al. (*14*). The photolysis rates and concentrations are obtained from in situ measurements, and φ_{OH} represents the OH yield from $O(^1D)+H_2O$ (Eqn.S9). The relative contribution of HONO photolysis to total HO_x production is calculated using Eqn.S10.

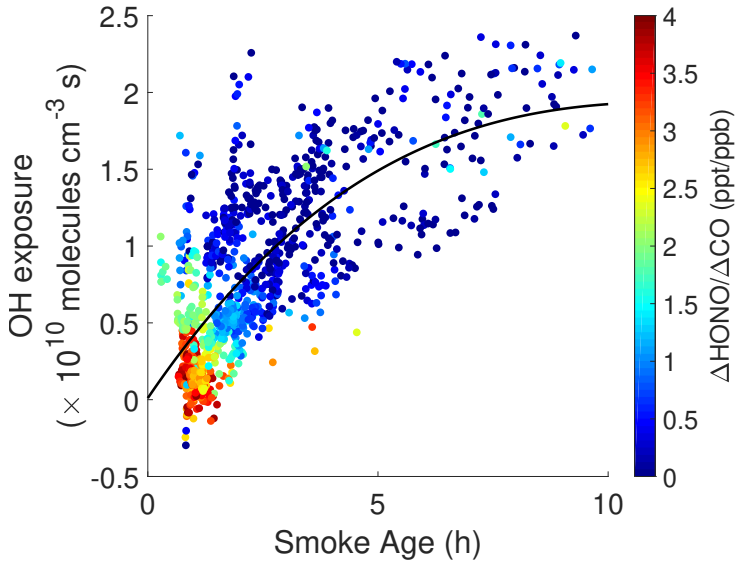

Figure S6: The OH exposure quickly increases to $\sim 1 \times 10^{10}$ molecule cm^{-3} s in 2 h. Beyond 2 h, coinciding with a depletion of HONO, it takes nearly 8 h to gain another $\sim 1 \times 10^{10}$ molecule cm^{-3} s increment in OH exposure. The black line is provided as a visual aid.

The relative contributions of HONO photolysis and HCHO photolysis to P_{HO_x} change over time. Figure S7 displays the P_{HO_x} enhancement in the plume relative to the clear sky as a function of HO_x production rate from HONO photolysis (i.e., $P_{HO_x,HONO}$) for the flight on 8/3/2019. When $P_{HO_x,HONO}$ is near its maximum value of 4 ppt s^{-1}, the P_{HO_x} in the plume is 300 times faster than that outside the plume and the HO_x production rate from HCHO photolysis (i.e., $P_{HO_x,HCHO}$) makes a minor contribution to P_{HO_x}. As $P_{HO_x,HONO}$ decreases, the P_{HO_x} enhancement decreases and $P_{HO_x,HCHO}$ becomes more important. For example, when $P_{HO_x,HONO}$ is about 0.01 ppt s^{-1}, higher $P_{HO_x,HCHO}$ leads to a factor of 10 enhancement in P_{HO_x}.

$$P_{HO_x} = j_{HONO}[HONO] + 2 \times j_{HCHO}[HCHO] + j_{CH_3CHO}[CH_3CHO] + \varphi_{OH} j_{O^1D}[O_3] \quad \text{(S8)}$$

$$\varphi_{OH} = \frac{2k_{O^1D+H_2O}[H_2O]}{k_{O^1D+H_2O}[H_2O] + k_{O^1D+O_2}[O_2] + k_{O^1D+N_2}[N_2]} \quad \text{(S9)}$$

$$f_{jHONO} = \frac{j_{HONO}[HONO]}{P_{HO_x}} \quad \text{(S10)}$$

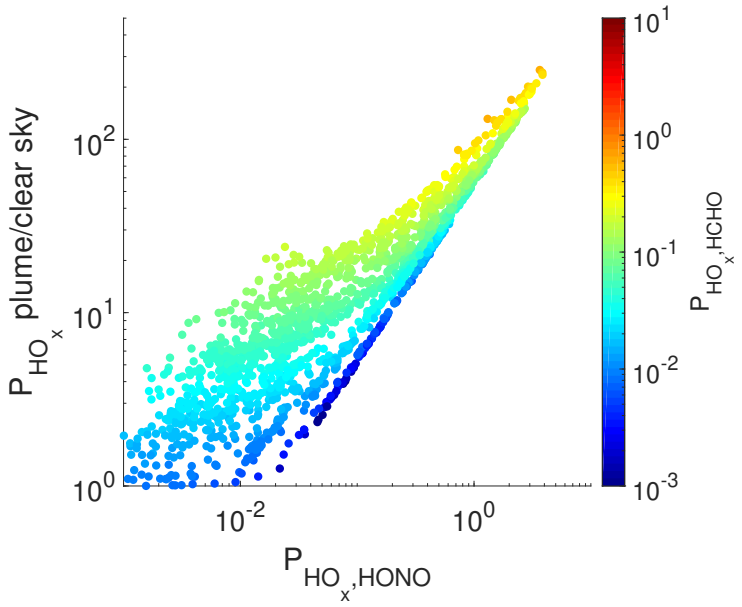

Figure S7: The enhancement of production rate of HO_x (P_{HO_x}) as a function of HO_x production rate from HONO photolysis (i.e., $P_{HO_x,HONO}$). The color represents the HO_x production rate from HCHO photolysis (i.e., $P_{HO_x,HCHO}$). The measurements are from the second fire ladder on 8/3/2019 flight. The P_{HO_x} in clear sky is on the order of 10^{-2} ppt s^{-1}.

3.3 HONO evolution

The observed contribution of HONO photolysis to the total HO_x production rate (denoted f_{jHONO}) varies greatly between fires. Figure S8 compares the maximum f_{jHONO} (denoted as $f_{jHONO,max}$) from the transect that encountered the highest [CO] between different fires. The highest [CO] was typically sampled in the transect closest to fire, which is typically 20 km to fire source. The minimal distance to fire is restricted by air traffic control to maintain an adequate distance between the DC8 and other aircraft supporting fire monitoring and fighting. Despite similar downwind distance, the $f_{jHONO,max}$ varies from 0.2 to 1 between different fires as shown in Figure S8, indicating that the relative contribution of HONO photolysis to

HO_x production is reduced to a larger extent in some fires. Such fire-to-fire variability is not driven by MCE as there is no correlation between $f_{jHONO,max}$ and MCE. Instead, the plume optical properties likely play a more important role. As a proxy for plume optical extinction, we use the reduction of HONO photolysis in the densest part of the plume (i.e., top 1% CO concentration) relative to the background photolysis rate determined outside the plume, which is calculated as 1 - $\frac{jHONO_{plume}}{jHONO_{background}}$. The $f_{jHONO,max}$ shows a positive dependence on jHONO reduction (Figure S8), implying that the contribution of HONO photolysis to the total HO_x production rate is larger in optically thicker plumes. This trend is likely caused by that in optically thin plumes (i.e., small jHONO reduction), rapid HONO photolysis occurs in the immediate vicinity of fires (i.e., lifetime $\sim$15 minute in daytime background air), resulting in large HONO depletion when such plumes are intercepted by aircraft at the minimal distance. As a result, the observed $f_{jHONO,max}$ is small for optically thin plumes. This observation suggests that the most active photochemistry in optically thin plumes may not have been captured by the aircraft sampling. The implication is that the emission ratios of reactive trace species measured in the field can be lower than that from laboratory studies which characterized the fire emissions with minimal photochemical processing. This finding may also cause, to some extent, the variability in OA evolution observed in the literature (*61*). For example, in optically thin plumes, the active photochemistry producing SOA near the fire may not be captured by some airborne measurements. Using the Δ[OA]/Δ[CO] measured in transects closest to fire as the baseline could lead to observed net decreases in OA as smoke ages, because the photochemistry is already weakened at this point and dilution-induced evaporation drives the OA concentration.

4 Transect selection

A plume transect is defined as a period between the aircraft entering and exiting the smoke plume. As this study focuses on near-field concentrated plumes, the start and stop times for

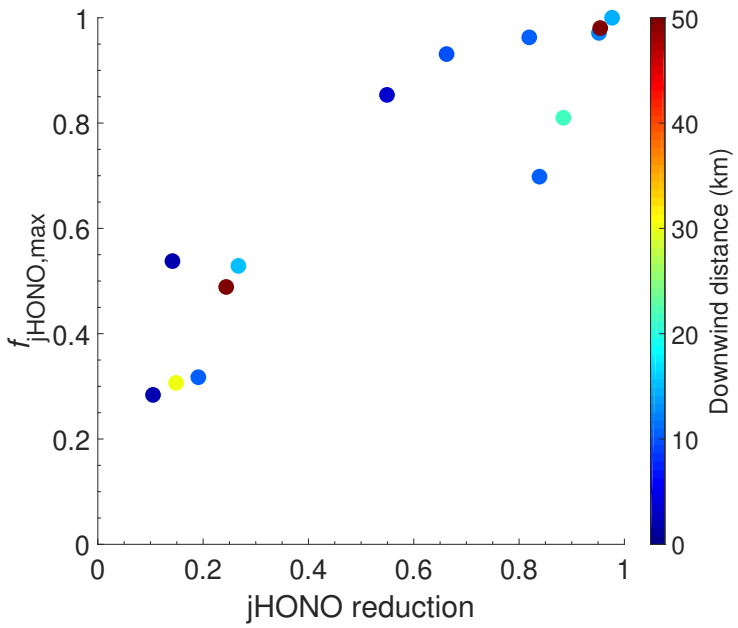

Figure S8: The relationship between $f_{jHONO,max}$ and jHONO reduction in plume. jHONO reduction = 1 - $\frac{jHONO_{plume}}{jHONO_{background}}$. The $jHONO_{background}$ is obtained immediately before and after plume interception. The $jHONO_{plume}$ is represented by the transect minimal. Each data point represents the properties of one transect that encounters the largest CO enhancement in sampling one fire.

plume transects are readily identified according to the enhancement of wildfire tracers, such as CO and HCN. We identify 253 plume transects of wildfires in the western US during the campaign. These transects are indexed consecutively from 1 to 253. Because of the complex plume structure, plume transport, and variable fuels on the ground, the fire conditions and emissions may not be stationary across some transects. Therefore, transects suitable for the STA need to be scrutinized, which is carried out in the following procedure and outlined in Figure S9.

The first step is to exclude some measurements within a plume transect, because of the complex dynamics and geometry of smoke plume. For example, aircraft sampling at a constant altitude, which is a common strategy, could miss the dense portion of the plume, when one side of the plume is elevated higher than the other side, resulting from the spatially heterogeneous

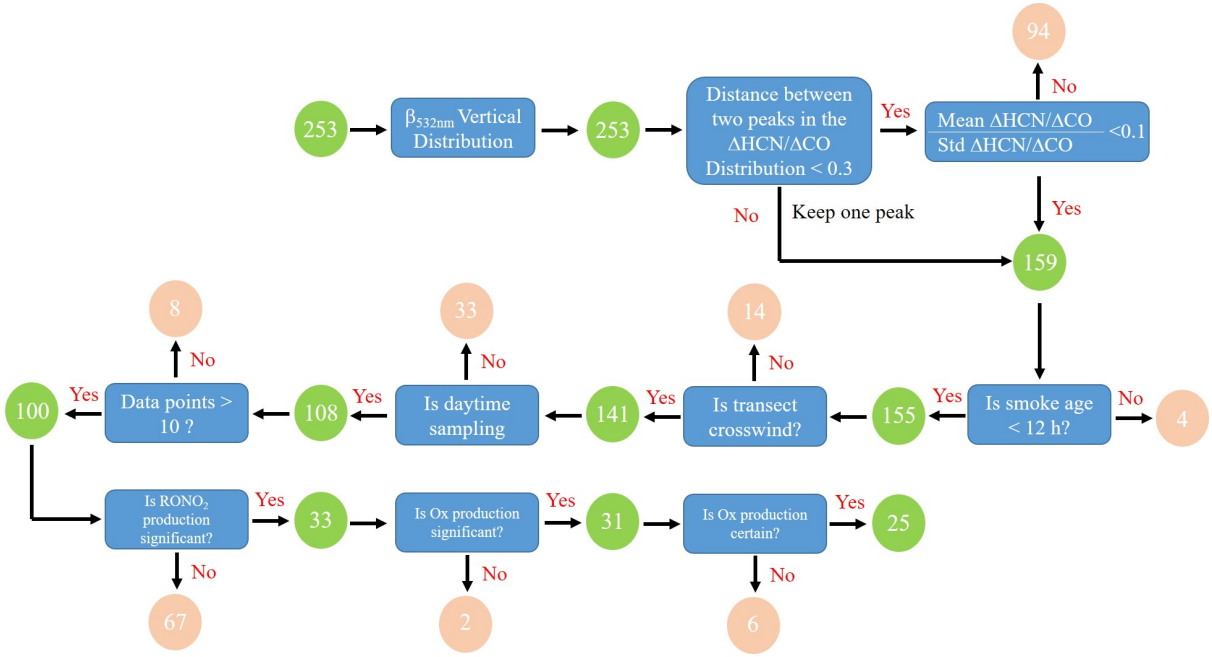

Figure S9: Flowchart to select transects suitable for the O_X chemical closure analysis. The numbers in circles represent the number of transects. Green and organge circles represent transects for which the expression is true and false, respectively. Note that the selection criteria vary with the analysis applied to single transect as described in the text. $RONO_2$ stands for hydroxynitrates.

updraft velocity beneath the plume. One case in point is shown in Figure S10a. The contour displays the vertical profile of aerosol backscatter coefficient at 532nm (β_{532nm}) as a function of time. The concentrated portion of the plume is elevated higher when the aircraft exists the plume than when it enters the plume. For further illustration, Figure S10b and S10c compare the vertical profile of β_{532nm} at two different times. At t1, the β_{532nm} measured right above the aircraft is close to that right below the aircraft, indicating the aircraft is close to the most concentrated portion of the plume. However, at t2, the β_{532nm} measured right above the aircraft is substantially larger than that right below the aircraft, indicating the aircraft merely touches the lower edge of the plume. The forward camera on the aircraft (Figure S10e) clearly shows that the thick plume is above the aircraft. After t2, the aircraft encountered another air parcel,

which has up to 20 ppbv HCN but CO_2/CO different from that before t2. In light of these observations, we utilize the vertical profile of β_{532nm} to exclude the measurements when the aircraft sampling deviates from the plume core. Specifically, the measurement at a certain time is excluded when the β_{532nm} measured right above or right below the aircraft is less than 5% of the max β_{532nm} in that vertical profile.

Next, we identify the plume transects that experience fluctuating fire emissions, which is likely influenced by the spatial variation in burning conditions. This analysis is based on the variations in ΔHCN/ΔCO across individual transects. This metric is chosen because both HCN and CO are stable plume tracers and because the emission ratio of HCN to CO depends on MCE and fuel types. ΔCO/ΔCO_2, which is directly related to MCE, is not chosen because the high and varying ambient CO_2 concentration complicates the analysis. For each plume transect, we fit the ΔHCN/ΔCO distribution using Gaussian Mixture Model (GMM) with two modes. Three example transects are shown in Figure S11. If the two modes are close (i.e., difference < 0.3) and the standard deviation of ΔHCN/ΔCO is smaller than 10% of the mean of ΔHCN/ΔCO, we assume fire emissions are relatively constant across such transect (Figure S11a). Otherwise, if the two modes are close (i.e., difference < 0.3) but the standard deviation is larger than 10% of the mean, we assume the transect experienced varying fire emissions and such transects are excluded from STA. This criterion excludes 94 transects. If the two modes are far apart (i.e., difference > 0.3, Figure S11b and c), only the mode with larger fraction of data is kept.

After identifying the transects or measurements within a transect that have relatively stable fire emissions, additional criteria are applied to select transects, depending on the analysis performed on the STA. In the combined analysis based on the O_x conceptual model and STA (denoted as O_x chemical closure analysis), we further scrutinize the transects according to the following set of stringent criteria.

1. We restrict analysis to transects that sample fresh smoke (< 12 h since emission). This

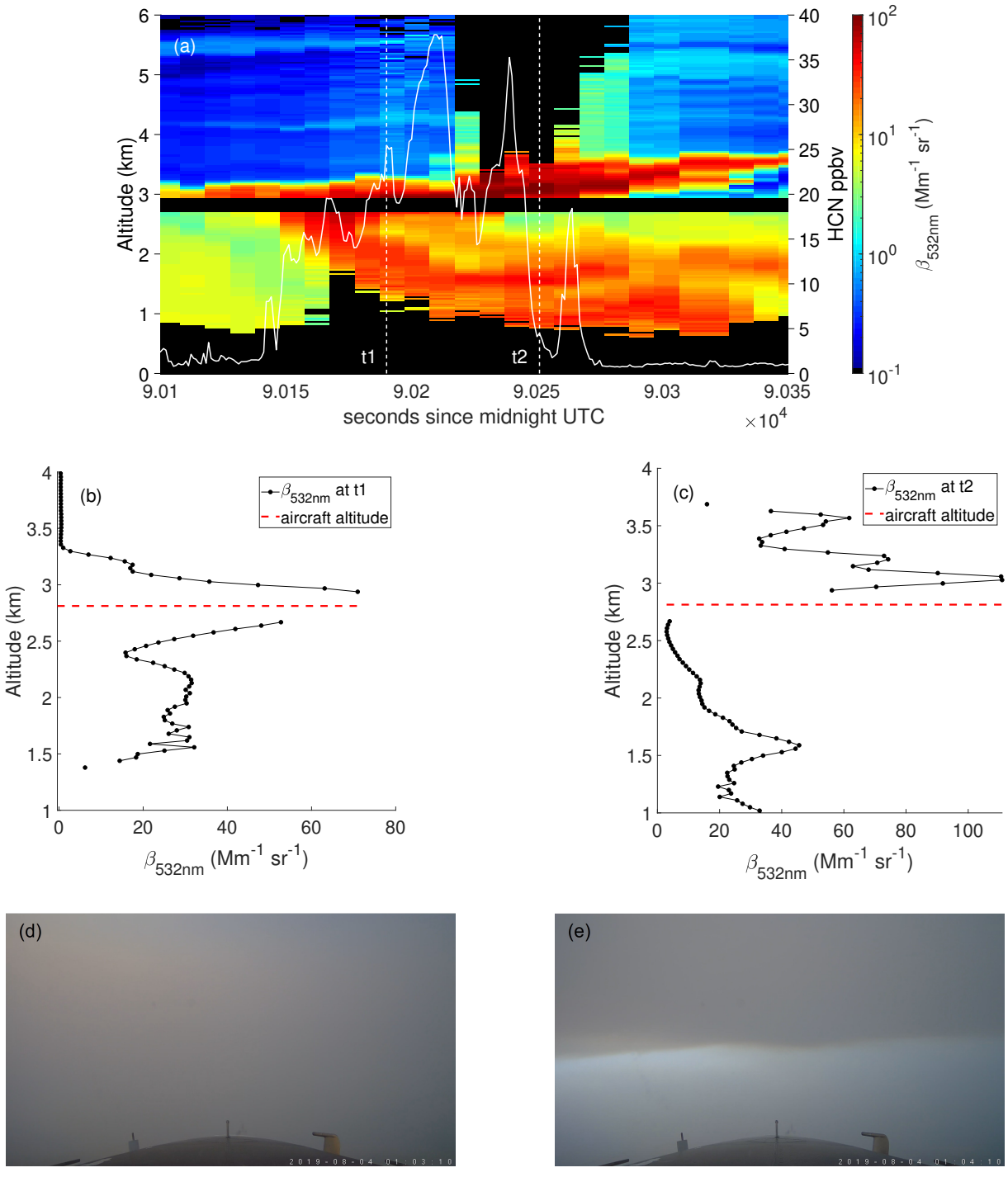

Figure S10: (a) Time series of HCN concentration and aerosol backscatter coefficient at 532nm (β_{532nm}) for one plume transect (index 108). The β_{532nm} is measured by the DIAL-HSRL instrument with a vertical resolution of 30 m. (b) The vertical profile of β_{532nm} at t1 when the aircraft flew through the thick part of the plume. (c) The vertical profile of β_{532nm} at t2 when the aircraft flew under the thick part of the plume. (d) Forward camera image taken at t1. (e) Forward camera image taken at t2. The images in panels (d) and (e) are taken by the forward camera on the DC8 aircraft.

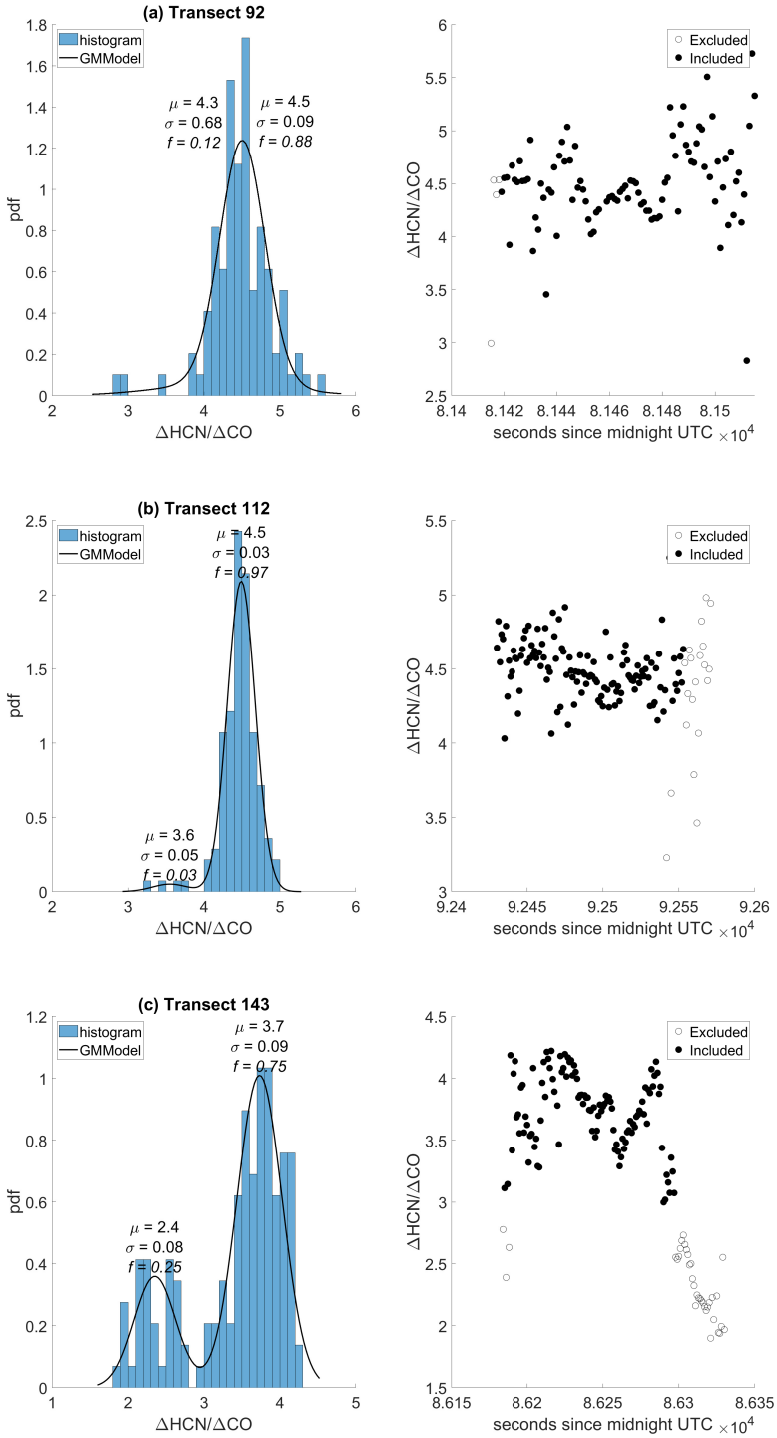

Figure S11: Gaussian Mixture Model (GMM) for three representative transects: (a) 92; (b) 112; and (c) 143. The μ, σ, and f represent the mean, variance, and the component proportion of one Gaussian mode, respectively. The black line represents the GMM fitting, which is the sum of two Gaussian functions. The black open circles in the time series of ΔHCN/ΔCO represent the measurements excluded based on both the vertical distribution of β_{532nm} and the variation in ΔHCN/ΔCO.

criterion excludes 4 transects.

2. We restrict analysis to transects that are crosswind sampling. This criteria excludes 14 transects, which are longitudinal to the smoke or have unusual sampling strategy (i.e., sampling the pyrocumulonimbus event on 8/8/2019). The longitudinal transects are excluded because the fire conditions likely changed with time.

3. We restrict analysis to transects that sample the smoke in daytime (8 am - 7 pm), because the O_x conceptual model is only applicable to daytime chemistry. This criterion further excludes 33 transects.

4. We restrict analysis to transects where there is sufficient data. A minimum of 10 data points is required to statistically test whether there is a real change in species excess ratios across one transect. This criterion further excludes 8 transects.

5. We restrict analysis to transects that have statistically significant production of hydroxynitrate ($RONO_2$, from ethene and propene oxidation). This criterion is implemented as a quality control for the f_{RO_2+NO} calculation, as the calculation requires accurate quantification of their production. The F-test is performed on the linear regression relationship between the NEMR (normalized excess mixing ratio) of $RONO_2$ and OH exposure. 67 Transects with p-value larger than 0.05 or negative slopes are excluded. Similar criterion is not applied to organic hydroperoxide (ROOH), though ROOH is also included in f_{RO_2+NO} calculation. It is because ROOH has a decreasing trend with OH exposure when ROOH loss overruns production under high NO_x conditions. In this case, the f_{RO_2+NO} is assumed to be 1, if there is a significant production of $RONO_2$. For the 67 transects that do not have significant correlation between the NEMR of $RONO_2$ and OH exposure, the NEMR of ROOH and O_x generally do not correlate with OH exposure either.

6. Similar to the criterion above, we restrict analysis to transects that have statistically significant production of O_x. This criterion excludes 2 transects.

7. Finally, we restrict analysis to transects for which the O_x production is quantified with low uncertainty. Because the O_x chemical closure analysis relies on comparing the predicted O_x production to measurement, an accurate quantification of O_x production is a prerequisite to provide a reliable diagnostic. The above criteria already limit the transects to a narrow range, but still are not sufficient to provide such confidence. To illustrate, two transects, both of which have statistically significant production of O_x, are shown in Figure S12. Regarding transect 212, the relationship between $\Delta O_x/\Delta CO$ and OH exposure is weak, such that the O_x production varies by a factor of 2 depending on how the $\Delta O_x/\Delta CO$ value at low OH exposure is determined. By contrast, transect 110 is shown as a good example in which the relationship between $\Delta O_x/\Delta CO$ and OH exposure is strong and the O_x production can be accurately calculated. Therefore, to prevent the uncertainty in calculating O_x production influence the analysis, one last criterion is implemented to exclude transects such as transect 212. This criterion is based on the distribution of the slopes determined by all pairs of sample points. Generally, broader distribution indicates weaker relationships between $\Delta O_x/\Delta CO$ and OH exposure (i.e., comparing the bottom panels in Figure S12). The transects are excluded if the standard deviation of the distribution is twice larger than the median value. This stringent criterion grants confidence to the ability to quantify the O_x production and it excludes 6 transects. Finally, 25 transects are included in the O_x chemical closure analysis.

The selection criteria vary with analysis applied to single transects. In the analysis of parameterizing the $O_3 + NO_2$ production, the criteria 6 and 7 are applied to $\Delta(O_3 + NO_2)/\Delta CO$, instead of $\Delta O_x/\Delta CO$. 39 transects are included in the analysis. In the analysis of the evolution

of f_{RO_2+NO} (Figure 5), the criteria 6 and 7 are not applied. In the analysis of f_{PAN}, criteria 5, 6, and 7 are not applied, but two other criteria are added, as will be discussed in Section S8.

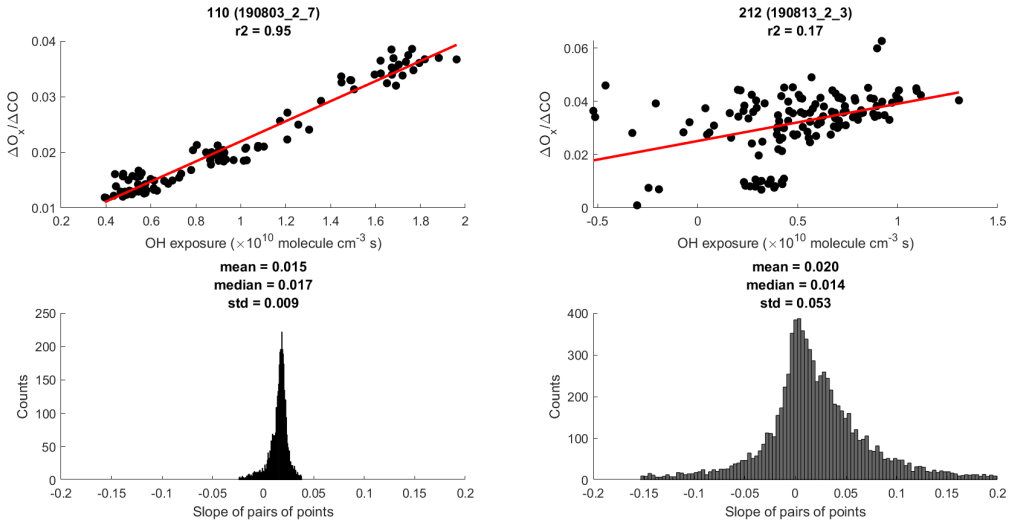

Figure S12: Two representative transects to rationalize the implementation of criterion #8. The transect in the left panels is the seventh transect during the second fire ladder on 8/3/2019. The transect in the right panels is the third transect during the second fire ladder on 8/13/2019.

5 Conceptual model to investigate O_x chemistry

This section presents the detailed derivation of the conceptual model to describe O_x formation. The derivation is conducted in a Lagrangian framework. We first derive an expression to account for dilution, then derive expressions for dilution-corrected O_x production across one transect.

The plume dilution is accounted for by normalization to inert traces, such as CO. Assume a scenario that a plume parcel with initial volume (V_{t_1}) and initial CO concentration ($[CO]_{t_1}$) is continuously mixed with ambient background air ($[CO]_{bkg}$). Then after some time at t_2, the plume parcel volume expands to V_2, with $[CO]_{t_2}$. Based on mass balance

$$[CO]_{t1} \cdot V_{t1} + [CO]_{bkg} \cdot (V_{t2} - V_{t1}) = [CO]_{t2} \cdot V_{t2} \quad \text{(S11)}$$

Rearrange Eqn.S11 to

$$([CO]_{t1} - [CO]_{bkg}) \cdot V_{t1} = ([CO]_{t2} - [CO]_{bkg}) \cdot V_{t2} \tag{S12}$$

$$\frac{[CO]_{t1} - [CO]_{bkg}}{[CO]_{t2} - [CO]_{bkg}} = \frac{V_{t2}}{V_{t1}} \tag{S13}$$

Eqn.S13 is simplified to Eqn.S14 by using the notation of excess concentration ($\Delta[X]_t = [X]_t - [X]_{bkg}$). Eqn.S14 is the fundamental equation to account for dilution.

$$\frac{\Delta[CO]_{t1}}{\Delta[CO]_{t2}} = \frac{V_{t2}}{V_{t1}} \tag{S14}$$

Next, we calculate the O_x production between t_1 and t_2 in a similar fashion. Based on mass balance,

$$[O_x]_{t_1} \cdot V_{t_1} + [O_x]_{bkg} \cdot (V_{t_2} - V_{t_1}) + O_x\_prod = [O_x]_{t_2} \cdot V_{t_2}$$

, where O_x_prod represents the number of O_x molecules produced between t_1 and t_2. The units of $[O_x]$ and V are molecules cm^{-3} and cm^3, respectively. Rearrange the above equation to

$$\begin{aligned} Ox\_prod &= ([Ox]_{t2} - [Ox]_{bkg}) \cdot V_{t2} - ([Ox]_{t1} - [Ox]_{bkg}) \cdot V_{t1} \\ &= \Delta[Ox]_{t2} \cdot V_{t2} - \Delta[Ox]_{t1} \cdot V_{t1} \end{aligned} \tag{S15}$$

After substituting the V_{t2} expression (by rearranging Eqn.(S14)) into Eqn.(S15), we obtain an expression of O_x_prod.

$$\begin{aligned} Ox\_prod &= \Delta[Ox]_{t2} \cdot \frac{\Delta[CO]_{t1}}{\Delta[CO]_{t2}} \cdot V_{t1} - \Delta[Ox]_{t1} \cdot V_{t1} \\ &= \left(\frac{\Delta[Ox]_{t2}}{\Delta[CO]_{t2}} - \frac{\Delta[Ox]_{t1}}{\Delta[CO]_{t1}} \right) \cdot \left(\Delta[CO]_{t1} \cdot V_{t1} \right) \end{aligned} \tag{S16}$$

We also derive an expression to predict the O_x_prod between t_1 and t_2 based on VOC decay and RO_2 chemistry (Figure S13) using Eqn.S17, where k_{OH+VOC_i} represents the second-order reaction rate coefficient of a VOC with OH, $[VOC_i]$ represents the VOC concentration, γ_i represents the number of peroxy radicals produced from the oxidization of one VOC_i molecule to its first-generation closed-shell products, α_i represents the alkylnitrate branching ratio of

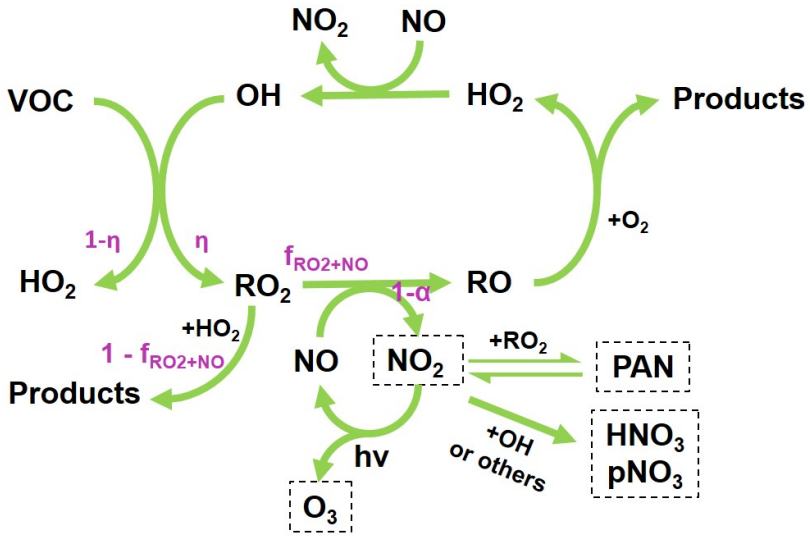

Figure S13: Simplified VOC oxidation scheme to describe the O_x conceptual model. The species in black box are collectively denoted as O_x. f_{RO_2+NO} represents the fraction of RO_2 radicals that react with NO. α represents the alkylnitrate branching ratio of RO_2+NO reaction. 1-η represents the yield of prompt HO_2 produced from the alkyl radical and O_2 reaction.

VOC_i-derived RO_2 + NO, and f_{RO_2+NO} represents the fraction of RO_2 radicals that react with NO. These parameters will be discussed in detail in Section S7 and S8. The right hand side of Eqn.S17 represents the production of NO_2, which is rapidly converted to O_3 via photolysis, to PANs via reaction with acyl peroxy radical, to nitrate (NO_3^- = HNO_3 + particulate nitrate) via oxidation. Thus, NO_2, O_3, PAN, and NO_3^- are collectively considered as O_x on the left hand side of the equation. The O_x is defined in a similar way as that in Wang et al. (*13*), but omits the oxygen atom (O), excited state of the oxygen atom ($O(^1D)$), nitrate radical (NO_3), dinitrogen pentoxide (N_2O_5), and peroxynitric acid (HO_2NO_2). These five unaccounted species are not quantified in this study, but their contributions are expected to be minor compared to other O_x species. Alkyl nitrates which are oxidation products of NO are not included in O_x.

$$\mathrm{Ox\_prod} = \int_{t_1}^{t_2} \sum_{i=1}^{i=n} \left(k_{OH+VOC_i} \cdot [VOC_i] \cdot \gamma_i \cdot (1-\alpha_i)\right) \cdot V_t \cdot f_{RO_2+NO} \cdot [OH]dt \qquad \text{(S17)}$$

By compiling the properties of individual VOC, including k_{OH+VOC_i}, $[VOC_i]$, γ_i, and α_i into a condensed parameter VOC reactivity (VOCR, Eqn.S18), Eqn.S17 is converted to Eqn.S19. f_{RO_2+NO} is assumed to be the same for all RO_2 and the associated uncertainty are discussed in Section S8.

$$VOCR_t = \sum_{i=1}^{i=n} k_{OH+VOC_i} \cdot [VOC_i]_t \cdot \gamma_i \cdot (1 - \alpha_i) \tag{S18}$$

$$Ox\_prod = \int_{t_1}^{t_2} VOCR_t \cdot V_t \cdot f_{RO_2+NO} \cdot [OH]dt \tag{S19}$$

According to Eqn.S14, $V_t = \frac{\Delta[CO]_{t1} \cdot V_{t1}}{\Delta[CO]_t}$. After substituting this V_t expression into Eqn.S19, we obtain

$$Ox\_prod = \left(\int_{t_1}^{t_2} \frac{VOCR_t}{\Delta[CO]_t} \cdot f_{RO_2+NO} \cdot [OH]dt \right) \cdot \left(\Delta[CO]_{t1} \cdot V_{t1} \right) \tag{S20}$$

Finally, equating Eqn.S16 and Eqn.S20, both of which describe O_x production, we obtain

$$\frac{\Delta[Ox]_{t2}}{\Delta[CO]_{t2}} - \frac{\Delta[Ox]_{t1}}{\Delta[CO]_{t1}} = \int_{t_1}^{t_2} \frac{VOCR_t}{\Delta[CO]_t} \cdot f_{RO_2+NO} \cdot [OH]dt \tag{S21}$$

We further transform the integral in time dimension to integral in OH exposure dimension and arrive at Eqn.S22. The right hand side of Eqn.S22 integrates from the fresh plume (i.e., lowest OH exposure) to the aged plume (i.e., highest OH exposure) across one plume transect.

$$\left(\frac{\Delta[O_x]}{\Delta[CO]}\right)_{aged} - \left(\frac{\Delta[O_x]}{\Delta[CO]}\right)_{fresh} = \int_{fresh}^{aged} \frac{VOCR_{[OH]t}}{\Delta[CO]_{[OH]t}} \cdot f_{RO_2+NO} \cdot d([OH]t) \tag{S22}$$

The left hand side of Eqn.S22, which represents the measured O_x production, is calculated from the measurements of individual O_x species (i.e., O_3, NO_2, PANs, HNO_3, and particulate nitrate). After adding individual O_x species to obtain the O_x concentration, we determine the percentile values of $\Delta O_x/\Delta CO$ under each OH exposure by treebagger algorithm. This algorithm uses bootstrap samples of the data to grow the bootstrap-aggregated (bagged) decision

trees to reduce overfitting and improve generalization. The treebagger algorithm is preferred in this study because the measurements in the $\Delta O_x/\Delta CO$ vs. OH exposure relationship are not uniformly distributed and bootstrap-aggregated analysis provides more robust percentiles. We employ the TreeBagger function for Matlab and 500 bagged classification trees are used. Lastly, the difference in the median value of $\Delta O_x/\Delta CO$ between aged (i.e., >95th percentile of OH exposure) and fresh portion (i.e., <5th percentile of OH exposure) of one transect represents the O_x production in that transect.

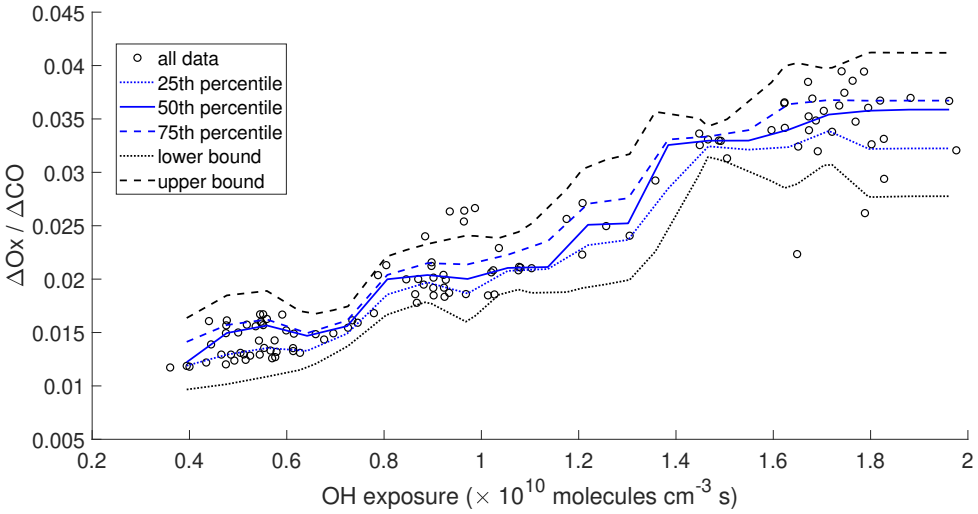

Figure S14: The plot of NEMR of O_x vs. OH exposure from one plume transect to illustrate the outliers identified based on treebagger algorithm. The lower and upper bounds represent the 25th percentile - interquartile and 75th percentile + interquartile, respectively.

The right hand side of the equation, representing the predicted O_x production based on VOC decay, is calculated from the measured VOCs, OH exposure, and RO_2 fate. The integral is represented by product of f_{RO_2+NO} and the area under curve in the $\frac{VOCR_t}{\Delta[CO]_t}$ vs. OH exposure plot (see Figure S23 as an example). f_{RO_2+NO} is factored out of the integral by applying the transect-averaged value, which assumes that f_{RO_2+NO} does not vary with OH exposure. The details on f_{RO_2+NO} are discussed in Section S8.

Several points regarding the conceptual model should be noted.

1. The measurements of NO_y and individual reactive nitrogen compounds (including NO, NO_2, HONO, HNO_3, particulate nitrate, and PANs) enable a diagnosis on the chemical closure of NO_y. Figure S15 shows that the sum of individual reactive nitrogen compounds equals the measured NO_y within measurement uncertainties, indicating no apparent missing NO_y species in this study. This analysis also suggests that alkyl nitrates, the sum of which is not measured in this study, comprise a small fraction of NO_y. To further investigate the contribution of alkyl nitrates to NO_y, we estimate the production of alkyl nitrates based on the decay of measured VOCs. According to Eqn.S23, the area under the curve in the plot of instantaneous production rate of alkyl nitrates ($P_{\text{alkyl nitrates}}$) as a function of OH exposure represents the amount of alkyl nitrates produced. We estimate that when OH exposure is 2×10^{10} molecules cm^{-3} s (equivalent to 5 h smoke age assuming [OH] = 1×10^6 molecules cm^{-3}), the produced alkyl nitrates account for less than 10% of NO_y. This estimate is consistent with above NO_y chemical closure analysis and also consistent with previous observations in ARCTAS studies (*20, 62*), where total NO_y measurements were available. A recent study by Calahorrano et al. (*19*) measured individual NO_y species in western wildfires in 2018 and reported that gas phase organic nitrates comprise 20-25% of NO_y, a fraction larger than the estimate in this and previous studies. Because a lack of total NO_y measurement, the NO_y chemical closure analysis in Calahorrano et al. (*19*) has larger uncertainty. In addition, the concentration of gas-phase organic nitrates in that study could be biased high because of a factor of 2 uncertainty in the calibration factors as noted in Calahorrano et al. (*19*).

$$\text{produced alkyl nitrates} = \int_{([OH]t)_1}^{([OH]t)_2} \sum_{i=1}^{i=n} k_{OH+VOC_i} \cdot \frac{[VOC_i]}{\Delta[CO]} \cdot \alpha_i \cdot f_{RO_2+NO} \cdot d([OH]t)$$
$$= \int_{([OH]t)_1}^{([OH]t)_2} P_{\text{alkyl nitrates}} d([OH]t) \quad \text{(S23)}$$

2. While the particulate nitrate measured by AMS is a sum of particulate inorganic nitrate, alkyl nitrates, and nitroaromatics (both -NO_2 and -OH groups attached to the aromatic ring), multiple lines of evidence suggests that inorganic nitrate is the predominant species. Both Positive Matrix Factorization (PMF) analysis and analysis based on the NO^+/NO_2^+ ratio suggest alkyl nitrates account for less that 5% of AMS nitrate. Regarding nitroaromatics, preliminary analysis estimates that nitroaromatics account for less than 10% of AMS nitrate (molar ratio) for 75% of all transects. In fact, as the formation of nitroaromatics involves NO_2 loss (i.e., phenoxy radicals + NO_2), they are included in the O_x calculation.

3. The stoichiometirc coefficient for HNO_3 and particulate nitrate in O_x is assumed to be 1. The underlying assumption is that the major formation pathway of HNO_3 is the oxidation of NO_2 by OH, as the HNO_3 produced via other pathways, for example N_2O_5 with H_2O, involves more than 1 odd oxygen (*63*). To test this hypothesis, we compare the measured production of NO_3^- (i.e., sum of HNO_3 and AMS nitrate) across individual transects to the predicted production based on the decay of $\Delta NO_2/\Delta CO$ as a function of OH exposure (Eqn. S24), in a similar fashion as O_x chemical closure analysis. As shown in Figure S16, the predicted NO_3^- production from NO_2+OH reaction agrees reasonably with the measurement, implying this reaction is the major source of inorganic nitrate. Other formation pathways of inorganic nitrate, including N_2O_5 uptake and nitrate radical + aldehdyes, play a minor role. However, we acknowledge that the importance of nitrate

radical chemistry in optically dense plumes warrants further investigations.

$$NO_3^- \text{ production} = \int_{([OH]t)_1}^{([OH]t)_2} k_{NO_2+OH} \cdot \frac{[NO_2]}{\Delta[CO]} \cdot d([OH]t) \quad \text{(S24)}$$

4. The O_3 consumption by reactions with alkenes is not included, as the reaction is assumed to be O_3 neutral.

5. As the conceptual model solely based on gas phase chemistry is sufficient to account for the measured O_x production here, we do not need to assign a significant role for the heterogeneous loss of O_3 and HO_2. This finding is supported by comparing the heterogeneous loss rate of HO_2 (Eqn.S25) and its loss via reaction rate with NO (Eqn.S26). γ in Eqn.S25 is the HO_2 uptake coefficient and it depends on aerosol composition. We use γ = 0.008, which is based on measurements of HO_2 uptake to a variety of organic aerosols (*64*). This choice is reasonable because organic aerosol generally accounts for more than 90% of submicron PM mass in wildfire plumes. ν is the mean molecular speed of HO_2, which is 437 m s^{-1} at 280 K. SA is the particle surface area and we use the largest value $\sim 10^5 \mu m^3/cm^3$ sampled from the Williams Flats fire on 8/3/2019. Together, $r_{HO_2,het}$ is 0.09 s^{-1}. At the same time when the largest SA was sampled, the NO concentration, ambient T, and ambient P are 6500 ppt, 280 K, and 729 hPa, respectively. Using these values, the r_{HO_2+NO} is 1.1 s^{-1}, which is one order of magnitude larger than $r_{HO_2,het}$. This analysis supports the conclusion that heterogeneous loss of HO_2 is minor.

$$r_{HO_2,het} = \frac{\gamma \times \nu \times SA}{4} \quad \text{(S25)}$$

$$r_{HO_2+NO} = k_{HO_2+NO}[NO] \quad \text{(S26)}$$

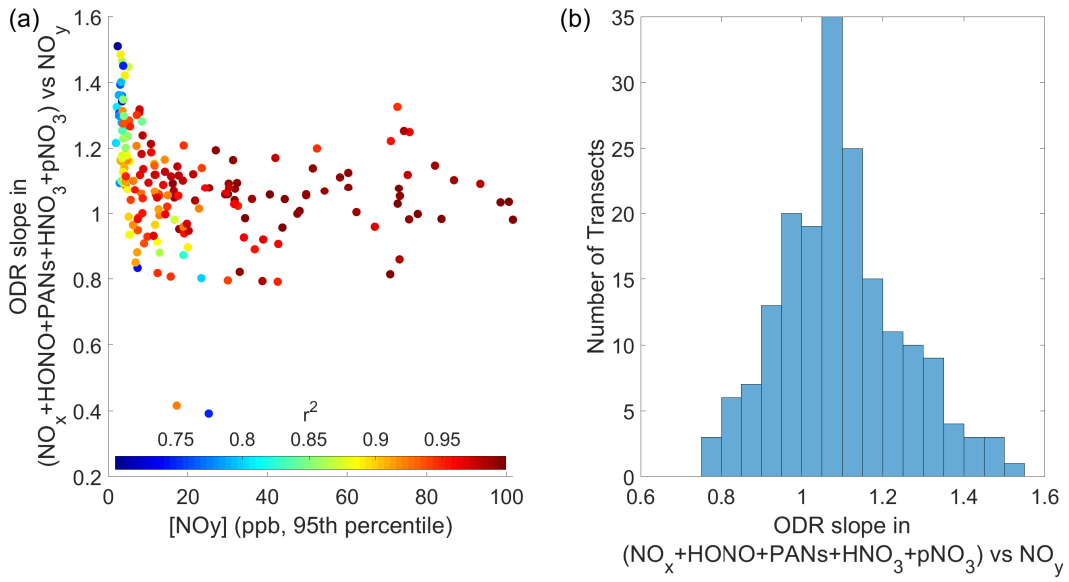

Figure S15: Analysis of NO_y closure. The NO_y closure is studied based on the correlation of summed NO_y species (as y-axis, including NO, NO_2, HONO, PANs, HNO_3, and particulate nitrate (pNO_3)) and measured NO_y (as x-axis). The orthogonal fitting is performed on individual transects. Panel (a) plots the orthogonal slope as a function of the 95% percentile of the NO_y concentration from the corresponding transect. Each data point represents one transect and is colored by the r^2 of the linear correlation of summed vs. measured NO_y. Only transects with r^2 larger than 0.7 are shown. Panel (b) plots the histogram of the orthogonal fitting slopes.

6 Statistical model to estimate the O_x background level

When quantifying the O_x enhancement in smoke plume (i.e., $\frac{\Delta[O_x]}{\Delta[CO]} = \frac{[O_x]_{plume}-[O_x]_{bkg}}{[CO]_{plume}-[CO]_{bkg}}$), a critical source of uncertainty is the relatively high O_3 concentration outside the plume. To represent the O_x background concentration (denoted as $[O_x]_{bkg}$), previous aircraft studies typically used the air upwind of the fire source or the concentration obtained immediately before and after plume interception (*7, 9, 32*). However, these estimates can be biased when the background air composition near the surface where the fire is emitted is different from that aloft where the smoke is sampled (*65*).

To take the airmass origin into account in estimating the $[O_x]_{bkg}$, we apply multivariate

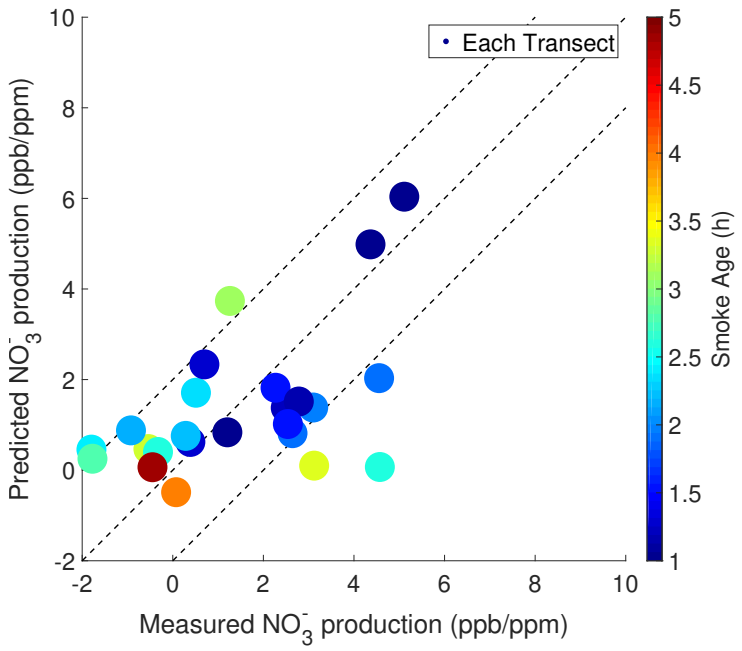

Figure S16: The comparison of predicted and measured production of NO_3^-. The prediction is based on the decay of $\Delta NO_2/\Delta CO$ as a function of OH exposure.

linear regression (MLR) to relate $[O_x]_{bkg}$ on several predictors, including water vapor concentration ($[H_2O]$), HCN concentration ([HCN]), longitude (Lon), latitude (Lat), temperature (T), pressure (P), and hour of day (HoD). The MLR is applied to each individual fire ladder. In the statistical model, the dependent variable is the O_x concentration outside of the wildfire plumes (i.e., $[O_x]_{bkg}$). The explanatory variables include $[H_2O]$, [HCN], Lon, Lat, T, P, and HoD. The $[H_2O]$ is included in the regression analysis because its strong vertical gradient helps to represent the airmass origin. For example, during the plume rise from surface to aloft, the composition of background air is constantly changing. The background composition immediately before and after the plume intercept may not accurately represent that of the plume core, which has undergone less extensive mixing with background air than plume edge. Using $[H_2O]$ enables a more accurate estimate of various extent of mixing that different portions of plume have experienced. The RH is $< 100\%$ in the plume transects, indicating the H_2O is conserved

in transport. We also verify that the H_2O emission from the wildfires due to combustion is insignificant compared to ambient H_2O level. The [HCN] is included in the regression analysis to represent the widespread fire impacts on the regional O_x background. As discussed below, [HCN] significantly increases the explanatory power (correlation) of the statistical model. Longitude, Latitude, and P (equivalently altitude) are selected to represent the spatial distribution of O_x. T is selected to represent the effects of temperature on O_3 chemistry.

We perform stepwise selection regression using stepwisefit function in Matlab. It adds terms to and removes terms from a multilinear model based on their statistical significance (F-statistics, p-value = 0.05). Based on the stepwise selection, the explanatory power of each predictor is explored. Taking the second fire ladder on 08/03/2019 as an example, all predictors arranged in descending explanatory power are H_2O, HCN, Lon, P, T, Lat, and HoD (Table S2). All explanatory variables have a statistically significant relationship with the dependent variable. Notably, H_2O and HCN together explain 73% of the variance in the measured $[O_x]_{bkg}$ ($r^2 = 0.73$), while other predictors explain additional 6% of the variance and hence increase the r2 to 0.79. The relative importance of these predictors vary with flights, but generally follow a similar trend as the second fire ladder of 8/3/2019 flight.

For all 26 fire ladders, the statistical model explains 44-94% (median value 79%) of variance in the measurements (Figure S17). The performance of the statistical model for one fire ladder is shown in Figure S18 as an example. Outside of the plume, the $[O_x]$ predicted by the statistical model well matches the measured $[O_x]$ for this particular case. Finally, we apply the regression coefficients from the statistical model to estimate point-wise $[O_x]_{bkg}$ inside the wildfire plume. We use the in situ measurements of $[H_2O]$, longitude, latitude, temperature, pressure, hour of day, and regional average [HCN]. The regionally average [HCN] is represented by the average of all outside plume measurements collected during the corresponding fire ladder.

Predictor[a]	Estimate	SE	p-value	cumulative $r^{2,b}$
intercept	5.4e2	72	9.5e-14	-
H_2O	-2.1e-3	5.5e-5	4.4e-264	0.32
HCN	8.8e-3	1.5e-4	0	0.73
Lon	2.7	0.52	1.9e-7	0.77
P	0.099	0.013	2.1e-14	0.78
T	-0.69	0.13	1.9e-7	0.79
Lat	-1.2	0.26	2.5e-6	0.79
HoD	0.66	0.23	3.6e-3	0.79

[a] The multivariate regression equation takes the following form: $[O_x]_{bkg} = \beta_0 + \beta_1 \times [H_2O] + \beta_2 \times [HCN] + \beta_3 \times Lon + \beta_4 \times P + \beta_5 \times T + \beta_6 \times Lat + \beta_7 \times [HoD]$

[b] the r^2 value of each line represents the model performance when the predictors in this line and above are included in the model.

Table S2: Multivariate Linear regression model to estimate $[O_x]_{bkg}$ for the second fire ladder on 08/03/2019.

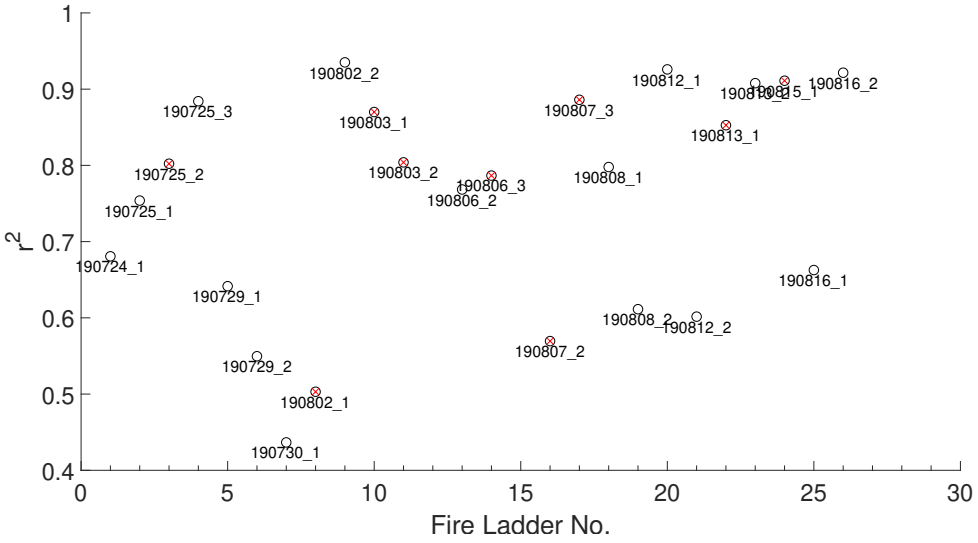

Figure S17: The performance of O_x statistical model (i.e., the r^2 between measured and modeled O_x concentration outside of wildfire plumes) for each fire ladder. The statistical model is not developed for the first fire ladder on 08/06/2019 and 08/07/2019, because they sampled aged smoke and the sampling strategy is different from other fire ladders. The plume transects included in Figure 7 are from the fire ladder with red cross.

7 VOC reactivity

VOC reactivity (VOCR) is a condensed parameter summarizing several properties of individual VOC (Eqn.S18), including the VOC concentration ($[VOC_i]$), the second-order reaction rate

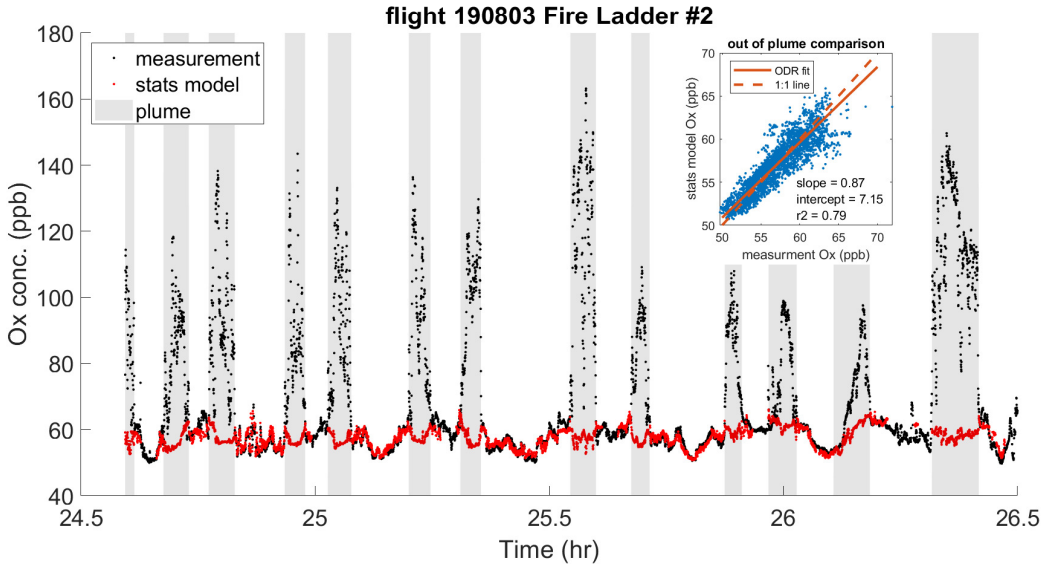

Figure S18: An example fire ladder (i.e., the second fire ladder on 08/03/2019) to illustrate the performance of O_x statistical model. The red line represents the modeled O_x background concentration. The difference between red and black line represents the O_x enhancement in the plume. The missing prediction for some periods is due to missing HCN measurement because of instrument background calibration. The inset panel plots the measured vs. predicted O_x concentration outside of the plume.

coefficient of a VOC with OH (k_{OH+VOC_i}), the number of RO_2 and HO_2 molecules produced in the process of oxidizing one VOC_i molecule to its first-generation closed-shell products (γ_i), and the alkylnitrate branching ratio of VOC_i-derived RO_2 + NO (α_i). These related parameters are summarized Tables S3, S4, S5, and will be discussed in detail below.

VOC species

Roughly 80 VOC species are included in the analysis. They include ∼40 species quantified by PTR-ToF-MS, ∼40 species quantified by the NOAA integrated whole air sampler (iWAS) with GC-MS analysis, CH_4 by DACOM, C_2H_6 by CAMS, HCHO by ISAF, CHOCHO by ACES, phenol by CF_3O^- CIMS. All the species have 1Hz measurements, except iWAS.

For all flights except the one on 8/7/2019, the VOCs measurements by the NOAA PTR-ToF-

MS are used. The NOAA PTR-ToF-MS was not operational because of power issue during the 8/7/2019 flight, so that the measurements collected by the PTR-ToF-MS from the University of Oslo (denoted as UIO PTR) were used. The UIO PTR focused on measuring NH_3 and only provided VOCs measurements for 8/7/2019 flight. Measurement of CH_3CHO by the UIO PTR is unavailable and we use the average contribution of CH_3CHO to total VOC reactivity from 20 transects included in the O_x chemical closure analysis, which is 13%, as an approximation of the CH_3CHO reactivity during the 8/7/2019 flight.

One limitation in the PTR-ToF-MS measurement is that it cannot distinguish isobaric compounds and their isomers. To address this issue, we assume the isomer distribution follows that identified by gas chromatography at the Fire Sciences Laboratory in 2016 by Koss et al. (*15*).

Another issue with the VOC measurements is that some compounds are sticky in sampling lines. This issue causes partition delay and a long tail when the aircraft exits the smoke plume, which may cause positive bias in the calculated VOC reactivity. This issue is largely avoided when the analysis focuses on the the concentrated portion of the plume when the phenol and benzene concentrations are 10 times higher than that in the background level.

Reaction rate coefficient of VOC with OH (k_{OH+RH})

The k_{OH+RH} are collected from the National Institute of Standards and Technology's Chemical Kinetics Database and (*66*). The temperature-dependent rate coefficients are applied whenever data are available.

Photolysis of aldehdyes

Besides OH-initiated oxidation of VOCs, the photolysis of aldehydes is another important source of radicals. Here, we convert the in situ photolysis rate of 9 aldehydes to an equivalent second-order reaction rate coefficients of VOC+OH reaction, by assuming an OH concentration

($k_{aldehyde+OH,eqv} = J_{aldehyde}/[OH]$). In this study and in the literature, the estimated [OH] in wildfire plumes ranges from 1×10^6 to 1.7×10^7 molecules cm^{-3} (*9, 67–69*). Here, we assume [OH] = 1×10^6 molecules cm^{-3}. The 9 aldehydes included in this analysis are acetaldehyde, acetone, propanal, methacrolein, methyl vinyl ketone, glyoxal, formaldehyde, methyl ethyl ketone, and hydroxyacetone. Their in situ photolysis rates are determined from the Charged-coupled device Actinic Flux Spectroradiometers. Several photolysis pathways could exist for the aldehydes. Here we only include the pathways that leading to primary radical productions. For example, we only consider the photolysis rate of HCHO that produces H and HCO.

Discussions about α

α represents the alkylnitrate branching ratio of RO_2 + NO reaction. Overall, we use measured α when available and estimate α by analogy to a closely related compound when measurement is unavailable. The α values of alkanes are obtained from the summary in Rosen et al. (*70*). The α values of alkenes are based on the measurements in Teng et al. (*71*) or calculated using the parameterization in Wennberg et al. (*72*) if measurements are not available. The α values of aromatics are highly uncertain. For example, a recent study by Xu et al. (*60*) measured the α to be <1% in OH-initiated oxidation of benzene and suggested the α values in current chemical mechanisms are largely overestimated (i.e., 8% in Master Chemical Mechanism for benzene). Given the lack of comprehensive measurements of α values of aromatics, we assume α=1% for all aromatics measured in this study. Similar to aromatics, the α values of furans are also sparsely studied in the literature. We apply the parameterization in Wennberg et al. (*72*) to calculate the α for furan, which is 5%. This value is applied for all furans. The α of C_1-C_3 carbonyls is zero. C_4 and larger carbonyls are assume to have the same α as methacrolein (i.e., 6% (*72*)).

Discussions about γ

The γ value represents the number of RO_2 and HO_2 molecules produced in the process of oxidizing one VOC_i molecule to its first-generation closed-shell products. The γ value for each individual VOC is evaluated based on its oxidation mechanism. The simplified and generic VOC oxidation scheme is shown in Figure S13, based on which the derivation of γ is illustrated below. The OH-initiated oxidation of VOCs typically produces an alkyl radical. In the oxidation of alkenes and alkanes, the alkyl radical quickly adds O_2 to become a RO_2. In the oxidation of aromatics and furans, the reaction of alkyl radicals and O_2 can proceed with H abstraction to produce a prompt HO_2 and a closed-shell product as counterpart. Given such difference between VOCs, the yield of RO_2 (represented by η) is considered to derive a generic γ expression. Next, depending on the reaction environment, a fraction of RO_2 reacts with NO (f_{RO_2+NO}) to produce alkoxy radical (RO) with a branching ratio $(1-\alpha)$, where α is the alkylnitrate branching ratio. Lastly, alkoxy radical is assumed to exclusively react with O_2 to produce a HO_2 and a counterpart aldehyde (*73*). Based on this simplified oxidation scheme, $\gamma = 1 + \eta f(1-\alpha)$. We further simplify the expression and approximate γ as $1 + \eta$, by assuming f is equal to 1 and α is equal to 0. These two assumptions are reasonable because f is generally larger than 0.6 in smoke plumes as shown in Section S8 and α values for the majority of measured VOCs in this study are smaller than 0.1 (Table S3 and S4). The γ under these assumptions represents an upper estimate.

According to the simplified γ expression, we estimate the γ of each VOC. For alkenes and C_1-C_3 alkanes, γ is 2, because η is equal 1. This is the typical γ value used in the literature, and the implicit assumptions (i.e., f = 1 under high-NO_x and α = 0) made to derive this value should be clearly acknowledged. For C_4 and higher alkanes, the alkoxy radical isomerization (not considered in Figure S13) becomes competitive, which produces additional RO_2 and leads to γ larger than 2. For these alkanes, we assume γ = 2.85 as estimated by Rosen et al. (*70*). For

aromatics and furans, the yield of prompt HO_2 (i.e., 1-η) is critical in γ estimation. The yields of prompt HO_2 of several common aromatics are measured by Nehr et al. (*73*), which ranges from 0.27 to 0.89 depending on aromatic speciation. When a measurement is unavailable, such as syringol and guaiacol, we assume their η to be the same as benzene. The yields of prompt HO_2 of furans are also substantial based on theoretical studies, but experiment values are largely unavailable. The yields are estimated from a series of theoretical studies on furans oxidation mechanism (*74, 75*). The γ estimation for aldehydes is challenging because aldehydes undergo both OH oxidation and photolysis, which result in different γ values. Another challenge is that the acyl peroxy radical produced from aldehydes oxidation can react with NO_2 to produce PAN, instead of recycling NO_x. Overall, we assume γ=2 for all aldehydes, except HCHO. Regarding HCHO, γ=1 when HCHO reacts with OH and γ=2 when it photolyzes to CO+2HO_2. HCHO photolysis to H2 and CO is not included in the analysis because this reaction does not produce primary radicals. Further, we estimate that the branching ratio of OH oxidation and photolysis to CO+2HO_2 is roughly half and half in the plume, leading to γ=1.5 for HCHO.

iWAS interpolation

The NOAA iWAS sampling interval is 4-9 s, depending on altitude. If a VOC is quantified by both PTR and iWAS, the 1Hz PTR measurement is used in the analysis and the iWAS measurement is excluded to avoid double counting. The VOCs uniquely measured by iWAS are treated as a group with a concentration-weighted reaction rate with OH ($k_{iWAS+OH,eff}$, Eqn.S27). Their combined reactivity is interpolated into 1s intervals by scaling to a species that has similar k_{OH} as $k_{iWAS+OH,eff}$ and is measured with 1Hz frequency.

$$k_{iWAS+OH,eff} = \frac{\sum_{i=1}^{i=n} \left(k_{OH+VOC_i} \cdot [VOC_i]\right)}{\sum_{i=1}^{i=n} [VOC_i]} \quad \text{(S27)}$$

The $k_{iWAS+OH,eff}$ is close to k_{OH} of xylene isomers. To illustrate, Figure S19 displays the $k_{iWAS+OH,eff}$ of each fire ladder, calculated using the iWAS species concentrations averaged

over the entire fire ladder. The $k_{iWAS+OH,eff}$ of all fire ladders are within the k_{OH} range bounded by o-xylene and m-xylene. 1Hz measurements of xylene isomers are available by PTR-ToF-MS measurement, despite all isomers being collectively measured as C8-aromatics. All unique iWAS species were treated as a group and assumed to decay at the same rate as C8-aromatics. To interpolate discrete iWAS measurement into 1Hz frequency for each plume transect, we first calculate the VOC reactivity including all unique iWAS species (denoted as $VOCR_{iWAS,slow}$), then divide it by the C8-aromatics concentration averaged over the iWAS sampling interval, and lastly multiply it by the 1Hz measurement of C8-aromatics across that transect (Eqn.S28).

$$VOCR_{iWAS,fast} = \frac{VOCR_{iWAS,slow}}{[C8-aromatics]_{PTR,slow}} \times [C8-aromatics]_{PTR,fast} \quad (S28)$$

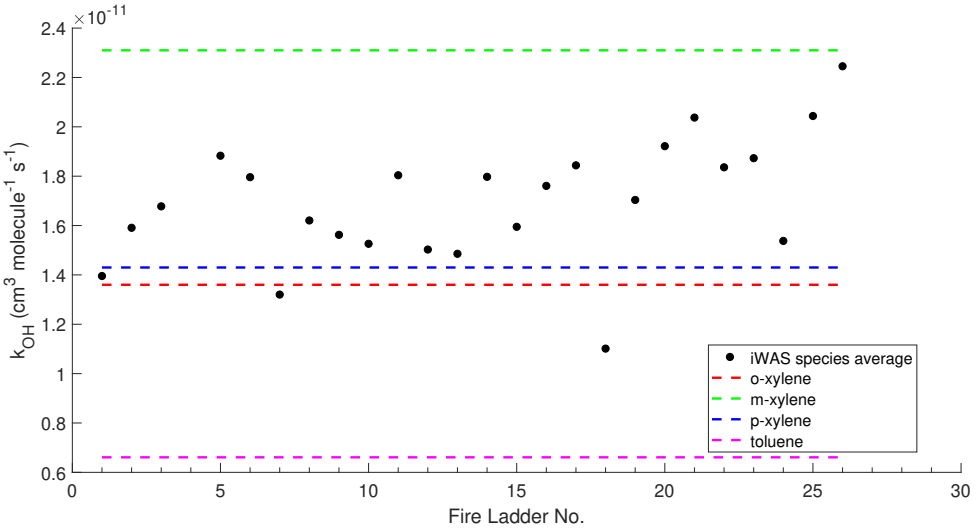

Figure S19: The concentration-weighted k_{OH} of unique VOC species (i.e. $k_{iWAS+OH,eff}$) measured by NOAA iWAS for each fire ladder. The secondary reaction rate coefficients of VOCs with OH are calculated at 280 K.

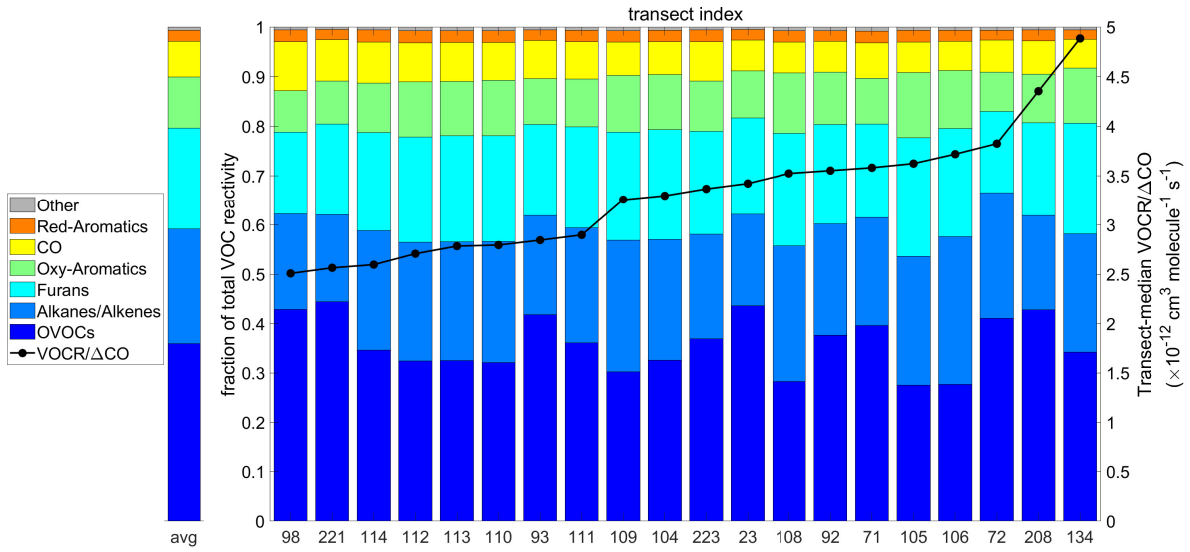

Figure S20: Contribution to total VOC reactivity (VOCR) of different VOC categories in the 21 transects selected in the chemical closure of O_x analysis (SI Appendix, Section S4). 4 transects from the flight on 8/7/2019, which are also included in the O_x chemical closure analysis, are not shown here, because the CH_3CHO measurement is unavailable. The numbers along x-axis represent the transect index. Oxygenated VOCs (OVOCs) are predominantly small carbonyls, with minor contributions of organic acids and alcohols. Red-Aromatics and Oxy-Aromatics stand for reduced and oxygenated homocyclic aromatic compounds, respectively.

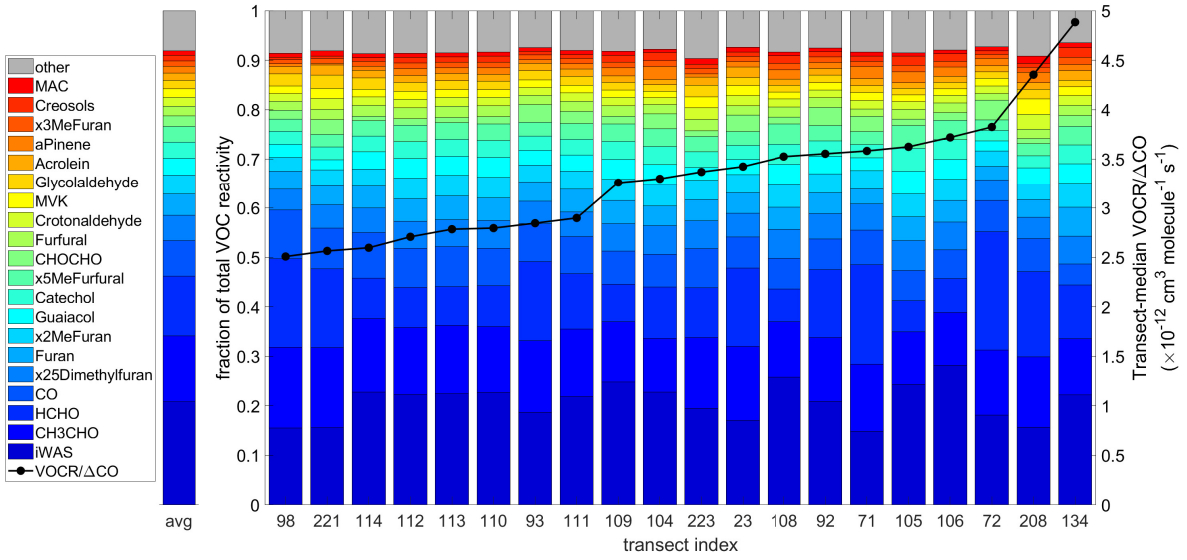

Figure S21: The fractional contribution of the top 20 VOCs to total VOC reactivity for the 21 plume transects selected in the O_X chemical closure analysis (Section S4). 4 transects from the flight on 8/7/2019, which are also included in the O_X chemical closure analysis, are not shown here, because the CH_3CHO measurement is unavailable. The numbers along x-axis represent the transect index.

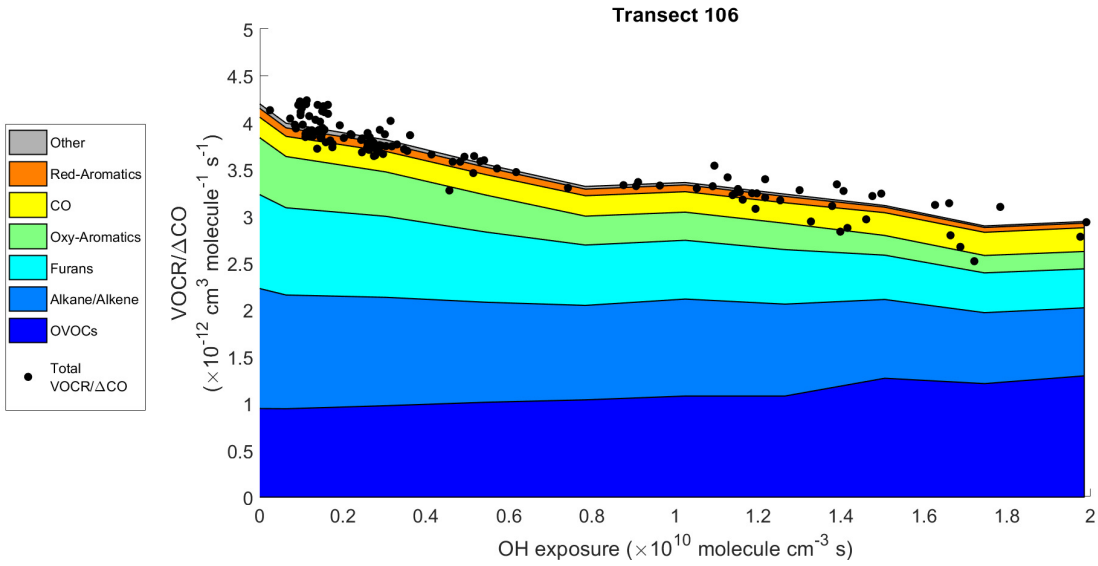

Figure S22: The OH-exposure-dependent VOC reactivity in a representative transect. The total VOCR/Δ CO (black dots) is from 1Hz measurements. The VOCR of each VOC class (colorful areas) is binned based on OH exposure.

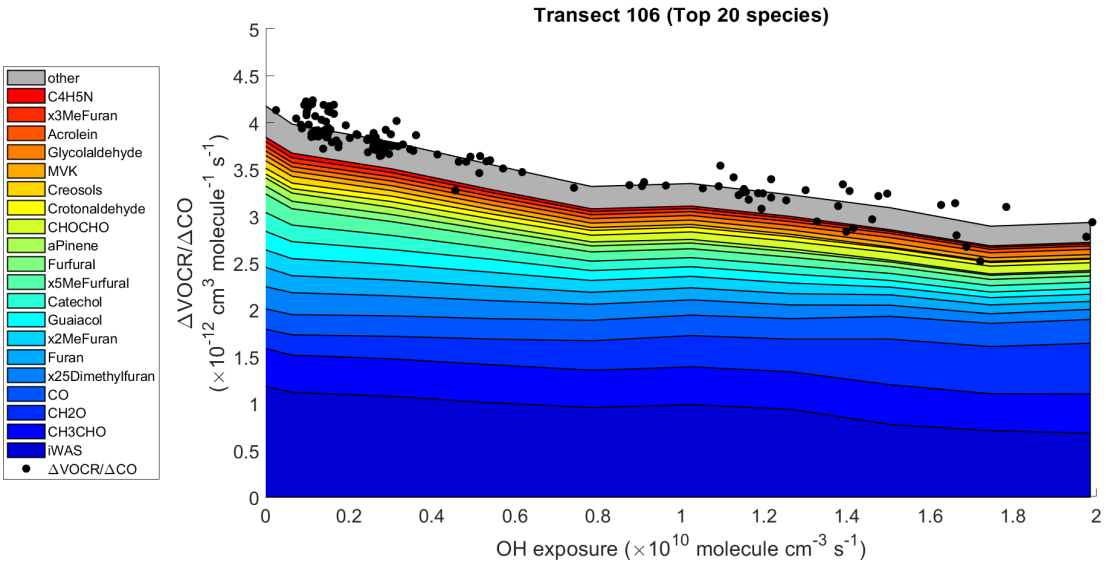

Figure S23: The OH-exposure-dependent VOC reactivity of top 20 species in one representative plume transect (index 106).

VOC[a]	A[b]	n	B	γ	α
c2Butene	1.10e-11	0	-487	2	0.12
c2Pentene	6.50e-11	0	0	2	0.15
CycHexane	3.26e-17	2	-262	2.85	0.17
Ethene	1.96e-12	0	-438	2	0.013
iButane	1.17e-17	2	-213	2.85	0.255
iButene	9.47e-12	0	-504	2	0.09
iPentane	3.60e-12	0	0	2.85	0.35
isoprene	2.70e-11	0	-390	2	0.13
MeCycHexane	9.64e-12	0	0	2.85	0.17
MeCycPentane	2.73e-17	2	-214	2.85	0.1
nButane	1.81e-17	2	-114	2.85	0.077
nDecane	3.17e-17	2	-406	2.85	0.3
nHexane	2.54e-14	1	112	2.85	0.141
nNonane	2.53e-17	2	-436	2.85	0.05
nOctane	2.72e-17	2	-361	2.85	0.226
nPentane	2.52e-17	2	-158	2.85	0.105
Propane	1.65e-17	2	87	2	0.036
Propene	4.85e-12	0	-504	2	0.041
t13Pentadiene	1.01e-10	0	0	2	0.03
t2Butene	1.01e-11	0	-550	2	0.12
t2Pentene	6.70e-11	0	0	2	0.15
x1Butene	6.55e-12	0	-467	2	0.12
x1Pentene	3.14e-11	0	0	2	0.15
x224TriMePentane	2.35e-17	2	-140	2.85	0.14
x22DiMeButane	3.37e-11	0	809	2.85	0.2
x24DiMePentane	4.77e-12	0	0	2.85	0.1
x2Me1Butene	6.10e-11	0	0	2	0.16
x2MePentane	5.20e-12	0	0	2.85	0.14
x3Me1Butene	5.32e-12	0	-533	2	0.03
x3MePentane	5.20e-12	0	0	2.85	0.14

[a] All iWAS species are classified as Alkane/Alkene.

[b] The units of A and b are cm^3 $molecule^{-1}$ s^{-1} and K, respectively. The rate expression is $k = AT^n e^{-B/T}$. B = 0 suggests the temperature-dependent rate constant is not available. This footnote also applies to Tables S4 and S5

Table S3: Summary of VOCs measured by NOAA iWAS.

VOC	Class	A	n	B	γ	α	note
Acetone	OVOCs	9.84e-13	0	485.52	2	0	
Acrolein	OVOCs	6.55e-12	0	-333.17	2	0	
Anisol	OVOCs	2.80e-11	0	0	1.13	0.01	50% of C_7H_8O
aPinene	Alkane/Alkene	1.21e-11	0	-436	2	0.03	100% of $C_{10}H_{16}$
Benzaldehyde	Oxy-aromatics	1.3e-11	0	0	2	0.06	
Benzene	Red-aromatics	2.33e-12	0	193	1.5	0.01	
BenzFuran	Furans	3.72e-11	0	0	1.5	0.05	
Butanal	OVOCs	5.71e-12	0	-411.35	2	0.06	1% of C_4H_8O
C_2H_5OH	OVOCs	5.31e-12	0	180.42	1	0	
Catechol	Oxy-aromatics	1.00e-10	0	0	1	0.01	50% of $C_6H_6O_2$
CH_3CHO	OVOCs	6.87e-12	0	-256.19	2	0	
CH_3COOH	OVOCs	2.44e-14	0	-1027.13	2	0	67% of $C_2H_4O_2$
CH_3OH	OVOCs	6.71e-12	0	600.19	1	0	
Creosols	Oxy-aromatics	7.5e-11	0	0	1.13	0.01	
Crotonaldehyde	OVOCs	5.77e-12	0	-532.84	2	0.06	33% of C_4H_6O
EthylBenzene	Red-aromatics	7.51e-12	0	0	1.6	0.01	10% of C_8H_{10}
EthylFormate	OVOCs	5.66e-13	0	-133.51	2	0	14% of $C_3H_6O_2$
Furan	Furans	1.32e-11	0	-334	1.24	0.05	
Furfural	Furans	3.50e-11	0	0	1	0.05	
Glycoaldehyde	OVOCs	8.00e-12	0	0	2	0	33% of $C_2H_4O_2$
Guaiacol	Oxy-aromatics	7.44e-11	0	0	1.5	0.01	
HCOOH	OVOCs	2.91e-13	0	-102.24	1	0	
Hydroxyacetone	OVOCs	1.88e-11	0	544.86	2	0	50% of $C_3H_6O_2$
HydroxyBenzoquinone	Oxy-aromatics	4.60e-12	0	0	1.5	0.01	$C_6H_4O_3$
isobutyraldehyde	OVOCs	6.79e-12	0	-393.31	2	0.06	14% of C_4H_8O
Methacrolein	OVOCs	8.00e-12	0	-380	2	0.06	19% of C_4H_6O
MaleicAnhydride	Furans	1.45e-12	0	0	1.24	0.05	
MEK	OVOCs	1.20e-12	0	0	2	0	85% of C_4H_8O
MethylAcetate	OVOCs	8.54e-19	2	-455	2	0	35% of $C_3H_6O_2$
MVK	OVOCs	2.60e-12	0	-610	2	0.03	48% of C_4H_6O
Naphthalene	Red-aromatics	1.05e-12	0	-902.09	2	0.01	
Styrene	Red-aromatics	4.30e-11	0	0	2	0.01	
Syringol	Oxy-aromatics	1.00e-10	0	0	1.5	0.01	
Toluene	Red-aromatics	2.09e-12	0	-322.35	1.58	0.01	
oXylene	Red-aromatics	1.47e-11	0	0	1.6	0.01	23% of C_8H_{10}
mXylene	Red-aromatics	1.66e-11	0	-115.47	1.6	0.01	34% of C_8H_{10}
pXylene	Red-aromatics	1.52e-11	0	0	1.6	0.01	34% of C_8H_{10}
Trimethylbenzene	Red-aromatics	1.32e-11	0	-449.84	1.67	0.01	C_9H_{12}
x23Butanedione	Alkane/Alkene	2.41e-13	0	0	2	0.05	
x25Dimethylfuran	Furans	1.32e-10	0	0	1.73	0.05	DimeFurans
x2Furanone	Furans	4.10e-12	0	0	2	0.05	
x2MeFuran	Furans	6.18e-11	0	0	1.65	0.05	85% of C_5H_6O
x3MeFuran	Furans	3.2e-11	0	-310.32	1.65	0.05	15% of C_5H_6O
x2Methylphenol	Oxy-aromatics	4.00e-11	0	0	1.13	0.01	50% of C_7H_8O
x5MeFurfural	Furans	5.10e-12	0	0	2	0.05	50% of $C_6H_6O_2$

Table S4: Summary of VOCs measured by PTR-ToF-MS. Red-Aromatics and Oxy-Aromatics stand for reduced and oxygenated homocyclic aromatic compounds, respectively.

VOC	Class	A	n	B	γ	α
HCHO	OVOCs	6.84e-12	0	-72.17	1.5	0
CH_4	Alkane/Alkene	1.85e-20	2.82	984	2	5e-4
CHOCHO	OVOCs	1.10e-11	0	0	2	0
CO	CO	1.5e-13	0	0	1	0
Ethane	Alkane/Alkene	1.49e-17	2	499	2	0.019
Phenol	Oxy-aromatics	4.70e-13	0	-1220	1.11	0.01

Table S5: Summary of VOCs measured by instruments other than PTR-ToF-MS and iWAS.

8 RO_2 fate

8.1 Calculations of RO_2 fate

The fraction of RO_2 that reacts with NO (f_{RO_2+NO}) is inferred from the production of a pair of organic hydroperoxide (ROOH) and hydroxynitrate ($RONO_2$) from the same parent VOC. The instantaneous production rates of ROOH and $RONO_2$ are written as Eqn.S29 and S30, where k_{RO_2+NO} and $k_{RO_2+HO_2}$ represent the reaction rate coefficients of RO_2 + NO and RO_2 + HO_2 reactions, respectively. α_{RONO_2} and α_{ROOH} represent the branching ratio to produce $RONO_2$ and ROOH, respectively. Then f_{RO_2+NO} is expressed using P_{ROOH}, P_{RONO_2}, α_{ROOH}, and α_{RONO_2}, as in Eqn.S31.

$$P_{RONO_2} = k_{RO_2+NO} \cdot \alpha_{RONO_2} \cdot [RO_2] \cdot [NO] \tag{S29}$$

$$P_{ROOH} = k_{RO_2+HO_2} \cdot \alpha_{ROOH} \cdot [RO_2] \cdot [HO_2] \tag{S30}$$

$$\begin{aligned} f_{RO_2+NO} &= \frac{k_{RO_2+NO} \cdot [NO]}{k_{RO_2+NO} \cdot [NO] + k_{RO_2+HO_2} \cdot [HO_2]} \\ &= \frac{\frac{P_{RONO_2}}{\alpha_{RONO_2}}}{\frac{P_{RONO_2}}{\alpha_{RONO_2}} + \frac{P_{ROOH}}{\alpha_{ROOH}}} \end{aligned} \tag{S31}$$

We use measurements of ROOH and $RONO_2$ from the OH-initiated oxidation of ethene and propene for this analysis. These two VOCs are selected because the corresponding ROOH and $RONO_2$ are accurately measured by CF_3O^- CIMS with high sensitivity and minor interference. Also, the α_{ROOH} and α_{RONO_2} for these two VOCs are relatively well-studied (*71*). The α_{ROOH} in both ethene and propene oxidation is assumed to be 1. The α_{RONO_2} values are estimated by scaling the laboratory measurements in Teng et al. (*71*) to the atmospheric conditions using the temperature and pressure dependencies described in Wennberg et al. (*72*). Under common sampling conditions (280 K and 700 hPa), the α_{RONO_2} values are 1.8% and 5.2% for ethene

and propene, respectively. The measured production of X (X = ROOH or $RONO_2$) across an entire transect is represented by the difference in $\Delta X/\Delta CO$ values between aged (i.e., >95th percentile of OH exposure) and fresh portion (i.e., <5th percentile of OH exposure) of one transect. Because the production of ROOH and $RONO_2$ across the entire transect is applied in Eqn.4, the calculated f_{RO_2+NO} represents a transect-integrated metric. The secondary loss of ROOH and $RONO_2$ is corrected by using the rate coefficients of their reaction with OH and the estimated OH exposure, following the procedure in Atkinson et al. (*76*). The f_{RO_2+NO} is calculated for both ethene and propene, and they are consistent within 10% as shown in Figure S25. The average value from both systems of each transect is applied in predicting the O_x formation across each transect.

Applying the f_{RO_2+NO} derived from ethene and propene to larger VOCs introduces uncertainty in predicting the O_x formation. It is mainly because $k_{RO_2+HO_2}$ increases with the number of heavy (non-hydrogen) atoms in RO_2, while the k_{RO_2+NO} does not vary significantly with RO_2 size (*72*). Therefore, the f_{RO_2+NO} is expected to decrease with larger RO_2 size. We estimate such uncertainty based on the dependence of $k_{RO_2+HO_2}$ on temperature and the number of heavy atoms (n = C + O + N - 2) (*72*). Under typical flight temperature 280K, the $k_{RO_2+HO_2}$ increases from $1.8\times\ 10^{-11}$ cm^3 $molecule^{-1}$ s^{-1} for propene-derived RO_2 to a plateau value of $2.7\times\ 10^{-11}$ cm^3 $molecule^{-1}$ s^{-1} for RO_2 with n larger than 11. Applying the plateau value of $k_{RO_2+HO_2}$ decreases the estimated f_{RO_2+NO}, but the change is more pronounced when f_{RO_2+NO} is small. or example, when the propene-derived f_{RO_2+NO} is 0.6 (i.e., the lowest value of the 25 transects in Figure 7), applying the plateau value of $k_{RO_2+HO_2}$ decreases the f_{RO_2+NO} to 0.5, a 17% change. In contrast, the change is only 5% When the propene-derived f_{RO_2+NO} is 0.9. Overall, applying the ethene- and propene-derived f_{RO_2+NO} introduces a small positive bias in the predicted O_x formation and such bias is considered in the uncertainty analysis.

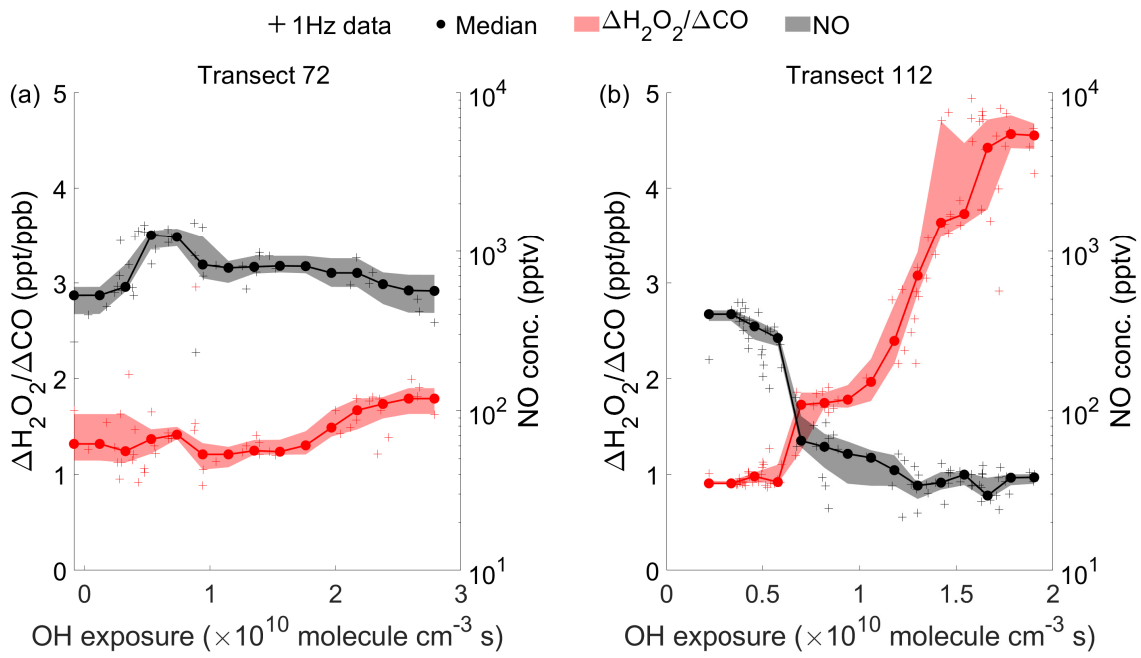

Figure S24: The NO concentration and NEMR of H_2O_2 as a function of OH exposure for two transects under different NO levels.

8.2 Discussions on NO_x loss pathways

Potential NO_x loss pathways include oxidation to inorganic nitrate (NO_3^-), NO_2 reaction with acyl peroxy radical to produce PANs, NO reaction with RO_2 to produce alkyl nitrates, NO_2 reaction with phenoxy radicals to produce nitroaromatics. Four PANs (listed in Table S1), gas phase HNO_3, and particulate nitrate are quantified in this study. Particulate nitrate measured by AMS is dominantly inorganic nitrate, with minor contribution from nitroaromatics and alkylnitrates, as discussed in Section S5. The measurement of the sum of all gas-phase alkyl nitrates is not available. Thus, to investigate the chemical closure of NO_x oxidation products, we compare the sum of PANs and NO_3^- (= HNO_3 + particulate nitrate) to NO_z across each transect. NO_z is calculated by subtracting NO_x and HONO from measured NO_y. As shown in Figure S27, the sum of PANs and NO_3^- equals the measured NO_z within measurement

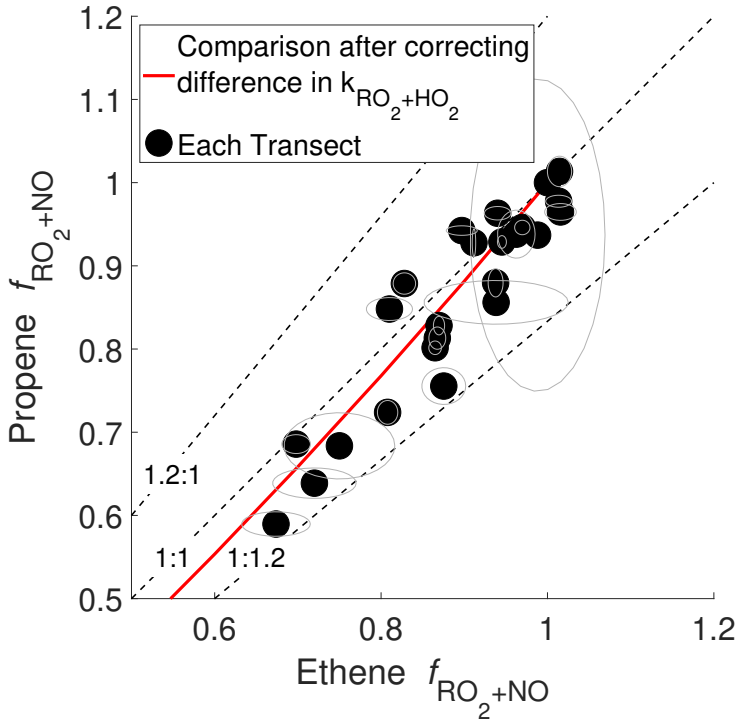

Figure S25: Comparison of f_{RO_2+NO} estimated from ethene and propene systems. The eclipse represents the estimation uncertainty. For a few transects, the estimated f_{RO_2+NO} is greater than 1, which is because the ROOH exhibits a decreasing trend with increasing OH exposure as a result of chemical removal and lack of production. For these transects, the f_{RO_2+NO} is set to 1 in further analysis (i.e., predict O_x formation using Eqn.3). The red line represents the theoretical relationship between ethene and propene f_{RO_2+NO} after accounting for the $k_{RO_2+HO_2}$ dependence on RO_2 size. The difference between ethene-derived and propene-derived f_{RO_2+NO} is quantified by comparing the black points and the red line.

uncertainties (Table S1). Therefore, this analysis suggests that PANs and NO_3^- are the dominant NO_x oxidation products and other NO_x loss pathways play a relatively minor role. This finding is consistent with previous studies (*6, 20, 67*). Among all four PANs (i.e, PAN, PBN, PPN, and APAN, Table S1) measured in this study, PAN accounts for more than 90%.

To investigate the relative contribution of NO_x loss pathways, we use STA and calculate the fraction of PAN in the newly formed NO_z (NO_z = NO_y - NO_x - HONO) across each transect (denoted as f_{PAN}) by exploring the relation of $\Delta PAN/\Delta CO$ and $\Delta NO_z/\Delta CO$. f_{PAN} is calculated using two methods. The first method uses the ratio of the difference in the 95th and

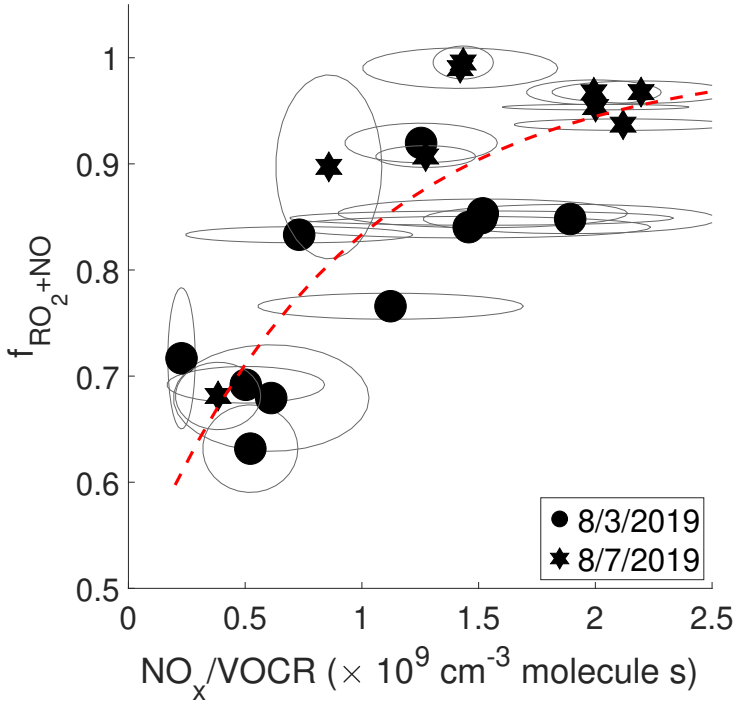

Figure S26: The relationship between f_{RO_2+NO} and NO_x/VOCR. The red line is provided as a visual aid.

5th percentiles of ΔPAN/ΔCO to that of $\Delta NO_z/\Delta CO$. The second method uses the slope of the orthogonal fitting of the ΔPAN/ΔCO vs. $\Delta NO_z/\Delta CO$ (an example transect is shown in Figure S28). The f_{PAN} of one transect is considered as robust and included in further analysis, only if the values calculated from two methods agree within 30% and ΔPAN/ΔCO vs. $\Delta NO_z/\Delta CO$ has a reasonable correlation ($r^2 > 0.5$). In Figure 6b, only fire ladders having more than 4 robust transects are included, in order to show the f_{PAN}evolution.

Here f_{PAN} represents the fraction of NO_x loss to PAN as the smoke evolved from the photochemical condition in plume center to that in plume edge across individual transects. It is different from the average $\Delta PAN/\Delta NO_z$ of one transect, which depends on the primary emissions of NO_z species and the integral of NO_x chemical loss from emission to be sampled. The f_{PAN} as a function of smoke age is shown in Figure 5b.

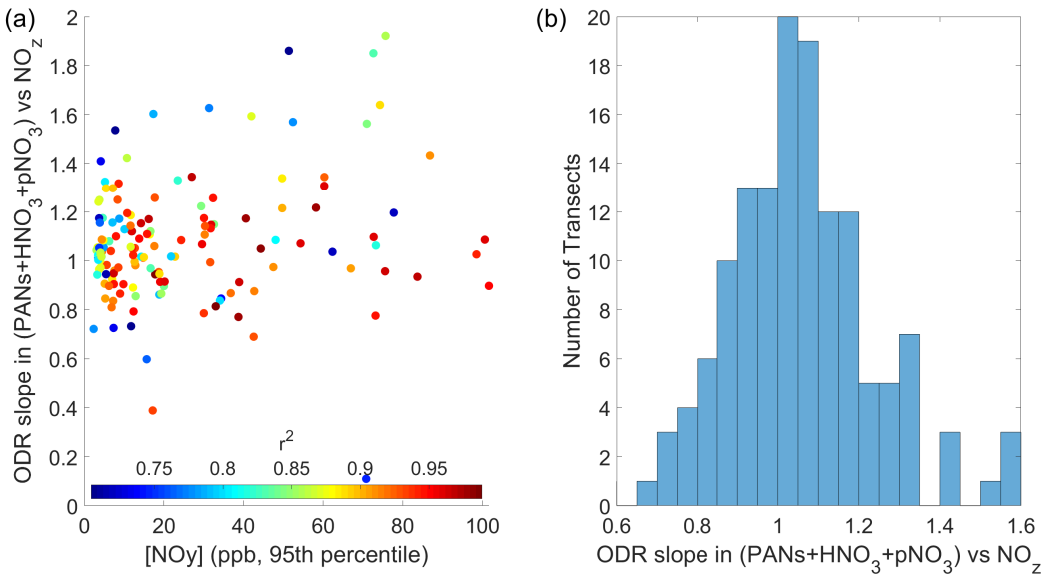

Figure S27: Analysis of NO_z closure. The NO_z closure is studied based on the correlation of summed NO_z species (as y-axis, including PANs, HNO_3, and pNO_3) and measured NO_z (ax x-axis, = NO_y - NO - NO_2 - HONO). The orthogonal fitting is performed on individual transects. Panel (a) plots the orthogonal slope as a function of the 95% percentile of the NO_y concentration from the corresponding transect. Each data point represents one transect and is colored by the r^2 from the least square fit of summed and measured NO_z. Only transects with r^2 larger than 0.7 are shown. Panel (b) plots the histogram of the orthogonal fitting slopes.

$$P_{PAN} = k_{CH_3CO_3+NO_2}[NO_2][CH_3CO_3] \tag{S32}$$

$$\begin{aligned}\frac{d[CH_3CO_3]}{dt} &= k_{CH_3CHO+OH}[CH_3CHO][OH] \\ &\quad - k_{CH_3CO_3+NO_2}[CH_3CO_3][NO_2] \\ &\quad - k_{CH_3CO_3+NO}[CH_3CO_3][NO] \\ &\quad - k_{CH_3CO_3+HO_2}[CH_3CO_3][HO_2]\end{aligned} \tag{S33}$$

$$[CH_3CO_3] = \frac{k_{CH_3CHO+OH}[CH_3CHO][OH]}{k_{CH_3CO_3+NO_2}[NO_2] + k_{CH_3CO_3+NO}[NO] + k_{CH_3CO_3+HO_2}[HO_2]} \tag{S34}$$

$$P_{HNO_3} = k_{NO_2+OH}[NO_2][OH] \tag{S35}$$

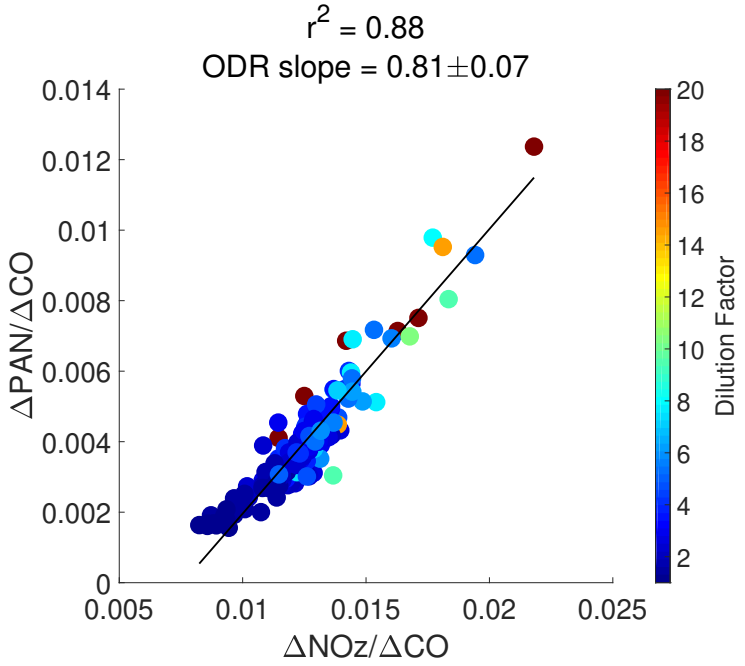

Figure S28: Scatter plot of ΔPAN/ΔCO vs. $\Delta NO_z/\Delta CO$ for transect 105. The slope is from orthogonal fit.

$$\frac{P_{PAN}}{P_{HNO_3}+P_{PAN}} = \frac{1}{1+\frac{k_{NO_2+OH}[NO_2]}{k_{CH_3CHO+OH}[CH_3CHO]}(1+\frac{k_{CH_3CO_3+NO}[NO]}{k_{CH_3CO_3+NO_2}[NO_2]}+\frac{k_{CH_3CO_3+HO_2}[HO_2]}{k_{CH_3CO_3+NO_2}[NO_2]})} \quad \text{(S36)}$$

In addition to obtaining f_{PAN} based on measured ΔPAN/ΔCO and $\Delta NO_z/\Delta CO$, f_{PAN} is estimated based on the production rates of PAN and HNO_3, assuming they are the only two NO_x oxidation products. The production rate of PAN from the reaction of NO_2 and acetyl peroxy radical (CH_3CO_3) is shown in Eqn.S32. The CH_3CO_3 concentration is estimated by assuming equilibrium between its production from OH oxidation of acetaldehyde and its reactions with NO, NO_2, and HO_2 (Eqns. S33 and S34). The production rate of HNO_3 from the oxidation of NO_2 by OH is shown in Eqn.S35. The measured HNO_3 in wildfire plumes is very low (i.e., a few ppt), because HNO_3 rapidly partitions to particles together with abundant NH_3 emitted from wildfires to become particle-phase NH_4NO_3. Combining S32, S34, and

Eqn.S35 leads to Eqn.S36, which is used to estimate the f_{PAN}, based on concentrations of NO, NO_2, and acetaldehyde. We apply the median value of species concentrations across each transect in Eqn.S36. The CH_3CO_3 + HO_2 reaction is considered to derive a complete expression, but dropped out in the final calculation because of a lack of information on HO_2 concentration. The f_{PAN} calculated by Eqn.S36 is denoted as "theoretical f_{PAN}", as opposed to that calculated based on measured ΔPAN/ΔCO and $\Delta NO_z/\Delta$CO (denoted as "measured f_{PAN}"). The measured and theoretical f_{PAN} is compared in Figure S29. The comparison is by no means expected to be perfect, but rather provide some confidence that the theoretical f_{PAN} based on a few species can reproduce the dependence of measured f_{PAN} on smoke age (Figure 5b).

Figure 5b shows that the measured f_{PAN} is about 0.2-0.4 at a smoke age of 0.5 h, rapidly increasing to $\sim$0.8-1 at 2 h, and is relatively stable afterwards. This trend suggests that the major NO_x oxidation product transits from NO_3 to PAN. According to Eqn. S36, two factors influence this transition, [CH_3CHO]/[NO_2] and [NO_2]/[NO]. The [CH_3CHO]/[NO_2] ratio influences the fate of OH and the [NO_2]/NO ratio influences the fate of CH_3CO_3. The evolution of both factors is shown in Figure S30. As smoke ages, the [CH_3CHO]/[NO_2] ratio increases because NO_2 is chemically lost to other NOy species, but CH_3CHO has secondary production from the oxidation of VOCs. Such change in [CH_3CHO]/[NO_2] causes a larger fraction of OH to react with CH_3CHO than with NO_2, which produces more CH_3CO_3 and favors PAN formation. In contrast, the fraction of CH_3CO_3 that reacts with NO_2 is relatively constant with increasing OH exposure (Figure S30b). Therefore, the change in f_{PAN} as a function of smoke age is mainly driven by the change in [CH_3CHO]/[NO_2]. However, one caveat in this analysis is that the CH_3CO_3 + HO_2 reaction is not considered in the analysis. Along with NO_x depletion, a larger fraction of CH_3CO_3 likely react with HO_2, resulting in a decrease in f_{PAN} in the far-field of smoke plumes. Lastly, we note that the produced amount of PAN depends on not only

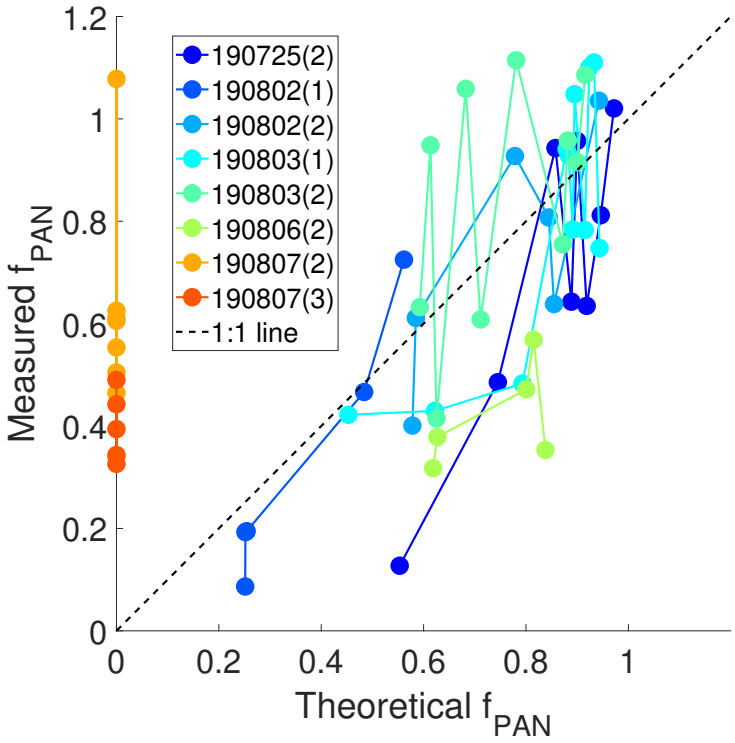

Figure S29: The comparison between measured and calculated fraction of NO_x loss to PAN. Only transects with $r^2 > 0.5$ in the measured $\Delta PAN/\Delta CO$ vs. $\Delta NO_z/\Delta CO$ relationship are included in this figure. Further, only fire ladders with more than four transects satisfying the above criteria are shown. The theoretical f_{PAN} is 0 for 190807(2) and 190807(3), because CH_3CHO measurement is not available on this flight.

the fraction of NO_x lost to PAN, but also the abundance of NO_x. Even though PAN is the dominant oxidation products of NO_x after ~2 h transport, the majority of PAN is produced in the relatively fresh part of the plume, because of large abundance of NO_x.

In Figure 6b, the transects from the third fire ladder on 8/7/2019 (i.e., 190807(3)) have smaller f_{PAN} than other transects under similar smoke age. This is likely because of low CH_3CHO/NO_2 of 190807(3) transects. As the CH_3CHO measurement is not available on 8/7/2019 flight, we use $HCHO/NO_2$ as a proxy of CH_3CHO/NO_2. As shown in Figure S31, the $HCHO/NO_2$ ratios of transects from 190807(3) are generally lower than that of other transects under similar smoke age. Different $HCHO/NO_2$ and CH_3CHO/NO_2 under similar smoke age is

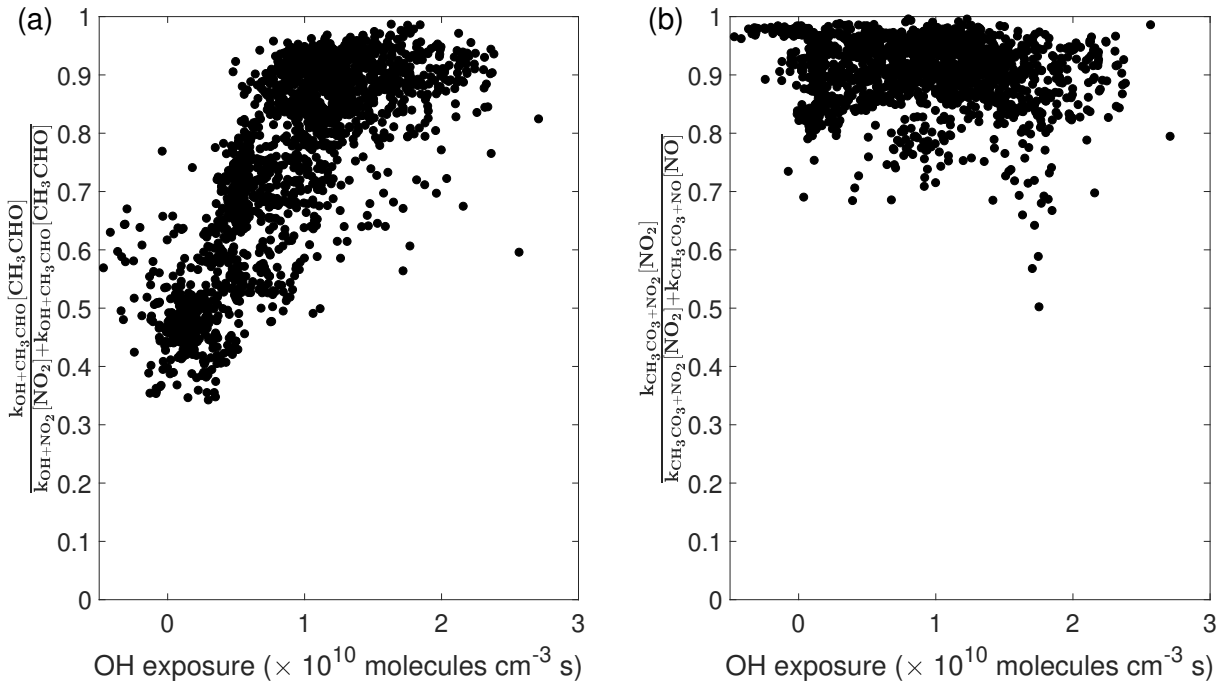

Figure S30: (a) The evolution of the fraction of CH_3CHO+OH reaction rate in the summed reaction rates of CH_3CHO+OH and NO_2+OH for 8/3/2019 Williams Flats Fire. (b) The fraction of CH_3CO_3 reacts with NO_2 as a function of OH exposure for the same fire as panel (a).

expected as they are affected by several factors, including initial emission ratios and the extent of photochemical processing.

Figure 6a uses the measurements from the second fire ladder on 8/3/2019 flight (denoted as 190803(2)) as an example to show the evolution of NO_y species as the smoke chemically ages. The $\Delta PAN/\Delta NO_y$ increases with OH exposure and then plateaues. The plateau value of $\Delta PAN/\Delta NO_y$ shows large variability between different fires and it ranges from 0.35 to 0.5. We find that the plateau value has a strong dependence on MCE. In the following analysis, we replace OH exposure, which is used in Figure 6a, with $\Delta NO_z/\Delta NO_y$ as a proxy for photochemical aging. This replacement is mainly because the calculation of OH exposure has strict requirements (i.e., both phenol and benzene concentrations are at least 10 times higher than the background values) and a fraction of measurements are excluded as a result. $\Delta NO_z/\Delta NO_y$ indicates photochemical

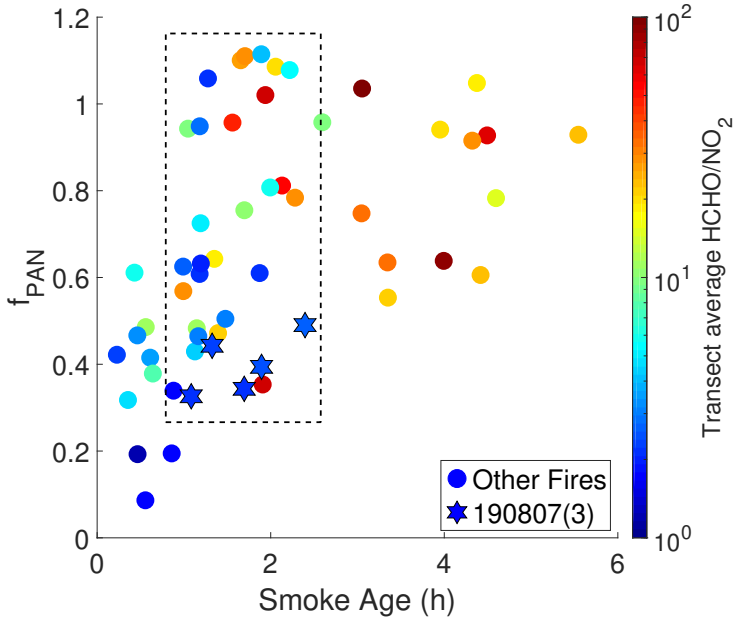

Figure S31: The fraction of PAN in the newly produced NO_z (f_{PAN}) in each transect of several sampling fire ladders as a function of smoke age. The data points are colored by the transect-average HCHO/NO_2, which is used as a proxy for CH_3CHO/NO_2.

processing because NO_x is converted to NO_z as the smoke ages, leading to higher $\Delta NO_z/\Delta NO_y$. Figure S32 shows that the $\Delta PAN/\Delta NO_y$ increases with $\Delta NO_z/\Delta NO_y$ for 190803(2) measurements. This is consistent with previous observations that $\Delta PAN/\Delta NO_y$ increases with smoke age and then plateaues (*6, 19, 20*). Next, we calculate the median $\Delta PAN/\Delta NO_y$ of observations of which the $\Delta NO_z/\Delta NO_z$ is between 0.9 and 1.1. This median value, denoted as $(\Delta PAN/\Delta NO_y)_{aged}$, represents the $\Delta PAN/\Delta NO_y$ in aged smoke where nearly all NO_x is converted to NO_z. We also calculate the MCE of the corresponding measurements. Figure S33 shows that the $(\Delta PAN/\Delta NO_y)_{aged}$ of 11 fire ladders has a negative correlation with MCE. The trend is likely caused by that higher MCE is associated with lower $[CH_3CHO]/[NO_2]$ (Figure S38), which favors NO_x loss to HNO_3 rather than PAN and hence decreases $\Delta PAN/\Delta NO_y$.

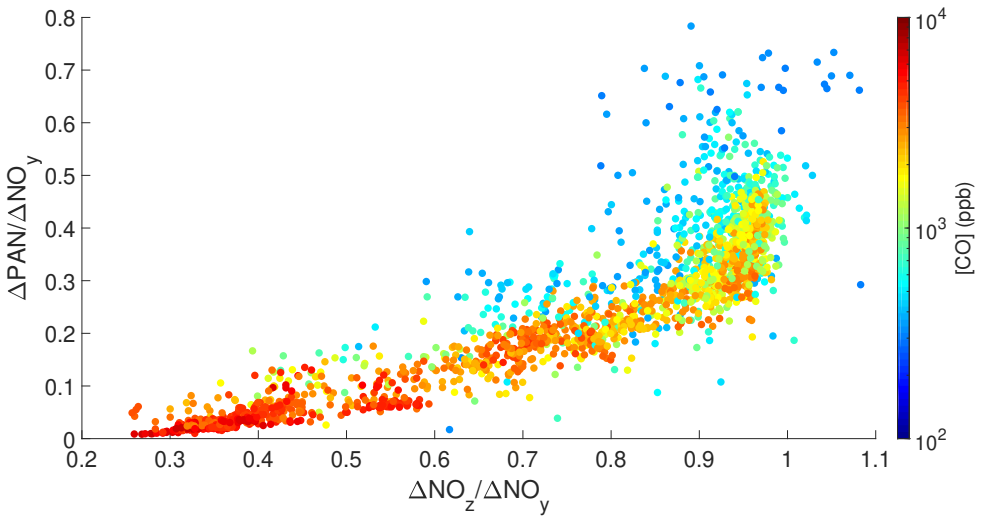

Figure S32: The evolution of $\Delta PAN/\Delta NO_y$ as a function of $\Delta NO_z/\Delta NO_y$ for the second fire ladder on 8/3/2019 flight.

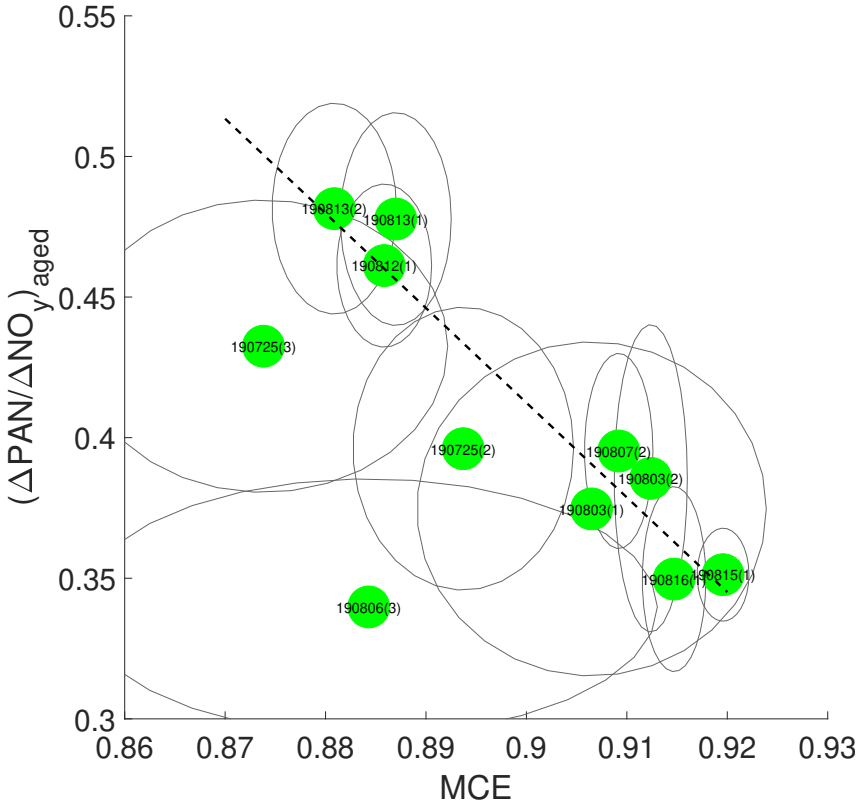

Figure S33: The $(\Delta PAN/\Delta NO_y)_{aged}$ as a function of MCE. The $(\Delta PAN/\Delta NO_y)_{aged}$ is represented by the median $\Delta PAN/\Delta NO_y$ of observations of which the $\Delta NO_z/\Delta NO_z$ is between 0.9 and 1.1. MCE is represented by the mean of the corresponding measurements. Only fire ladders that have more than 100 data points of which $\Delta NO_z/\Delta NO_y$ are within 0.9 and 1.1 are shown here. The dashed line represents York fit.

9 Uncertainty analysis

The uncertainty of measured $\Delta O_x/\Delta CO$ is calculated by propagating the uncertainties in O_3 (time dependent, and $\sim$3% on average), NO (8%), NO_2 (4%), HNO_3 (25%), PAN (20%), PBN (20%), APAN (20%), PPN (30%), AMS nitrate (34%), and CO (7%). The propagated uncertainty in measured $\Delta O_x/\Delta CO$ depends on transect and it ranges from 18% to 33%, with a mean value of 26%. The propagated uncertainty is displayed as the x-axis error bar in Figure 7.

The total uncertainties of the predicted O_x production stem from the uncertainties in the VOCs measurements, estimation of f_{RO_2+NO}, and OH exposure. The uncertainties of VOCs measurements are from the documented uncertainties of each instrument, which are not listed here. The uncertainty of f_{RO_2+NO} is estimated to be 20%, by considering (1) the difference in f_{RO_2+NO} values derived from ethene and propene systems and (2) the dependence of $k_{RO_2+HO_2}$ on the number of heavy atoms in RO_2 (as discussed in Section S8). The uncertainty of OH exposure is estimated to be 30% as discussed in Section S3. These uncertainties are propagated to calculate the total uncertainty of predicted O_x production. The propagated uncertainty in predicted $\Delta O_x/\Delta CO$ depends on transect and it ranges from 37% to 64%, with a mean value of 48%. The propagated uncertainty is displayed as the y-axis error bar in Figure 7.

10 Parameterize the production of O_3+NO_2

We parameterize the production of O_3+NO_2 using Multivariate Adaptive Regression Splines (MARS). This algorithm is an extension of multivariate linear regression and accounts for the non-linear relationship between predictors and response variables, which is observed in laboratory-simulated wildfires (*23*). We employed the Adaptive Regression Splines toolbox for Matlab written by ARESLab (http://www.cs.rtu.lv/jekabsons/regression.html). The basis functions are forced to be linear. Non-linear basis functions (continuous derivative truncated

cubics) are available in the toolbox, but disabled to avoid overfitting. No interaction between variables is allowed. The Generalized Cross-Validation penalty per knot is chosen automatically by the algorithm. We start with MCE and ΔOH exposure as independent variables, because they exhibit significant correlation with O_3+NO_2 production (Figure 8). Further, we stepwisely include VOCR, NO_x, NO_x/VOCR ratio, and f_{RO_2+NO} as predictors, but do not observe significant improvement in model performance by adding these predictors. Thus, only MCE and OH exposure are included in the final statistical model. The statistics of estimated coefficients are summarized in Table S6. The uncertainties are estimated from bootstrap analysis.

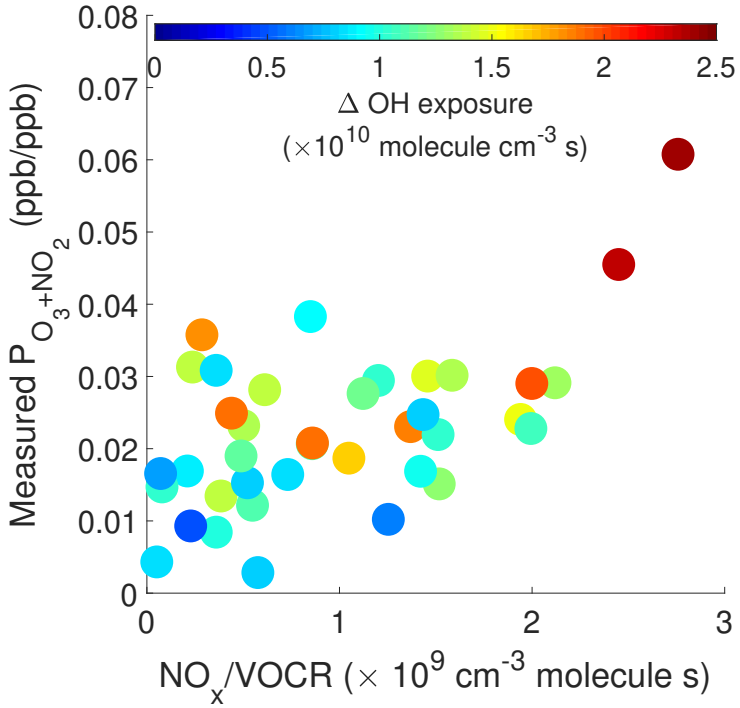

Figure S34: The measured production of O_3+NO_2 vs. the average NO_x/VOCR of each transect.

We compile the literature values of $\Delta O_3/\Delta CO$ in Figure S35. After a few hours of aging, $\Delta O_3/\Delta CO$ is much higher than $\Delta NO_2/\Delta CO$, so that the $\Delta O_3/\Delta CO$ compiled in the figure is comparable to the $\Delta(O_3 + NO_2)/\Delta CO$ reported in the near field of wildfire plumes. The $\Delta O_3/\Delta CO$ in aged plumes is highly uncertain because of uncertainties in estimating the background

Parameter	Estimate	Uncertainty	MSE[a]	GCV[b]	R2GCV[c]
intercept	0.0036	0.0028	-	-	-
max(0,MCE-0.916)	0.46	0.16	7×10^{-5}	8×10^{-5}	0.41
OH exposure	0.014	0.0019	1×10^{-4}	1.1×10^{-4}	0.14

[a] Mean Squared Error.
[b] Generalized Cross-Validation of the model in the training data set.
[c] R2 estimated by GCV in training data for the best candidate model of each size.

Table S6: Parameterization of the O_3+NO_2 production based on the statistical MARS model. Number of observation: 39. Mean squared error: 5.53×10^{-5}. $r^2 = 0.56$.

concentration of O_3 and CO. For example, studies G, I, and J used the measurements at the same PICO-NARE station in the Azores to study the influence of North American boreal fires, but obtained $\Delta O_3/\Delta CO$ values different by a factor of 4 by utilizing different methods to estimate the background concentration of O_3 and CO. Val Martin et al. (*27*) (Index J in Figure S35) determined the background concentrations (100 ppb for CO and 46 ppb for O_3) by "the boreal region outflow reached the station prior to the occurrence of the large fires". In contrast, Honrath et al. (*77*) (Index G in Figure S35) determined the background concentrations (61 ppb for CO and 25 ppb for O_3) based on periods associated with low frequency of flow over northeastern U.S. (i.e., "low-CO mode" in that study). The background concentrations in Honrath et al. (*77*) are lower than those in Val Martin et al. (*27*), leading to higher $\Delta O_3/\Delta CO$ in Honrath et al. (*77*). The complex history of air parcels (i.e., mixing with other sources) is another factor causing the variability in $\Delta O_3/\Delta CO$ in aged smoke. During the long-range transport of wildfire smokes, the plume could be affected by mixing with upper troposphere air with high O_3 and low CO, which leads to a biased high $\Delta O_3/\Delta CO$ at the reception site.

The amount of ozone produced from wildfire emissions can have substantial impacts on air quality. We estimate the impacts of wildfire emissions on surface O_3 concentration in the western U.S. during the fire season, by using the aircraft measured $\Delta(O_3 + NO_2)/\Delta CO$ and the estimated CO flux from wildfires. A study by Jaffe and Wigder (*5*) estimated that an

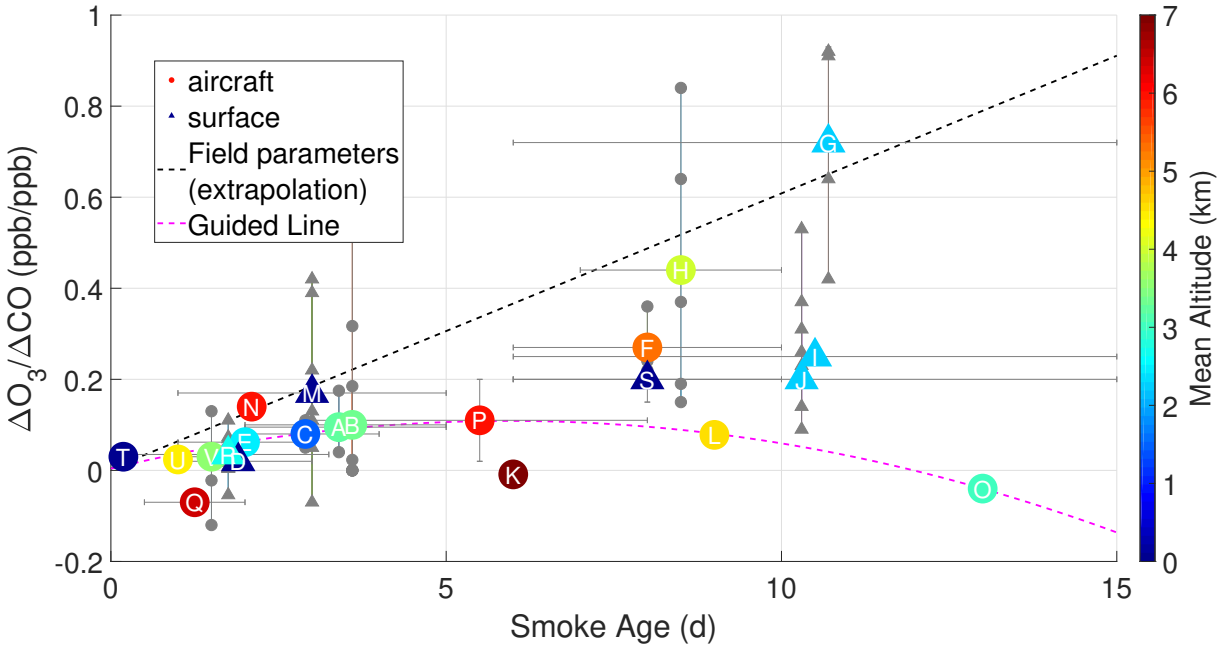

Figure S35: Literature review of $\Delta O_3/\Delta CO$ observed in boreal and temperate forest fires. The grey triangles and colorful circles represent the $\Delta O_3/\Delta CO$ of individual fire events and mean values of each study. The error bars represent the minimum and maximum values of each study. The dashed black line is the extrapolation of field-derived parameterization, which represents the O_3 formation if the NO_x is sustained at the near-field level. A constant daytime OH concentration of 10^6 molecules cm^{-3} is assumed. The coefficient b is divided by 2 to account for that the OH oxidation only occurs in daytime. The dashed pink line represents an upper bound of 13 out of 16 aircraft studies, excluding studies Q, F, H. This line is provided as a visual aid to show the trend of majority of aircraft studies. The dashed pink line follows the equation $\Delta O_3/\Delta CO = k0 + k1 \times age + k2 \times age^2$, where k0 = 4e-3, k1 = 3.5e-2, k2 = -3e-3, and age unit is day. References: A, Wofsy et al. (1992) (*78*); B, Mauzerall et al. (1996) (*79*); C, Wotawa et al. (2000) (*80*); D and E, DeBell et al. (2004) (*81*); F, Bertschi et al. (2004) (*82*); G, Honrath et al. (2004) (*77*); H, Bertschi et al. (2005) (*83*); I, Pfister et al. (2006) (*84*); J, Val Martin et al. (2006) (*27*); K and L, Real et al. (2007) (*85*); M, Tanimoto et al. (2008) (*86*); N and O, Paris et al. (2009) (*87*); P, Singh et al. (2010) (*88*); Q, Alvarado et al. (2010) (*20*); R, Baylon et al. (2017) (*89*); S, Teakles et al.(2017) (*90*); T, this study, fresh plume (physical age < 12 h); U, this study, aged plume (physical age > 24 h); V, SEAC4RS campaign data analyzed in this study. Studies G, I, J used the measurements from the same site. The smoke ages in these studies are likely similar, but are displayed with offset for clarity.

O_3 production rate of 0.027 Tg $month^{-1}$ is required to sustain a 1 ppb enhancement in O_3 concentration in the boundary layer (i.e., 1 km) of the western U.S. (i.e., 1500 km $\times$ 1500 km),

assuming an O_3 lifetime of 5 days. The $\Delta(O_3 + NO_2)/\Delta CO$ predicted by the field-derived parameterization (Eqn. 5) is 0.045, assuming a MCE value of 0.92 and an OH exposure value of 2.5×10^{10} molecules cm^{-3} s (i.e., maximum value used to constrain the parameterization, which is equivalent to roughly 7 h transport time). Combining this $\Delta(O_3 + NO_2)/\Delta CO$ and the estimated CO flux from wildfires averaged from 2011 to 2015 in the western U.S. (5240±2240 Gg yr^{-1} (*30*)), 0.4 Tg yr^{-1} O_3 is produced from wildfire emissions. Given the typical wildfire season in the western U.S. is June - October (*91*), evenly distributing the annual O_3 production over 5-months in the wildfire season leads a monthly production of 0.08 Tg. This amount is sufficient to sustain a 3 ppb enhancement in boundary layer O_3 concentration over the western U.S. during the fire season. The enhancement could double if the $\Delta(O_3 + NO_2)/\Delta CO$ reaches the maximum value of 0.1 when the smoke plume is 3-5 days aged. The enhancement could also be larger if the smoke plume mixes into the NO_x-rich urban atmospheres. One underlying assumption in above analysis is that the majority of wildfires inject smoke in the boundary layer, which is supported by a comprehensive analysis of satellite-retrieved wildfire smoke injection heights (*92*). The episodic nature of wildfires can result in more severe impacts on the occurrence of ozone exceedances.

11 Fuel types and emission factors in FIREX field and lab studies

Table S7 lists the fuel types of the research flights which provide the transects in the O_3 + NO_2 production parameterization. The fuel types are summarized based on: the burned area defined by the Fuel2Fire team using daily satellite fire-detection data, calibrated to the final Geospatial Multi-Agency Coordination perimeters; and the Fuel Characteristic Classification System (FCCS), which classifies wildland fuel characteristics at 30 m resolution. As shown in Table S7, a variety of fuel types were studied in the analysis. The fuel types, which are studied

in the 2016 FIREX FireLab study and relevant to the field measurements in this study, include bear grass, ceanothus, douglas fir, Engelmann spruce, juniper, lodgepole pine, ponderosa pine, sagebrush, subalpine fir, and manzanita. Different components of these fuel types were burned separately or in combinations in the lab study. More details can be found in Selimovic et al. (*36*).

Date	Fire Name	No.[b]	FCCS Fuel types (%Area)[a]
7/24	Sheep	1	Sagebrush shrubland - post prescribed burn (69%) Modified or Managed Xeric Grass 2 (29%)
7/25	Shady	3	Modified or Managed Xeric Grass 1 (34%) Modified or Managed Xeric Understory 2 (21%) Modified or Managed Xeric Grass Shrub 2 (18%) Modified or Managed Xeric Understory 1 (11%)
8/2	Ridgetop	4	Bluebunch wheatgrass-bluegrass grassland (66%)
8/3	Williams Flats	14	Douglas-fir-Pacific ponderosa pine/oceanspray forest (29%) Idaho fescue-bluebunch wheatgrass grassland (20%) Sagebrush shrubland - post prescribed burn (13%) Wheatgrass-cheatgrass grassland - exotic species (10%)
8/6	Horsefly	4	Subalpine fir-lodgepole pine-Engelmann spruce forest (43%) Douglas-fir-Pacific ponderosa pine/oceanspray forest (28%) Mature lodgepole pine forest (14%)
8/7	Williams Flats	6	Douglas-fir-Pacific ponderosa pine/oceanspray forest (55%) Idaho fescue-bluebunch wheatgrass grassland (12%)
8/12	Castle	1	Ponderosa pine-two-needle pinyon-Utah juniper forest (44%) Douglas-fir-white fir-ponderosa pine forest (12%) Madrean pine-oak forest (11%)
8/13	Castle	2	Ponderosa pine-two-needle pinyon-Utah juniper forest (41%) Douglas-fir-white fir-ponderosa pine forest (14%) Madrean pine-oak forest (12%) Ponderosa pine-white fir/quaking aspen forest (11%)
8/15	Sheridan	3	Pinyon-Utah juniper forest (80%) Turbinella oak-alderleaf mountain mahogany shrubland (17%)
8/16	Sheridan	1	Pinyon-Utah juniper forest (67%) Turbinella oak-alderleaf mountain mahogany shrubland (28%)

[a] %Area represents the fraction of total burned area. Fuel types that account for >10% of burned area are listed in the table.
[b] Number of Transects.

Table S7: FIREX-AQ fuel types of flights included in the parameterization of O_3+NO_2 formation.

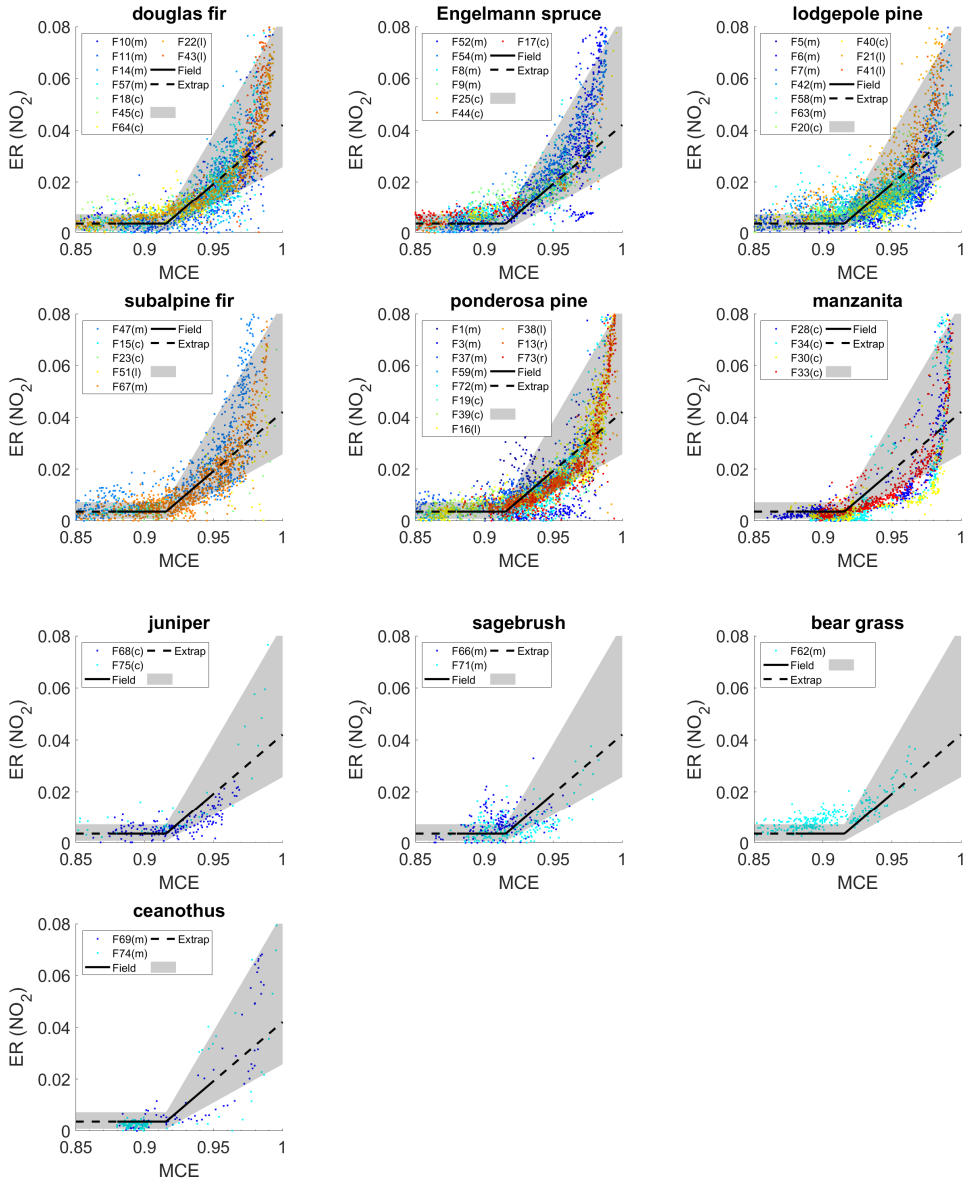

Figure S36: The fuel-specific NO_2 emission ratio relative to CO as a function of MCE. Each panel represents one fuel type characterized in the 2016 FIREX FireLab. The black line represents the field-derived initial emission of O_3+NO_2 (i.e., a + b$\times$max(0,MCE-c)). The number indicates fire index in lab study. The letter after the number indicates the fuel component: "m" means mixture, "l" means litter, "c" means canopy, "r" means rotten log.

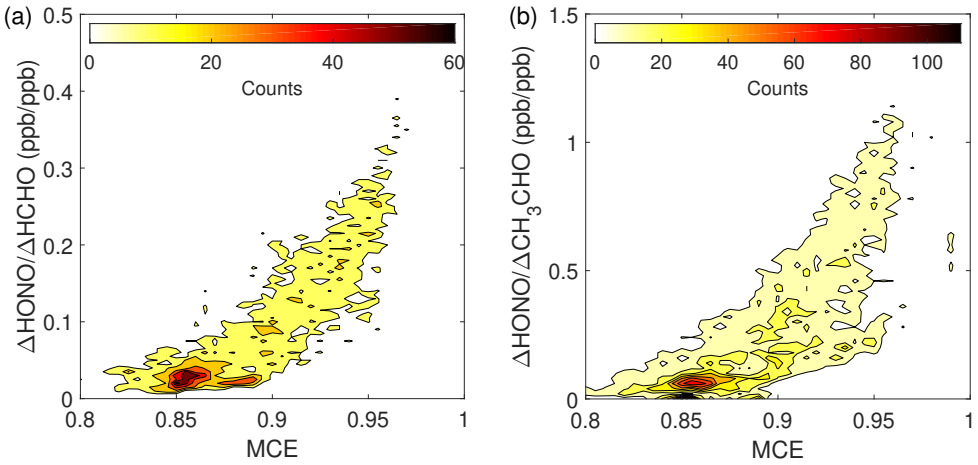

Figure S37: The emission ratio of (a) HONO/HCHO and (b) HONO/CH_3CHO as a function of MCE from the 2016 FIREX FireLab study. All FIREX-AQ relevant fuel types are compiled.

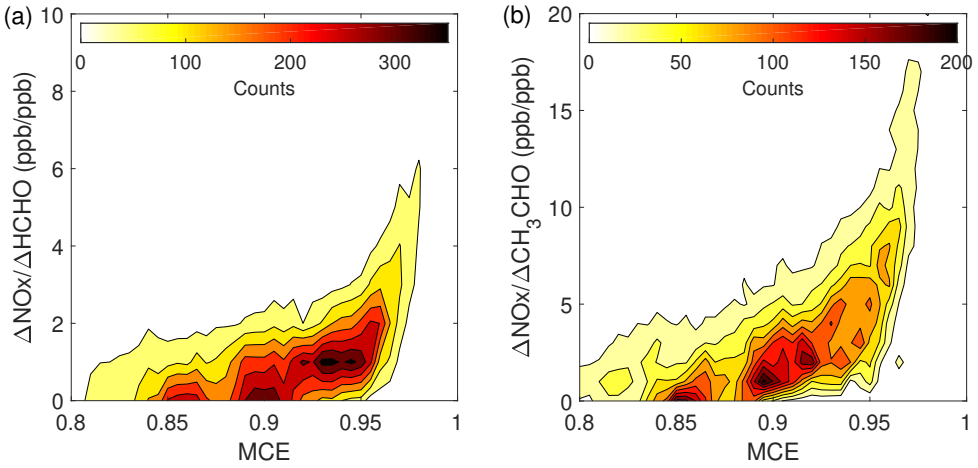

Figure S38: The emission ratio of (a) NO_x/HCHO and (b) NO_x/CH_3CHO as a function of MCE from the 2016 FIREX FireLab study. All FIREX-AQ relevant fuel types are compiled.

REFERENCES AND NOTES

1. S. K. Akagi, R. J. Yokelson, C. Wiedinmyer, M. J. Alvarado, J. S. Reid, T. Karl, J. D. Crounse, P. O. Wennberg, Emission factors for open and domestic biomass burning for use in atmospheric models.*Atmos. Chem. Phys.* **11**, 4039–4072 (2011)

2. M. O. Andreae, Emission of trace gases and aerosols from biomass burning–An updated assessment. *Atmos. Chem. Phys.* **19**, 8523–8546 (2019).

3. Y. Li, L. J. Mickley, P. Liu, J. O. Kaplan, Trends and spatial shifts in lightning fires and smoke concentrations in response to 21st century climate over the national forests and parks of the western United States. *Atmos. Chem. Phys.* **20**, 8827–8838 (2020).

4. D. A. Jaffe, S. M. O'Neill, N. K. Larkin, A. L. Holder, D. L. Peterson, J. E. Halofsky, A. G. Rappold, Wildfire and prescribed burning impacts on air quality in the United States. *J. Air Waste Manage. Assoc.* **70**, 583–615 (2020).

5. D. A. Jaffe, N. L. Wigder, Ozone production from wildfires: A critical review. *Atmos. Environ.* **51**, 1–10 (2012).

6. S. K. Akagi, J. S. Craven, J. W. Taylor, G. R. McMeeking, R. J. Yokelson, I. R. Burling, S. P. Urbanski, C. E. Wold, J. H. Seinfeld, H. Coe, M. J. Alvarado, D. R. Weise, Evolution of trace gases and particles emitted by a chaparral fire in California. *Atmos. Chem. Phys.* **12**, 1397–1421 (2012).

7. M. J. Alvarado, R. G. Prinn, Formation of ozone and growth of aerosols in young smoke plumes from biomass burning: 1. Lagrangian parcel studies. *J. Geophys. Res. Atmos.* **114** (2009).

8. M. J. Alvarado, C. Wang, R. G. Prinn, Formation of ozone and growth of aerosols in young smoke plumes from biomass burning: 2. Three-dimensional Eulerian studies. *J. Geophys. Res. Atmos.* **114** (2009).

9. M. Müller, B. E. Anderson, A. J. Beyersdorf, J. H. Crawford, G. S. Diskin, P. Eichler, A. Fried, F. N. Keutsch, T. Mikoviny, K. L. Thornhill, J. G. Walega, A. J. Weinheimer, M. Yang, R. J. Yokelson, A. Wisthaler, In situ measurements and modeling of reactive trace gases in a small biomass burning plume. *Atmos. Chem. Phys.* **16**, 3813–3824 (2016).

10. M. M. Coggon, C. Y. Lim, A. R. Koss, K. Sekimoto, B. Yuan, J. B. Gilman, D. H. Hagan, V. Selimovic, K. J. Zarzana, S. S. Brown, J. M. Roberts, M. Müller, R. Yokelson, A. Wisthaler, J. E. Krechmer, J. L. Jimenez, C. Cappa, J. H. Kroll, J. de Gouw, C. Warneke, OH chemistry of non-methane organic gases (NMOGs) emitted from laboratory and ambient biomass burning smoke: Evaluating the influence of furans and oxygenated aromatics on ozone and secondary NMOG formation*Atmos. Chem. Phys.* **19**, 14875–14899 (2019).

11. M. A. Robinson, Z. C. J. Decker, K. C. Barsanti, M. M. Coggon, F. M. Flocke, A. Franchin, C. D. Fredrickson, J. B. Gilman, G. I. Gkatzelis, C. D. Holmes, A. Lamplugh, A. Lavi, A. M. Middlebrook, D. M. Montzka, B. B. Palm, J. Peischl, B. Pierce, R. H. Schwantes, K. Sekimoto, V. Selimovic, G. S. Tyndall, J. A. Thornton, P. van Rooy, C. Warneke, A. J. Weinheimer, S. S. Brown,, Variability and time of day dependence of ozone photochemistry in western wildfire plumes. *Environ. Sci. Technol.* **55**, 10280–10290 (2021).

12. P. J. Young, V. Naik, A. M. Fiore, A. Gaudel, J. Guo, M. Y. Lin, J. L. Neu, D. D. Parrish, H. E. Rieder, J. L. Schnell, S. Tilmes, O. Wild, L. Zhang, J. Ziemke, J. Brandt, A. Delcloo, R. M. Doherty, C. Geels, M. I. Hegglin, L. Hu, U. Im, R. Kumar, A. Luhar, L. Murray, D. Plummer, J. Rodriguez, A. Saiz-Lopez, M. G. Schultz, M. T. Woodhouse, G. Zeng, Tropospheric Ozone Assessment Report: Assessment of global-scale model performance for global and regional ozone distributions, variability, and trends. *Elementa* **6**, 10 (2018).

13. Y. Wang, J. A. Logan, D. J. Jacob, Global simulation of tropospheric O3-NOx-hydrocarbon chemistry: 2. Model evaluation and global ozone budget. *J. Geophys. Res. Atmos.* **103**, 10727–10755 (1998).

14. Q. Peng, B. B. Palm, K. E. Melander, B. H. Lee, S. R. Hall, K. Ullmann, T. Campos, A. J. Weinheimer, E. C. Apel, R. S. Hornbrook, A. J. Hills, D. D. Montzka, F. Flocke, L. Hu, W. Permar, C. Wielgasz, J. Lindaas, I. B. Pollack, E. V. Fischer, T. H. Bertram, J. A. Thornton,

HONO emissions from western U.S. wildfires provide dominant radical source in fresh wildfire smoke*Environ. Sci. Technol.* **54**, 5954–5963 (2020).

15. A. R. Koss, K. Sekimoto, J. B. Gilman, V. Selimovic, M. M. Coggon, K. J. Zarzana, B. Yuan, B. M. Lerner, S. S. Brown, J. L. Jimenez, J. Krechmer, J. M. Roberts, C. Warneke, R. J. Yokelson, J. de Gouw, Non-methane organic gas emissions from biomass burning: Identification, quantification, and emission factors from PTR-ToF during the FIREX 2016 laboratory experiment. *Atmos. Chem. Phys.* **18**, 3299–3319 (2018).

16. A. Akherati, Y. He, M. M. Coggon, A. R. Koss, A. L. Hodshire, K. Sekimoto, C. Warneke, J. de Gouw, L. Yee, J. H. Seinfeld, T. B. Onasch, S. C. Herndon, W. B. Knighton, C. D. Cappa, M. J. Kleeman, C. Y. Lim, J. H. Kroll, J. R. Pierce, S. H. Jathar, Oxygenated aromatic compounds are important precursors of secondary organic aerosol in biomass-burning emissions. *Environ. Sci. Technol.* **54**, 8568–8579 (2020).

17. B. B. Palm, Q. Peng, C. D. Fredrickson, B. H. Lee, L. A. Garofalo, M. A. Pothier, S. M. Kreidenweis, D. K. Farmer, R. P. Pokhrel, Y. Shen, S. M. Murphy, W. Permar, L. Hu, T. L. Campos, S. R. Hall, K. Ullmann, X. Zhang, F. Flocke, E. V. Fischer, J. A. Thornton Quantification of organic aerosol and brown carbon evolution in fresh wildfire plumes. *Proc. Natl. Acad. Sci.* **117**, 29469–29477 (2020).

18. C. Ichoku, L. Giglio, M. J. Wooster, L. A. Remer, Global characterization of biomass-burning patterns using satellite measurements of fire radiative energy. *Remote Sens. Environ.* **112**, 2950–2962 (2008).

19. J. F. Juncosa Calahorrano, J. Lindaas, K. O'Dell, B. B. Palm, Q. Peng, F. Flocke, I. B. Pollack, L. A. Garofalo, D. K. Farmer, J. R. Pierce, J. L. Collett Jr., A. Weinheimer, T. Campos, R. S. Hornbrook, S. R. Hall, K. Ullmann, M. A. Pothier, E. C. Apel, W. Permar, L. Hu, A. J. Hills, D. Montzka, G. Tyndall, J. A. Thornton, E. V. Fischer, Daytime oxidized reactive nitrogen partitioning in western U.S. wildfire smoke plumes. *J. Geophys. Res. Atmos.* **126**, e2020JD033484 (2021).

20. M. J. Alvarado, J. A. Logan, J. Mao, E. Apel, D. Riemer, D. Blake, R. C. Cohen, K. E. Min, A. E. Perring, E. C. Browne, P. J. Wooldridge, G. S. Diskin, G. W. Sachse, H. Fuelberg, W. R. Sessions, D. L. Harrigan, G. Huey, J. Liao, A. Case-Hanks, J. L. Jimenez, M. J. Cubison, S. A. Vay, A. J. Weinheimer, D. J. Knapp, D. D. Montzka, F. M. Flocke, I. B. Pollack, P. O. Wennberg, A. Kurten, J. Crounse, J. M. S. Clair, A. Wisthaler, T. Mikoviny, R. M. Yantosca, C. C. Carouge, P. le Sager, Nitrogen oxides and PAN in plumes from boreal fires during ARCTAS-B and their impact on ozone: An integrated analysis of aircraft and satellite observations. *Atmos. Chem. Phys.* **10**, 9739–9760 (2010).

21. I. B. Konovalov, M. Beekmann, B. D'Anna, C. George, Significant light induced ozone loss on biomass burning aerosol: Evidence from chemistry-transport modeling based on new laboratory studies. *Geophys. Res. Lett.* **39**, L17807 (2012).

22. R. J. Yokelson, T. J. Christian, T. G. Karl, A. Guenther, The tropical forest and fire emissions experiment: Laboratory fire measurements and synthesis of campaign data. *Atmos. Chem. Phys.* **8**, 3509–3527 (2008).

23. J. M. Roberts, C. E. Stockwell, R. J. Yokelson, J. de Gouw, Y. Liu, V. Selimovic, A. R. Koss, K. Sekimoto, M. M. Coggon, B. Yuan, K. J. Zarzana, S. S. Brown, C. Santin, S. H. Doerr, C. Warneke, The nitrogen budget of laboratory-simulated western US wildfires during the FIREX 2016 FireLab study. *Atmos. Chem. Phys.* **20**, 8807–8826 (2020).

24. J. H. Friedman, Multivariate adaptive regression splines. *Ann. Stat.* **19**, 1–67 (1991).

25. N. L. Ng, J. H. Kroll, A. W. H. Chan, P. S. Chhabra, R. C. Flagan, J. H. Seinfeld, Secondary organic aerosol formation from *m*-xylene, toluene, and benzene. *Atmos. Chem. Phys.* **7**, 3909–3922. (2007)

26. L. D. Yee, K. E. Kautzman, C. L. Loza, K. A. Schilling, M. M. Coggon, P. S. Chhabra, M. N. Chan, A. W. H. Chan, S. P. Hersey, J. D. Crounse, P. O. Wennberg, R. C. Flagan, J. H. Seinfeld, Secondary organic aerosol formation from biomass burning intermediates: Phenol and methoxyphenols. *Atmos. Chem. Phys.* **13**, 8019–8043 (2013).

27. M. Val Martín, R. E. Honrath, R. C. Owen, G. Pfister, P. Fialho, F. Barata, Significant enhancements of nitrogen oxides, black carbon, and ozone in the North Atlantic lower free troposphere resulting from North American boreal wildfires. *J. Geophys. Res. Atmos.* **111**, D23S60 (2006).

28. S. J. Brey, E. V. Fischer, Smoke in the city: How often and where does smoke impact summertime ozone in the United States?. *Environ. Sci. Technol.* **50**, 1288–1294 (2016).

29. E. C. Apel, R. S. Hornbrook, A. J. Hills, N. J. Blake, M. C. Barth, A. Weinheimer, C. Cantrell, S. A. Rutledge, B. Basarab, J. Crawford, G. Diskin, C. R. Homeyer, T. Campos, F. Flocke, A. Fried, D. R. Blake, W. Brune, I. Pollack, J. Peischl, T. Ryerson, P. O. Wennberg, J. D. Crounse, A. Wisthaler, T. Mikoviny, G. Huey, B. Heikes, D. O'Sullivan, D. D. Riemer, Upper tropospheric ozone production from lightning NOx-impacted convection: Smoke ingestion case study from the DC3 campaign. *J. Geophys. Res. Atmos.* **120**, 2505–2523 (2015)

30. X. Liu, L. G. Huey, R. J. Yokelson, V. Selimovic, I. J. Simpson, M. Müller, J. L. Jimenez, P. Campuzano-Jost, A. J. Beyersdorf, D. R. Blake, Z. Butterfield, Y. Choi, J. D. Crounse, D. A. Day, G. S. Diskin, M. K. Dubey, E. Fortner, T. F. Hanisco, W. Hu, L. E. King, L. Kleinman, S. Meinardi, T. Mikoviny, T. B. Onasch, B. B. Palm, J. Peischl, I. B. Pollack, T. B. Ryerson, G. W. Sachse, A. J. Sedlacek, J. E. Shilling, S. Springston, J. M. St. Clair, D. J. Tanner, A. P. Teng, P. O. Wennberg, A. Wisthaler, G. M. Wolfe, Airborne measurements of western U.S. wildfire emissions: Comparison with prescribed burning and air quality implications. *J. Geophys. Res. Atmos.* **122**, 6108–6129, (2017).

31. E. B. Wiggins, A. J. Soja, E. Gargulinski, H. S. Halliday, R. B. Pierce, C. C. Schmidt, J. B. Nowak, J. P. Di Gangi, G. S. Diskin, J. M. Katich, A. E. Perring, J. P. Schwarz, B. E. Anderson, G. Chen, E. C. Crosbie, C. Jordan, C. E. Robinson, K. J. Sanchez, T. J. Shingler, M. Shook, K. L. Thornhill, E. L. Winstead, L. D. Ziemba, R. H. Moore, High temporal resolution satellite observations of fire radiative power reveal link between fire behavior and aerosol and gas emissions. *Geophys. Res. Lett.* **47**, e2020GL090707 (2020).

32. L. A. Garofalo, M. A. Pothier, E. J. T. Levin, T. Campos, S. M. Kreidenweis, D. K. Farmer, Emission and evolution of submicron organic aerosol in smoke from wildfires in the western United States. *ACS Earth Space Chem.* **3**, 1237–1247 (2019).

33. T. B. Ryerson, L. G. Huey, K. Knapp, J. A. Neuman, D. D. Parrish, D. T. Sueper, F. C. Fehsenfeld, Design and initial characterization of an inlet for gas-phase NOymeasurements from aircraft. *J. Geophys. Res. Atmos.* **104**, 5483–5492 (1999).

34. M. Luria, R. J. Valente, R. L. Tanner, N. V. Gillani, R. E. Imhoff, S. F. Mueller, K. J. Olszyna, J. F. Meagher, The evolution of photochemical smog in a power plant plume. *Atmos. Environ.* **33**, 3023–3036 (1999).

35. T. B. Ryerson, M. Trainer, J. S. Holloway, D. D. Parrish, L. G. Huey, D. T. Sueper, G. J. Frost, S. G. Donnelly, S. Schauffler, E. L. Atlas, W. C. Kuster, P. D. Goldan, G. Hübler, J. F. Meagher, F. C. Fehsenfeld, Observations of ozone formation in power plant plumes and implications for ozone control strategies. *Science* **292**, 719–723 (2001)

36. V. Selimovic, R. J. Yokelson, C. Warneke, J. M. Roberts, J. de Gouw, J. Reardon, D. W. T. Griffith, Aerosol optical properties and trace gas emissions by PAX and OP-FTIR for laboratory-simulated western US wildfires during FIREX. *Atmos. Chem. Phys.* **18**, 2929–2948 (2018).

37. A. F. Stein, R. R. Draxler, G. D. Rolph, B. J. B. Stunder, M. D. Cohen, F. Ngan, NOAA's HYSPLIT atmospheric transport and dispersion modeling system. *Bull. Am. Meteorol. Soc.* **96**, 2059–2077 (2015)

38. A. W. Rollins, P. S. Rickly, R.S. Gao, T. B. Ryerson, S. S. Brown, J. Peischl, I. Bourgeois, Single-photon laser-induced fluorescence detection of nitric oxide at sub-parts-per-trillion mixing ratios. *Atmos. Meas. Tech.* **13**, 2425–2439 (2020).

39. J. M. St. Clair, A. K. Swanson, S. A. Bailey, T. F. Hanisco, CAFE: A new, improved nonresonant laser-induced fluorescence instrument for airborne in situ measurement of formaldehyde. *Atmos. Meas. Tech.* **12**, 4581–4590 (2019).

40. K. E. Min, R. A. Washenfelder, W. P. Dubé, A. O. Langford, P. M. Edwards, K. J. Zarzana, J. Stutz, K. Lu, F. Rohrer, Y. Zhang, S. S. Brown, A broadband cavity enhanced absorption spectrometer for aircraft measurements of glyoxal, methylglyoxal, nitrous acid, nitrogen dioxide, and water vapor. *Atmos. Meas. Tech.* **9**, 423–440, (2016)

41. P. R. Veres, J. A. Neuman, T. H. Bertram, E. Assaf, G. M. Wolfe, C. J. Williamson, B. Weinzierl, S. Tilmes, C. R. Thompson, A. B. Thames, J. C. Schroder, A. Saiz-Lopez, A. W. Rollins, J. M. Roberts, D. Price, J. Peischl, B. A. Nault, K. H. Møller, D. O. Miller, S. Meinardi, Q. Li, J.F. Lamarque, A. Kupc, H. G. Kjaergaard, D. Kinnison, J. L. Jimenez, C. M. Jernigan, R. S. Hornbrook, A. Hills, M. Dollner, D. A. Day, C. A. Cuevas, P. Campuzano-Jost, J. Burkholder, T. P. Bui, W. H. Brune, S. S. Brown, C. A. Brock, I. Bourgeois, D. R. Blake, E. C. Apel, T. B. Ryerson, Global airborne sampling reveals a previously unobserved dimethyl sulfide oxidation mechanism in the marine atmosphere. *Proc. Natl. Acad. Sci. U.S.A.* **117**, 4505–4510 (2020).

42. M. Cazorla, G. M. Wolfe, S. A. Bailey, A. K. Swanson, H. L. Arkinson, T. F. Hanisco, A new airborne laser-induced fluorescence instrument for in situ detection of formaldehyde throughout the troposphere and lower stratosphere. *Atmos. Meas. Tech.* **8**, 541–552 (2015)

43. D. Richter, P. Weibring, J. G. Walega, A. Fried, S. M. Spuler, M. S. Taubman, Compact highly sensitive multi-species airborne mid-IR spectrometer. *Appl. Phys. B* **119**, 119–131 (2015)

44. J. Liao, G. M. Wolfe, R. A. Hannun, J. M. St. Clair, T. F. Hanisco, J. B. Gilman, A. Lamplugh, V. Selimovic, G. S. Diskin, J. B. Nowak, H. S. Halliday, J. P. DiGangi, S. R. Hall, K. Ullmann, C. D. Holmes, C. H. Fite, A. Agastra, T. B. Ryerson, J. Peischl, I. Bourgeois, C. Warneke, M. M. Coggon, G. I. Gkatzelis, K. Sekimoto, A. Fried, D. Richter, P. Weibring, E. C. Apel, R. S. Hornbrook, S. S. Brown, C. C. Womack, M. A. Robinson, R. A. Washenfelder, P. R. Veres, J. A. Neuman, Formaldehyde evolution in U.S. wildfire plumes during FIREX-AQ. *Atmos. Chem. Phys. Discuss.* **2021**, 1–38 (2021).

45. J. D. Crounse, K. A. McKinney, A. J. Kwan, P. O. Wennberg, Measurement of gas-phase hydroperoxides by chemical ionization mass spectrometry. *Anal. Chem.* **78**, 6726–6732 (2006).

46. L. G. Huey, Measurement of trace atmospheric species by chemical ionization mass spectrometry: Speciation of reactive nitrogen and future directions. *Mass Spectrom. Rev.* **26**, 166–184 (2007).

47. P. F. DeCarlo, J. R. Kimmel, A. Trimborn, M. J. Northway, J. T. Jayne, A. C. Aiken, M. Gonin, K. Fuhrer, T. Horvath, K. S. Docherty, D. R. Worsnop, J. L. Jimenez, Field-deployable, high-resolution, time-of-flight aerosol mass spectrometer. *Anal. Chem.* **78**, 8281–8289 (2006).

48. M. R. Canagaratna, J. T. Jayne, J. L. Jimenez, J. D. Allan, M. R. Alfarra, Q. Zhang, T. B. Onasch, F. Drewnick, H. Coe, A. Middlebrook, A. Delia, L. R. Williams, A. M. Trimborn, M. J. Northway, P. F. DeCarlo, C. E. Kolb, P. Davidovits, D. R. Worsnop, Chemical and microphysical characterization of ambient aerosols with the aerodyne aerosol mass spectrometer. *Mass Spectrom. Rev.* **26**, 185–222 (2007).

49. H. Guo, P. Campuzano-Jost, B. A. Nault, D. A. Day, J. C. Schroder, D. Kim, J. E. Dibb, M. Dollner, B. Weinzierl, J. L. Jimenez, The importance of size ranges in aerosol instrument intercomparisons: a case study for the Atmospheric Tomography Mission. *Atmos. Meas. Tech.* **14**, 3631–3655 (2021).

50. B. M. Lerner, J. B. Gilman, K. C. Aikin, E. L. Atlas, P. D. Goldan, M. Graus, R. Hendershot, G. A. Isaacman-VanWertz, A. Koss, W. C. Kuster, R. A. Lueb, R. J. McLaughlin, J. Peischl, D. Sueper, T. B. Ryerson, T. W. Tokarek, C. Warneke, B. Yuan, J. A. de Gouw, An improved, automated whole air sampler and gas chromatography mass spectrometry analysis system for volatile organic compounds in the atmosphere. *Atmos. Meas. Tech.* **10**, 291–313 (2017)

51. J. de Gouw, C. Warneke, Measurements of volatile organic compounds in the earth's atmosphere using proton-transfer-reaction mass spectrometry. *Mass Spectrom. Rev.* **26**, 223–257 (2007)

52. M. Müller, T. Mikoviny, S. Feil, S. Haidacher, G. Hanel, E. Hartungen, A. Jordan, L. Märk, P. Mutschlechner, R. Schottkowsky, P. Sulzer, J. H. Crawford, A. Wisthaler, A compact PTR-ToF-MS instrument for airborne measurements of volatile organic compounds at high spatiotemporal resolution. *Atmos. Meas. Tech.* **7**, 3763–3772 (2014).

53. G. W. Sachse, G. F. Hill, L. O. Wade, M. G. Perry, Fast-response, high-precision carbon monoxide sensor using a tunable diode laser absorption technique. *J. Geophys. Res. Atmos.* **92**, 2071 (1987).

54. R. E. Shetter, M. Müller, Photolysis frequency measurements using actinic flux spectroradiometry during the PEM-Tropics mission: Instrumentation description and some results. *J. Geophys. Res. Atmos.* **104**, 5647–5661 (1999).

55. G. Diskin, J. Podolske, G. Sachse, T. Slate, *Open-path airborne tunable diode laser hygrometer*, vol. 4817 of *International Symposium on Optical Science and Technology* (SPIE, 2002).

56. D. D. Parrish, A. Stohl, C. Forster, E. L. Atlas, D. R. Blake, P. D. Goldan, W. C. Kuster, J. A. de Gouw, Effects of mixing on evolution of hydrocarbon ratios in the troposphere. *J. Geophys. Res. Atmos.* **112**, D10S34 (2007).

57. S. A. McKeen, S. C. Liu, Hydrocarbon ratios and photochemical history of air masses. *Geophys. Res. Lett.* **20**, 2363–2366 (1993).

58. J. A. de Gouw, C. A. Brock, E. L. Atlas, T. S. Bates, F. C. Fehsenfeld, P. D. Goldan, J. S. Holloway, W. C. Kuster, B. M. Lerner, B. M. Matthew, A. M. Middlebrook, T. B. Onasch, R. E. Peltier, P. K. Quinn, C. J. Senff, A. Stohl, A. P. Sullivan, M. Trainer, C. Warneke, R. J. Weber, E. J. Williams, Sources of particulate matter in the northeastern United States in

summer: 1. Direct emissions and secondary formation of organic matter in urban plumes. *J. Geophys. Res.* **113**, (2008).

59. Z. C. J. Decker, M. A. Robinson, K. C. Barsanti, I. Bourgeois, M. M. Coggon, J. P. DiGangi, G. S. Diskin, F. M. Flocke, A. Franchin, C. D. Fredrickson, G. I. Gkatzelis, S. R. Hall, H. Halliday, C. D. Holmes, L. G. Huey, Y. R. Lee, J. Lindaas, A. M. Middlebrook, D. D. Montzka, R. Moore, J. A. Neuman, J. B. Nowak, B. B. Palm, J. Peischl, F. Piel, P. S. Rickly, A. W. Rollins, T. B. Ryerson, R. H. Schwantes, K. Sekimoto, L. Thornhill, J. A. Thornton, G. S. Tyndall, K. Ullmann, P. Van Rooy, P. R. Veres, C. Warneke, R. A. Washenfelder, A. J. Weinheimer, E. Wiggins, E. Winstead, A. Wisthaler, C. Womack, S. S. Brown, Nighttime and daytime dark oxidation chemistry in wildfire plumes: an observation and model analysis of FIREX-AQ aircraft data. *Atmos. Chem. Phys.* **21**, 16293–16317 (2021).

60. L. Xu, K. H. Møller, J. D. Crounse, H. G. Kjaergaard, P. O. Wennberg, New insights into the radical chemistry and product distribution in the OH-initiated oxidation of benzene. *Environ. Sci. Technol.* **54**, 13467–13477 (2020).

61. A. L. Hodshire, A. Akherati, M. J. Alvarado, B. Brown-Steiner, S. H. Jathar, J. L. Jimenez, S. M. Kreidenweis, C. R. Lonsdale, T. B. Onasch, A. M. Ortega, J. R. Pierce, Aging effects on biomass burning aerosol mass and composition: A critical review of field and laboratory studies. *Environ. Sci. Technol.* **53**, 10007–10022 (2019).

62. H. B. Singh, C. Cai, A. Kaduwela, A. Weinheimer, A. Wisthaler, Interactions of fire emissions and urban pollution over California: Ozone formation and air quality simulations. *Atmos. Environ.* **56**, 45–51 (2012).

63. C. C. Womack, E. E. McDuffie, P. M. Edwards, R. Bares, J. A. Gouw, K. S. Docherty, W. P. Dubé, D. L. Fibiger, A. Franchin, J. B. Gilman, L. Goldberger, B. H. Lee, J. C. Lin, R. Long, A. M. Middlebrook, D. B. Millet, A. Moravek, J. G. Murphy, P. K. Quinn, T. P. Riedel, J. M. Roberts, J. A. Thornton, L. C. Valin, P. R. Veres, A. R. Whitehill, R. J. Wild, C. Warneke, B. Yuan, M. Baasandorj, S. S. Brown, An odd oxygen framework for wintertime ammonium nitrate aerosol pollution in urban areas: NOx and VOC control as mitigation strategies. *Geophys. Res. Lett.* **46**, 4971–4979 (2019).

64. P. S. J. Lakey, I. J. George, L. K. Whalley, M. T. Baeza-Romero, D. E. Heard, Measurements of the HO_2 uptake coefficients onto single component organic aerosols. *Environ. Sci. Technol.* **49**, 4878–4885 (2015).

65. R. J. Yokelson, M. O. Andreae, S. K. Akagi, Pitfalls with the use of enhancement ratios or normalized excess mixing ratios measured in plumes to characterize pollution sources and aging. *Atmos. Meas. Tech.* **6**, 2155–2158 (2013).

66. R. Atkinson, J. Arey, Atmospheric degradation of volatile organic compounds. *Chem. Rev.* **103**, 4605–4638 (2003).

67. X. Liu, Y. Zhang, L. G. Huey, R. J. Yokelson, Y. Wang, J. L. Jimenez, P. Campuzano-Jost, A. J. Beyersdorf, D. R. Blake, Y. Choi, J. M. St. Clair, J. D. Crounse, D. A. Day, G. S. Diskin, A. Fried, S. R. Hall, T. F. Hanisco, L. E. King, S. Meinardi, T. Mikoviny, B. B. Palm, J. Peischl, A. E. Perring, I. B. Pollack, T. B. Ryerson, G. Sachse, J. P. Schwarz, I. J. Simpson, D. J. Tanner, K. L. Thornhill, K. Ullmann, R. J. Weber, P. O. Wennberg, A. Wisthaler, G. M. Wolfe, L. D. Ziemba, Agricultural fires in the southeastern U.S. during SEAC4RS: Emissions of trace gases and particles and evolution of ozone, reactive nitrogen, and organic aerosol. *J. Geophys. Res. Atmos.* **121**, 7383–7414 (2016).

68. J. Trentmann, R. J. Yokelson, P. V. Hobbs, T. Winterrath, T. J. Christian, M. O. Andreae, S. A. Mason, An analysis of the chemical processes in the smoke plume from a savanna fire. *J. Geophys. Res. Atmos.* **110**, D12 (2005).

69. P. V. Hobbs, P. Sinha, R. J. Yokelson, T. J. Christian, D. R. Blake, S. Gao, T. W. Kirchstetter, T. Novakov, P. Pilewskie, Evolution of gases and particles from a savanna fire in South Africa. *J. Geophys. Res. Atmos.* **108**, (2003).

70. R. S. Rosen, E. C. Wood, P. J. Wooldridge, J. A. Thornton, D. A. Day, W. Kuster, E. J. Williams, B. T. Jobson, R. C. Cohen, Observations of total alkyl nitrates during Texas Air Quality Field Study 2000: Implications for O_3 and alkyl nitrate photochemistry. *J. Geophys. Res. Atmos.* **109**, D07303 (2004).

71. A. P. Teng, J. D. Crounse, L. Lee, J. M. St. Clair, R. C. Cohen, P. O. Wennberg, Hydroxy nitrate production in the OH-initiated oxidation of alkenes. *Atmos. Chem. Phys.* **15**, 4297–4316 (2015).

72. P. O. Wennberg, K. H. Bates, J. D. Crounse, L. G. Dodson, R. C. McVay, L. A. Mertens, T. B. Nguyen, E. Praske, R. H. Schwantes, M. D. Smarte, J. M. St Clair, A. P. Teng, X. Zhang, J. H. Seinfeld, Gas-phase reactions of isoprene and its major oxidation products. *Chem. Rev.* **118**, 3337–3390 (2018).

73. S. Nehr, B. Bohn, A. Wahner, Prompt HO2 formation following the reaction of OH with aromatic compounds under atmospheric conditions. *Chem. A Eur. J.* **116**, 6015–6026 (2012).

74. Y. Yuan, X. Zhao, S. Wang, L. Wang, Atmospheric oxidation of furan and methyl-substituted furans initiated by hydroxyl radicals. *Chem. A Eur. J.* **121**, 9306–9319 (2017).

75. X. Zhao, L. Wang, Atmospheric oxidation mechanism of furfural initiated by hydroxyl radicals. *Chem. A Eur. J.* **121**, 3247–3253 (2017).

76. R. Atkinson, S. M. Aschmann, W. P. L. Carter, A. M. Winer, J. N. Pitts, Alkyl nitrate formation from the nitrogen oxide (NOx)-air photooxidations of C2-C8 n-alkanes. *J. Phys. Chem.* **86**, 4563–4569 (1982).

77. R. E. Honrath, R. C. Owen, M. Val Martín, J. S. Reid, K. Lapina, P. Fialho, M. P. Dziobak, J. Kleissl, D. L. Westphal, Regional and hemispheric impacts of anthropogenic and biomass burning emissions on summertime CO and O_3 in the North Atlantic lower free troposphere. *J. Geophys. Res. Atmos.* **109**, D24310 (2004).

78. S. C. Wofsy, G. W. Sachse, G. L. Gregory, D. R. Blake, J. D. Bradshaw, S. T. Sandholm, H. B. Singh, J. A. Barrick, R. C. Harriss, R. W. Talbot, M. A. Shipham, E. V. Browell, D. J. Jacob, J. A. Logan, Atmospheric chemistry in the Arctic and subarctic: Influence of natural fires, industrial emissions, and stratospheric inputs. *J. Geophys. Res. Atmos.* **97**, 16731 (1992).

79. D. L. Mauzerall, D. J. Jacob, S.M. Fan, J. D. Bradshaw, G. L. Gregory, G. W. Sachse, D. R. Blake, Origin of tropospheric ozone at remote high northern latitudes in summer. *J. Geophys. Res. Atmos.* **101**, 4175–4188 (1996).

80. G. Wotawa, M. Trainer, The influence of Canadian forest fires on pollutant concentrations in the United States. *Science* **288**, 324–328 (2000).

81. L. J. DeBell, R. W. Talbot, J. E. Dibb, J. W. Munger, E. V. Fischer, S. E. Frolking, A major regional air pollution event in the northeastern United States caused by extensive forest fires in Quebec, Canada. *J. Geophys. Res. Atmos.* **109**, (2004).

82. I. T. Bertschi, D. A. Jaffe, Long-range transport of ozone, carbon monoxide, and aerosols to the NE Pacific troposphere during the summer of 2003: Observations of smoke plumes from Asian boreal fires. *J. Geophys. Res. Atmos.* **110**, D05303 (2005).

83. I. T. Bertschi, D. A. Jaffe, L. Jaeglé, H. U. Price, J. B. Dennison, PHOBEA/ITCT 2002 airborne observations of transpacific transport of ozone, CO, volatile organic compounds, and aerosols to the northeast Pacific: Impacts of Asian anthropogenic and Siberian boreal fire emissions. *J. Geophys. Res. Atmos.* **109**, D23S12 (2004),

84. G. G. Pfister, L. K. Emmons, P. G. Hess, R. Honrath, J.-F. Lamarque, M. Val Martin, R. C. Owen, M. A. Avery, E. V. Browell, J. S. Holloway, P. Nedelec, R. Purvis, T. B. Ryerson, G. W. Sachse, H. Schlager, Ozone production from the 2004 North American boreal fires. *J. Geophys. Res. Atmos.* **111**, D24S07 (2006).

85. E. Real, K. S. Law, B. Weinzierl, M. Fiebig, A. Petzold, O. Wild, J. Methven, S. Arnold, A. Stohl, H. Huntrieser, A. Roiger, H. Schlager, D. Stewart, M. Avery, G. Sachse, E. Browell, R. Ferrare, D. Blake, Processes influencing ozone levels in Alaskan forest fire plumes during long-range transport over the North Atlantic. *J. Geophys. Res. Atmos.* **112**, (2007).

86. H. Tanimoto, K. Matsumoto, M. Uematsu, Ozone-CO correlations in Siberian wildfire plumes observed at Rishiri Island. *SOLA* **4**, 65–68 (2008).

87. J. D. Paris, A. Stohl, P. Nédélec, M. Y. Arshinov, M. V. Panchenko, V. P. Shmargunov, K. S. Law, B. D. Belan, P. Ciais, Wildfire smoke in the Siberian Arctic in summer: Source characterization and plume evolution from airborne measurements. *Atmos. Chem. Phys.* **9**, 9315–9327 (2009).

88. H. B. Singh, B. E. Anderson, W. H. Brune, C. Cai, R. C. Cohen, J. H. Crawford, M. J. Cubison, E. P. Czech, L. Emmons, H. E. Fuelberg, Pollution influences on atmospheric composition and chemistry at high northern latitudes: Boreal and California forest fire emissions. *Atmos. Environ.* **44**, 4553–4564 (2010).

89. P. Baylon, D. A. Jaffe, N. L. Wigder, H. Gao, J. Hee, Ozone enhancement in western US wildfire plumes at the Mt. Bachelor Observatory: The role of NOx. *Atmos. Environ.* **109**, 297–304 (2015).

90. A. D. Teakles, R. So, B. Ainslie, R. Nissen, C. Schiller, R. Vingarzan, I. McKendry, A. M. Macdonald, D. A. Jaffe, A. K. Bertram, K. B. Strawbridge, W. R. Leaitch, S. Hanna, D. Toom, J. Baik, L. Huang, Impacts of the July 2012 Siberian fire plume on air quality in the Pacific Northwest. *Atmos. Chem. Phys.* **17**, 2593–2611 (2017).

91. C. Wiedinmyer, J. C. Neff, Estimates of CO2 from fires in the United States: Implications for carbon management. *Carbon Balance Manag.* **2**, 10 (2007).

92. M. Val Martin, R. A. Kahn, M. G. Tosca, A global analysis of wildfire smoke injection heights derived from space-based multi-angle imaging. *Remote Sens.* **10**, 1609 (2018).